



UNIVERSITÀ
DEGLI STUDI
FIRENZE

DOTTORATO DI RICERCA IN
ATOMIC AND MOLECULAR PHOTONICS

CICLO XXXVI

Coordinatore Prof. Diederik Wiersma

From superfluids to droplets:
quantum phenomena
with a tunable Bose-Bose mixture

Settore Scientifico Disciplinare
FIS/03

Dottorando

Dott. Luca Cavicchioli

Supervisore

Prof. Francesco Minardi

Coordinatore

Prof. Diederik Wiersma

Anni accademici: 2020-2023

Abstract

Superfluids are one of the most intriguing among macroscopic quantum phenomena, where the large-scale properties of the system reveal the small-scale quantum properties of its constituent components: this happens because of the coherent interaction of these components, which interfere constructively, and therefore amplify their characteristics. For the specific case of superfluids, this is most famously manifest in their dissipationless flow, whose observation led to their discovery, but also in a plethora of other peculiarities, which are, as said, ultimately due to coherence effects within the fluid particles. Apart from a low temperature laboratory, the presence of superfluids has been hypothesized in many systems, ranging from superconductors to neutron stars. A facet of superfluidity that has long been a fertile area of study is that of multicomponent superfluids, where two different specimens of such fluids interact, giving rise to novel and interesting phenomena, which would not be present in the single component case. While different from *stricto sensu* superfluidity, Bose-Einstein condensation is intimately linked to it, as it is, ultimately, its cause.

In this thesis, we focused on the physics of superfluids, investigated with a mixture of Bose-Einstein condensates realized with ultracold ^{41}K and ^{87}Rb . These atoms have the capability, which is of particular interest for our stated purpose, of tuning the interactions between the K and the Rb atoms, enabling the exploration of the whole phase diagram of the mixture. The work has been done in three phases.

In the first phase, we have developed a procedure to obtain the double condensate in the correct hyperfine state, and has resulted in the production of Bose-Einstein condensates with tunable interspecies interactions, having a total number of atoms ranging between 5×10^4 and 3×10^5 , in a consistent and reliable way.

In the second phase, we have investigated the physics of the dipole oscillation of the condensate mixture. Dipole oscillations are one of the possible collective excitations of a condensate, and those where the presence of interspecies interactions more dramatically changes the features of the modes, with respect to the single component case. We have experimentally measured their behaviour for various interspecies interaction strengths, and compared it with the theoretical models, finding which are more amenable to the description of the observations in various cases.

In the third phase, we have designed and built a new, high-resolution imaging system. This system is capable of resolution of approximately $1.5 \mu\text{m}$, in contrast to the $5 \mu\text{m}$ previously attainable, widening the capabilities of the apparatus. The system needed a compensation of the objective, which is on the path of the magneto-optical trap laser beam, and a new

sequence of imaging pulses, to adapt to the different orientation of the probe beam with respect to the magnetic fields, and to the different strength of the latter when the image is done on a trapped condensate, as opposed to one that is free-falling. We used this apparatus to obtain some preliminary in-situ images of a quantum droplet. Quantum droplets are very peculiar self-bound states of a mixture, where the collapse of the atomic cloud, in a regime of very strong interspecies attraction, is impeded by the quantum fluctuations, and instead an hydrodynamic equilibrium is reached. Such states have peculiar features not normally found in quantum gases.

With the work done in this thesis, we have built the foundations for further investigations of multicomponent superfluidity, with the eventual aim of contributing to the exploration of this wide and fascinating subject.

Contents

1. Introduction	1
2. Dual species Bose-Einstein condensates	5
2.1. Two body interactions in cold gases	6
2.1.1. Generalities of two-body scattering in cold gases	6
2.1.2. Feshbach resonances	8
2.1.3. Interspecies Feshbach resonances for ^{41}K - ^{87}Rb	11
2.2. Bose-Einstein condensation in interacting condensates	14
2.2.1. Ground state and thermodynamic properties	14
2.2.2. Elementary excitations and quantum depletion	16
2.2.3. Gross-Pitaevskii equation	17
2.3. A condensate of two species	19
2.3.1. Phases of the interacting condensates	19
2.3.2. Elementary excitations of a double BEC	22
2.4. Beyond-mean-field interactions and quantum droplets	23
3. Preparation of a double species Bose-Einstein Condensate	27
3.1. Experimental apparatus	27
3.1.1. Vacuum apparatus	28
3.1.2. Laser sources	29
3.1.3. Laser locking	32
3.1.4. Optical dipole trap	33
3.1.5. Magnetic fields	37
3.2. Cooling sequence	38
3.3. Hyperfine transfers	41
3.3.1. Feshbach field calibration	43
3.4. Gravity compensation	44
4. Dipole oscillations of an interacting bosonic mixture	49
4.1. Theoretical framework	49
4.1.1. Classification of the collective excitations	50
4.1.2. Coupled models of dipole oscillations	52
4.2. Experimental protocol	56

4.3.	Frequencies and amplitudes of the oscillations	60
4.4.	Role of population imbalance	64
4.5.	Oscillation damping	65
5.	High resolution imaging of a Bose-Bose mixture	69
5.1.	Absorption imaging of degenerate quantum gases	69
5.2.	Design	71
5.2.1.	Description of the objective	71
5.2.2.	MOT compensation	75
5.3.	Objective performance	77
5.3.1.	Magnification calibration	80
5.4.	High-field imaging	81
5.5.	In situ images of a Bose-Bose mixture	84
6.	Characterization of a Digital Micromirror Device	87
6.1.	DMD Setup	87
6.2.	Image calibration and optimization	90
6.2.1.	Geometric calibration	90
6.2.2.	PI optimization	92
6.3.	Characterization	92
6.3.1.	Timing properties	92
6.3.2.	Sharpness	93
6.3.3.	Residual light	94
6.3.4.	Filtering	94
	Conclusions and outlook	97
A.	Calculation of high-field imaging transitions	99
A.1.	Transition frequencies	99
A.2.	Transition amplitudes	104
B.	Denoising an Optical Density image	109
	Bibliography	115

List of Figures

2.1. Two channel model for Feshbach resonances	9
2.2. Interspecies scattering length for ^{41}K - ^{87}Rb	13
2.3. Phase diagram for the ^{41}K - ^{87}Rb mixture.	21
2.4. Mean-field collapse phase diagram for ^{41}K - ^{87}Rb	26
3.1. Double condensates of ^{41}K - ^{87}Rb	28
3.2. Experimental apparatus	29
3.3. Scheme of laser sources	30
3.4. Transition scheme	31
3.5. Laser locking scheme	32
3.6. Trapping laser scheme	35
3.7. Magnetic coils	37
3.8. Curved field as produced by Feshbach coils	38
3.9. Cooling sequence	39
3.10. Trap potential	40
3.11. Hyperfine sublevel energies	42
3.12. Transfer efficiency curve for Feshbach field calibration	44
3.13. Calibration of Feshbach field	45
3.14. Magnetic moment as a function of external field	46
3.15. Calibration of sag compensation current	46
4.1. Semiclassical model predictions	55
4.2. Dipole oscillation of ^{41}K - ^{87}Rb	57
4.3. Stability of oscillations	58
4.4. Dipole oscillation frequencies	61
4.5. Dipole oscillation amplitudes	62
4.6. Overlap of predicted and measured frequencies	63
4.7. Effect of population imbalance on dipole oscillation	64
4.8. Dipole oscillation decay	66
5.1. High resolution objective and imaging scheme	73
5.2. MOT compensation optimization	77
5.3. MOT compensation scheme	78

5.4. Image of USAF 1951 chart	78
5.5. Image of 1 μm pinhole	79
5.6. Magnification calibration	81
5.7. Frequencies of the imaging transitions	82
5.8. Strengths of the imaging transitions	83
5.9. High resolution image of attractive mixture	84
5.10. High resolution image of droplet	85
6.1. DMD setup	88
6.2. Optimal DMD orientation	89
6.3. DMD image calibration	91
6.4. Image sharpness	93
6.5. Residual light intensity	95
6.6. Effect of filtering	96
B.1. K image denoising	110
B.2. K image denoising, spatial frequencies	111

List of Tables

2.1. Parameters for the ^{41}K - ^{87}Rb interatomic potential	12
2.2. Interspecies Feshbach resonances for ^{41}K - ^{87}Rb	14
3.1. Hyperfine sublevel data	42
4.1. Oscillation decay times	67
5.1. Technical data for the high-resolution objective lenses	71
5.2. Optical data for the high-resolution objective	74
A.1. Hyperfine splittings of $^2\text{P}_{3/2}$ for ^{41}K and ^{87}Rb	100
A.2. Coefficients for the calculation of the Zeeman Hamiltonian	101

Introduction

Ever since its inception, the study of quantum physics has been inextricably intertwined with the ideas and the methods of statistical mechanics [1]. This link is nowhere more evident than in the concept of quantum statistics, in which the intrinsic indistinguishability of the particles in a quantum regime changes drastically their thermodynamic properties, dividing particles in two classes according to their behaviour: either exchange-symmetric bosons, following the Bose-Einstein statistic [2, 3] or exchange-antisymmetric fermions, that obey the Fermi-Dirac statistic [4, 5]. The phenomenon of Bose-Einstein condensation started to rouse the interest of physicists worldwide after the discovery of superfluid liquid helium [6], when London advanced an explanation that linked superfluidity with the formation of a condensate [7]; it was then further cast into spotlight when another macroscopic quantum phenomenon, superconductivity [8], was explained in terms of condensation of quasiparticles by Bardeen, Cooper, and Schrieffer [9].

The first impulse to the realization of a Bose-Einstein condensate in atomic gases was given by Stwalley and Nosanow [10]: its experimental realization was achieved two decades later—spurred by advances in laser cooling [11, 12] and atomic trapping [13]—first in ^{87}Rb [14], and then, after a few months, in ^7Li [15] and in ^{23}Na [16]. From these initial experiments, the study of degenerate quantum gases has greatly expanded to many topics, encompassing both fundamental and more applied physics.

Early proposals for the realization of a mixture of Bose-Einstein condensates [17, 18] were focused on the investigation of multicomponent superfluidity, which theretofore had been concentrated on superfluid helium [19–23]. This interest lies in the richer variety of phenomena that the presence of an additional species offers, as the interaction between the atoms is split into three relevant quantities: namely, one interspecies and two intraspecies, which drastically change their properties with respect to the single species case. It is with these goals in minds that the first experiments were realized, first with spin mixtures of ^{87}Rb [24] and ^{23}Na [25], and after with an heteronuclear mixture of ^{41}K - ^{87}Rb [26]. The understanding of multicomponent superfluids, apart from the mentioned ^3He - ^4He and ^6He - ^4He systems, could be crucial in other areas, such as for superconductors [27–30] or neutron stars [31–33].

Apart from multicomponent superfluidity, the variety of interesting phenomena with quantum mixtures is astounding, including, but not limited to, the study of collective dynamics [26, 34, 35], of the physics of polarons [36–39], of quantum turbulence [40], the formation of solitonic states [41, 42], three body physics, such as the formation of Efimov trimers [43–46], and measurements of the equivalence principle [47–49]. Moreover, mixtures have been instrumental in the formation and investigation of ultracold molecules, which, in and of itself, is a vast field of inquiry [50–57].

Another area in which mixtures, both of the spin and of the chemical varieties, have been in the spotlight is in study of quantum droplets. Quantum droplets are self-bound states, where the equilibrium is given by the interplay between an attractive and a repulsive interaction, which is ultimately due to quantum fluctuations [58]; as these interactions scale differently as a function of density, there is a finite size for which an atomic cloud is stable in free space. The first quantum droplets were obtained with dipolar quantum gases [59, 60]: when the dipole-dipole interaction is attractive, these gases are unstable against collapse, that is, until the beyond-mean-field effects mentioned before stop the collapse and achieve an hydrostatic equilibrium. They have then been observed in ^{39}K spin mixtures [61, 62], where the attractive interaction was, instead, solely caused by the contact interaction, and therefore completely isotropic. Due to the nature of the stabilizing force that intervenes in the droplet formation, these states show peculiar properties similar to those of liquids, such as incompressibility [63]; they can also show a crossover, dictated by the total number of atoms in the state, between a droplet proper and a bright soliton [64]—another kind of localized state—, when confined by a trapping potential. The main obstacle to the characterization of a droplet is the fact that, at the densities that it usually has, three-body recombination of the ultracold atoms leads to a finite lifetime of the state: for this reason, droplets have been created in heteronuclear mixtures [65, 66].

Given the central role of the interactions in the physics of mixtures, their tunability is one of the main features of an atomic platform [67]. While many mechanisms to achieve this exist, such as coherent coupling [68] or Raman coupling [69], the most widely used is that of magnetic Feshbach resonances [70], especially for our case of interest of heteronuclear mixtures.

A variety of mixtures have been experimentally realized, even if we limit ourselves to considering only mixtures of Bose Einstein Condensates with two chemically different species, as is the one which is the topic of this thesis. The first of such mixtures realized experimentally was ^{41}K - ^{87}Rb [26], with the aim of studying multicomponent superfluidity, and, in later incarnation, of realizing double species quantum simulations and molecules in optical lattices [71], for interferometry [72, 73], and the study of impurity physics [74]. This mixture has the capability of tuning the interspecies interactions, while keeping the intraspecies interactions constant, thanks to two conveniently located magnetic Feshbach resonances [71]. The next to reach degeneracy was the ^{133}Cs - ^{87}Rb mixture [75, 76], with the purpose of obtaining ultracold molecules with a permanent electric dipole moment, which were obtained a few years later [52]; in this mixtures, both ^{133}Cs - ^{87}Rb [77] and ^{133}Cs - ^{133}Cs [78] Feshbach resonances are present, giving the possibility of tuning both interactions in various regimes. The first mixtures involving an alkali-earth metal were ^{88}Sr - ^{87}Rb and ^{84}Sr - ^{87}Rb [79], for production of ultracold molecules of these two species: this is because the molecule formed by the combination of an alkali and

an alkali-earth metal has not only electrical, but also a magnetic dipole moment, due to its open shell. The tunability in this mixture is given by an interspecies Feshbach resonance [80]. Afterwards came the ^{39}K - ^{87}Rb mixture, for studying quantum phase transitions [81] and the formation of self-bound droplets [82]: these investigations are favoured by the present of a rich resonance structure in the mixture, where both ^{39}K - ^{39}K [83] and ^{39}K - ^{87}Rb [84] can be tuned via a Feshbach resonance. In 2018, condensation of ^{23}Na - ^{39}K was achieved [85], with the stated purpose of obtaining ultracold molecules which were chemically stable and bore an electric dipole moment, and also the comparison of Bosonic and Fermionic (^{23}Na - ^{40}K) molecules [57]. In the same year, another class of mixtures reached degeneration, namely the Er-Dy, in five isotopic varieties: ^{166}Er - ^{164}Dy , ^{168}Er - ^{162}Dy , ^{168}Er - ^{164}Dy , ^{170}Er - ^{162}Dy , and ^{170}Er - ^{164}Dy . Here we have a rich Feshbach spectrum for both intraspecies collisions and for the interspecies collisions [86]; moreover, the dipole-dipole interaction is present for all scattering pairs, giving rise to a complex phase diagram [87] where anisotropic, long range effects play a key role. A few years later came the condensation of ^{133}Cs - ^{170}Yb and ^{133}Cs - ^{174}Yb , where the availability of various Yb isotopes for the realization of the mixtures, united with the Feshbach spectrum of ^{133}Cs and its large mass, give a large tunability range for the interaction parameters, that enable the study of effects beyond the mean field approximation with this mixture [88]. Also in 2021 a BEC of ^{23}Na - ^{133}Cs was produced: for this experiment, the objectives include the creation of ultracold molecules (which have the largest electric dipole for chemically stable bialkali molecules), and their further employment to study dipolar crystals and fractional Mott insulators [89]; apart from the Feshbach resonances in ^{133}Cs , this mixture bears interspecies resonances as well [90]. The last mixture obtained to date was ^7Li - ^{133}Cs [91]: the strong atomic mass imbalance in this mixtures, united with the presence ^7Li - ^{133}Cs and ^{133}Cs - ^{133}Cs Feshbach resonances, makes it interesting for investigating Efimov phenomena and the physics of polarons and impurities; in this last case, both the heavy and the light impurity regimes could be investigated.

It is within this historical context that our experiment was conceived, with aims of exploring the varied physics of multicomponent superfluids. Due to the aforementioned tunability of the interspecies interaction strength with a magnetic Feshbach resonance, the physics that can be investigated with this platform encompasses the whole phase diagram, going from the immiscible regime, and the corresponding miscible-immiscible phase transition on the repulsive side, to the investigation of beyond-mean-field structures, such as droplets, on the other extreme. During the time span of my PhD, the focus was mainly on the attractive side, looking into both collective excitations, where the character of the interspecies interactions drastically changes the phenomenon characteristics, and on the realization of quantum droplets, and their probing with a new and improved imaging apparatus.

This thesis is structured in the following way:

- In Chapter 2, we will talk about the theoretical framework for the description of the ^{41}K - ^{87}Rb mixture, going over some fundamentals of the scattering theory for ultracold atoms, as well as the theory of Bose-Einstein condensates for both the single and double component cases. Finally, we will illustrate the basics of beyond-mean-field theory, in order to describe quantum droplets.

- In Chapter 3, we will look at the experimental techniques for the preparation of a double condensate of ^{41}K - ^{87}Rb with tunable interspecies interactions. We will start with an exposition of the apparatus used in this experiment; we will then pass over to the experimental sequence steps needed, in order, to reach degeneracy, to transfer the condensates each to its respective hyperfine ground state, and finally to compensate gravity, enabling the full overlap of the two clouds.
- In Chapter 4, we will focus on the dipole oscillations, which is a collective mode of a Bose-Einstein condensate that, for a single component, would be characterized by its insensitivity to the interactions, whereas this is not true anymore for a mixture. After having seen the theory of the dipole mode, we will go on to the experimental protocol for its excitation, ensuring that the excursion amplitude is low enough to remain in the linear regime, and the analysis of the data thus obtained; we will then describe the main results of our experimental measures, namely the frequencies and amplitudes, and the role of the population imbalance on the frequency of an highly attractive state. We will conclude with a brief look at the damping of the oscillations and its consequences. The work presented here is part of what is found in [92].
- In Chapter 5, we will chronicle the implementation of an high-resolution imaging system for the apparatus. We will start from the design of the objective, and its theoretical performance, and then pass on to the compensation of the MOT beam, which is needed because of the physical position, in the apparatus, of the objective tube. Then, the objective is tested, on a test setup, in order to assess its real optical characteristics; it is then mounted and calibrated on the experimental apparatus. We will go over the details of high-field imaging for the mixture, which is needed to view the atoms in-situ (the calculations of the transition frequencies are reported in Appendix A). Finally, we will look at some high-resolution, in-situ images of the Bose-Bose mixture, in its most demanding regime, namely that of mean-field-collapse.
- In Chapter 6, we will detail a part of the development work done during my stay in the Quantum Gases Experiment group of Prof. Leticia Tarruell, with the eventual aim of the realization of arbitrary optical potentials within the K experiment therein. First, the setup for the performed tests is explained; then, we will look at calibration and defect compensation routines, and, finally, at some characterization results.

Dual species Bose-Einstein condensates

Bose-Einstein condensation (BEC) is a physical phenomenon, defined as the macroscopic occupation of the ground state for a many-body system: this is made possible, and indeed necessary, by the quantum statistics of bosons [93].

Let's take, for example, a system of non interacting, identical bosons in a closed box of volume \mathcal{V} . The occupations numbers, taking for the moment the energy states to form a discrete spectrum, are

$$N_i = \frac{1}{\exp\left[\frac{1}{k_B T}(E_i - \mu)\right] - 1}. \quad (2.1)$$

In order to exclude nonphysical negative occupation numbers, we notice that the inequality $\mu < E_0$ must hold.* If now we cool the box, the chemical potential will have to increase, in order to keep the denominator constant. From our assumption that the box is closed, we can impose the conservation of the total number of atoms; if we go to the continuum limit for the states $i > 0$, we have [94]

$$N = N_0 + \frac{\mathcal{V}}{(2\pi\hbar)^3} \int \mathcal{D}(E) N(E) dE \quad (2.2)$$

$$= N_0 + \frac{\mathcal{V}}{\lambda_T^3} g_{3/2}(e^{\beta\mu}), \quad (2.3)$$

where

$$\lambda_T = \sqrt{\frac{2\pi\hbar^2}{mk_B T}} \quad (2.4)$$

is the thermal wavelength, and

$$g_p(z) = \sum_{l=0}^{+\infty} \frac{z^l}{l^p} \quad (2.5)$$

*We suppose here $E_i < E_{i+1}$.

is the polylogarithm function [95].

From this, we can see that $N_0 = 0$ for temperatures above a critical temperature

$$T_c = \frac{mk_B}{2\pi\hbar^2} \left(\frac{\mathcal{V}}{g_{3/2}(1)} \right)^{3/2}, \quad (2.6)$$

while, below,

$$N_0 = \left[1 - \left(\frac{T}{T_c} \right)^{3/2} \right] \quad (2.7)$$

meaning that we have a second order phase transition to a BEC.

In this chapter, we will lay the theoretical foundations upon which we will build all the later parts of the thesis; given that our experimental system is a mixture of two condensates, and that one of its main features is the capability of tuning the interspecies interactions, we will have to add two ingredients to the perfect Bose gas: the first are interactions among the atoms of which said gas is made of, and the second is the presence of a second species in the condensate.

We will start, in Section 2.1, by looking at how interactions between cold atoms work, and in Section 2.2 we will see what role they play in the theory of Bose-Einstein condensates. We will then move on to explain, in Section 2.3, how the introduction of another component shuffles the cards around yet again, with respect to the case of a single species BEC. Finally, in Section 2.4, we will talk about another type of not previously treated interactions and of the phenomena that this interactions give rise to.

2.1. Two body interactions in cold gases

While the phenomenon of condensation, in principle, would encompass any physical system that obeys Bose-Einstein statistics, we will focus the treatment in this section on the pertinent case of dilute and cold atomic gases. For this kind of system, the diluteness condition is valid:

$$r_0 \ll d \quad (2.8)$$

where r_0 is some kind of typical radius for the interaction, and d is the mean interparticle distance.

Respecting such a condition is experimentally necessary, as none of the atoms commonly used for the production of BECs is gaseous at temperatures below the critical temperature for condensation. However, for desublimation (or liquefaction, in the case of He) to occur, three-body collisions are necessary, and, due to gas diluteness, their rate is oftentimes—but not always—sufficiently small, given the typical duration of an experiment.

2.1.1. Generalities of two-body scattering in cold gases

From quantum scattering theory [96], we know that, for two interacting particles, the solutions of the Schrödinger equation, recast as a problem of a single particle of reduced mass μ moving in a central potential $V(\mathbf{r})$, can be factorized into a radial and an angular part:

$$\Psi(r, \theta, \phi) = R(r) Y_{lm}(\theta, \phi), \quad (2.9)$$

where Y_{lm} are the spherical harmonics, and $R(r)$ is a radial wave function, such that $\chi(r) = rR(r)$ satisfies the radial Schrödinger equation:

$$\left[-\frac{\hbar^2}{2\mu} \frac{d^2}{dr^2} + V(r) + \frac{\hbar^2 l(l+1)}{2\mu r^2} \right] \chi(r) = E\chi(r), \quad (2.10)$$

where

$$\mu = \frac{m_1 m_2}{m_1 + m_2} \quad (2.11)$$

is the reduced mass.

It can be shown that, asymptotically [97],

$$\lim_{rk \gg l} \chi(r) \propto \sin\left(kr - l\frac{\pi}{2} + \delta_l\right) \quad (2.12)$$

$$\propto \sin\left(kr - l\frac{\pi}{2}\right) + \tan(\delta_l) \cos\left(kr - l\frac{\pi}{2}\right) \quad (2.13)$$

where δ_l is called the scattering phase shift: this parameter characterizes completely the two body scattering in the asymptotic regime. In the long wavelength regime $k \rightarrow 0$, we have that [98]

$$\tan(\delta_l) \propto k^{2l+1}, \quad (2.14)$$

which means that, for a fixed initial energy E , and thus fixed $k = \sqrt{2\mu E}/\hbar$, the effect of the potential, measured by δ_l , decreases as l increases.[†] The starting wave function Ψ describes a stationary scattering state, for which the asymptotic form will, in general, have a circular, scattered wave superimposed with the incoming plane wave

$$\lim_{rk \gg 1} \Psi(\mathbf{r}, \mathbf{k}) = e^{ik_z z} + f(k, \theta) \frac{e^{ikr}}{r}; \quad (2.16)$$

we can express the scattering amplitude $f(k, \theta)$ as a partial wave expansion

$$f(k, \theta) = \sum_l (2l+1) P_l(\cos(\theta)) \frac{e^{2i\delta_l} - 1}{2ik} \quad (2.17)$$

$$= \sum_l (2l+1) P_l(\cos(\theta)) \left(\frac{k}{\tan(\delta_l)} - ik \right)^{-1}, \quad (2.18)$$

and, from that, the scattering cross section

$$\sigma_t = \int |f(k, \theta)|^2 d\Omega \quad (2.19)$$

$$= \sum_l \frac{4\pi}{k^2} (2l+1) \sin^2(\delta_l(k)). \quad (2.20)$$

[†]We suppose for V the boundary condition

$$\lim_{r \rightarrow +\infty} V(r) = 0. \quad (2.15)$$

If the two particles are indistinguishable, the scattering cross section changes, due to the Pauli exclusion principle: exchanging two particles means, in the reduced problem, making the transformation $\mathbf{r} \rightarrow -\mathbf{r}$. The symmetry of the wave function is instead dictated by the spherical harmonics:

$$\Psi_l(-\mathbf{r}) = (-1)^l \Psi_l(\mathbf{r}), \quad (2.21)$$

so, for the Pauli exclusion principles, only partial waves with even l are allowed for bosons, and only partial waves with odd l are allowed for fermions. Moreover, due to the interference between the indistinguishable particles, the differential cross section [99]

$$d\sigma = \frac{1}{2} |f(k, \theta) \pm f(k, \pi - \theta)|^2 d\Omega, \quad (2.22)$$

where the $+$ sign is for bosons and $-$ for fermions, is markedly different from that of distinguishable particles [100]

$$d\sigma = C \csc^4\left(\frac{\theta}{2}\right) d\Omega. \quad (2.23)$$

From our previous considerations, we can see that the most important partial wave for bosons is the s wave; according to (2.14) [97]:

$$\lim_{k \rightarrow 0} \frac{\tan(\delta_0)}{k} = -a \quad (2.24)$$

where a has the dimensions of a length, and is for this reason called scattering length. For fermions, or for non identical bosons at the second order of partial wave expansion, the same line of reasoning brings to a scattering volume v :

$$\lim_{k \rightarrow 0} \frac{\tan(\delta_1)}{k^3} = -v. \quad (2.25)$$

2.1.2. Feshbach resonances

Feshbach resonances, also known as Fano-Feshbach resonances, are one kind of scattering resonances occurring in the collisional physics of cold atoms [70]; they were introduced in the context of nuclear physics by Feshbach [101, 102], and in the context of atomic physics by Fano [103], because of the experimental observation that there were significant interactions between continuum states and bound states: in Feshbach's case, these interactions were represented by a nucleon scattering resonantly with a nucleus in an atomic reaction, whereas in Fano's case they were represented by the phenomenon of autoionization, where an atom or a molecule in a highly excited state spontaneously emits an electron [104].

Other relevant resonances for cold atoms are zero-energy resonances, shape resonances, and confinement induced resonances. Zero-energy resonances happen only for s -wave scattering, and are akin to the classical example of the scattering resonance from a square well [96]: the scattering length diverges when there is a bound state just below the dissociation threshold, which is also the energy of the scattering event (i.e. $E = 0$); this happens, for example, in ^{133}Cs [105]. Shape resonances, on the other hand, happen only for $l > 1$ partial waves: here, a bound state behind the centrifugal barrier resonantly enhances a scattering process when the

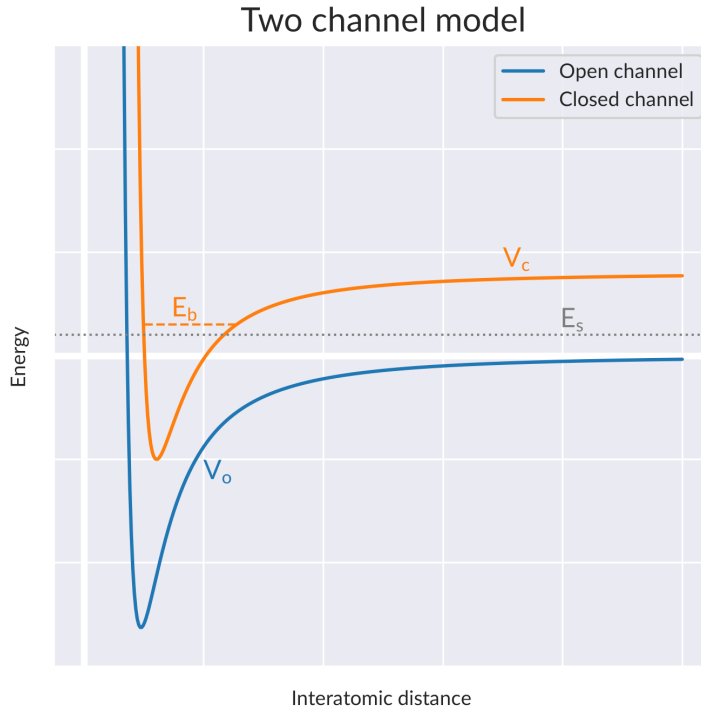


Figure 2.1.: Depiction of the two channel model used to explain Feshbach resonances. The blue continuous line represents the potential for the open channel V_o , the orange one the potential for the closed channel V_c , the dotted grey line the scattering energy E_s , and the dashed orange line the energy of a bound state in the closed channel.

collision energy is similar to that of the bound state; such a resonance has been found, for example, in ^{87}Rb [106] and ^4K [107] for d-wave scattering. Confinement induced resonances, along with Feshbach resonances, differ from the previous ones in that they involve two different states: an energetically permitted unbound state, called the open channel, and an energetically forbidden bound state, called the closed state: for confinement induced resonances, the resonance happens when the transversal harmonic oscillator length a_\perp (see (2.79)) is equal to Ca , where a is the scattering length, and C is a numerical constant, due to the fact that external confinement changes the density of states, which has a singularity for the aforementioned ratio a_\perp/a [108–110]; this kind of scattering resonance has also been predicted [111, 112] and seen [113] in two-species cases when one of the two species is confined in a different dimensionality regime than the other.

Ever since having been observed in a sodium BEC [114], Feshbach resonances have been a workhorse of cold atom physics, mainly due to the fact that the resonant character—that is, the scattering length—can be tuned with an external field, either magnetic [115], which is the kind observed in the sodium BEC, or optical [116, 117], although the latter are usually employed when a magnetically tunable Feshbach resonance is absent [70].

A simple treatment of a Feshbach resonance, which is exposed in this paragraph, can be found in the original work by Fano [103]. There, he starts from a two-channel model: for a scattering energy E_s , we have an open channel, that is, a configuration for which the interatomic potential $V_o(\mathbf{r})$ is such that $V_o(r \rightarrow +\infty) \rightarrow E_o \leq E_s$, and a closed channel $V_c(\mathbf{r})$, where $V_c(r \rightarrow +\infty) \rightarrow E_c > E_s$; in other words, the open channel is determined by the interatomic potential of the reactants, whereas the closed channel by that of the products, which, in our case, are the two colliding atoms and the molecule that they would form. We suppose also that V_c has a bound state (i.e. there is a molecular energy level) with an energy E_b close to E_s . An illustration of this model is shown in Figure 2.1. In this situation, we have for this problem the Hamiltonian

$$\langle \psi(E) | H | \psi(E_s) \rangle = E_s \delta(E_s - E) \quad (2.26a)$$

$$\langle \psi(E_s) | H | \phi \rangle = V(E_s) \quad (2.26b)$$

$$\langle \phi | H | \phi \rangle = E_b, \quad (2.26c)$$

where $|\Psi\rangle$ is a scattering state in the open channel, and $|\phi\rangle$ is a bound state in the closed channel. We want to find the eigenstates $|\Xi\rangle$ of this Hamiltonian, which will be of the form

$$|\Xi(E)\rangle = \alpha(E) |\phi\rangle + \int \beta(E') |\psi(E')\rangle dE'. \quad (2.27)$$

Using (2.27) as a solution of the system (2.26), we reduce it to

$$\alpha E_b + \int \beta(E') V(E') dE' = E \alpha \quad (2.28a)$$

$$V(E_s) \alpha + E_s \beta(E_s) = E \beta(E_s); \quad (2.28b)$$

by solving this system, we can express β as the formal solution

$$\beta(E_s) = \left[\frac{1}{E - E_s} + z(E) \delta(E - E_s) \right] V(E_s) \alpha, \quad (2.29)$$

where z is a function to be determined by substituting back into (2.28a), obtaining

$$z(E) = \frac{E - E_b - F(E)}{|V_E|^2}, \quad (2.30)$$

where

$$F(E) = \mathcal{P} \int_{-\infty}^{+\infty} \frac{|V(E')|^2}{E - E'} dE', \quad (2.31)$$

in which \mathcal{P} denotes the Cauchy principal value of the integral.[‡]

[‡]Let $a < b \in \mathbb{R}$, $f: \mathbb{R} \rightarrow \mathbb{R}$ continuous $\forall x \in [a, b]$, and $x_0 \in]a, b[$. Then

$$\mathcal{P} \int_{-\infty}^{+\infty} \frac{f(x)}{x - x_0} dx = \lim_{\epsilon \rightarrow 0} \int_a^{x_0 - \epsilon} \frac{f(x)}{x - x_0} dx + \int_{x_0 + \epsilon}^b \frac{f(x)}{x - x_0} dx \quad (2.32)$$

is the principal part of the integral [118].

Assuming for the unbound state an asymptotic form analogous to (2.12)

$$\lim_{kr \gg 1} \int \beta(E') \psi(E') dE' \propto \sin(kr + \delta_0 + \delta(E)), \quad (2.33)$$

we conclude that the energy dependent part of the scattering shift is[§]

$$\tan(\delta(E)) = -\frac{\pi |V(E)|^2}{E - E_b - F(E)}; \quad (2.34)$$

The scattering length is, therefore,

$$\begin{aligned} a &= -\lim_{k \rightarrow 0} \frac{\tan(\delta)}{k} \\ &= \frac{\pi |V(0)|^2}{E_b - F(0)}, \end{aligned} \quad (2.35)$$

and we can see that a diverges when $E_b = F(0)$. In the atom-molecule picture, the interpretation of this fact is that a Feshbach resonance happens when the molecular bound state crosses the interatomic dissociation threshold [119].

In our main case of interest, namely a magnetically tunable Feshbach resonance, we have that the two channels have different magnetic momenta; thus [70]

$$E_b - E = \delta\mu(B - B_b), \quad (2.36)$$

where $\delta\mu$ is the difference between the magnetic moment of the scattering participants μ_a , and the magnetic moment of the bound state μ_b : given that B externally controllable, this makes possible the tuning of the scattering length. An experimentally useful form of the scattering length for a magnetically tuned Feshbach resonance is

$$a(B) = a_{\text{bg}} \left(1 - \frac{\Delta}{B - B_r} \right), \quad (2.37)$$

where Δ and B_r are phenomenological parameters related to the physical parameters of the scattering [120].

There are various schemes for the classification of Feshbach resonances in ultracold atoms; in most of those, the orbital quantum number l' of the molecule is the principal quantum number of interest, as it is the most characterizing for the resonance properties [70]: we will thus say s, p, d-wave resonances, and so on, according to this particular quantum number. Note that this does not correspond to the order of the partial wave expansion needed for the calculation of the resonance: for even l' , all even partial waves in general can contribute, and for odd l' all odd partial waves.

2.1.3. Interspecies Feshbach resonances for ^{41}K - ^{87}Rb

Interspecies Feshbach resonances are an interesting part of the physics of the ^xK - ^{87}Rb mixtures, and have been studied both theoretically and experimentally for all the isotopes of K [71, 121, 123–125].

[§]Following [103], we remark that, due to the normalization of the $|\psi\rangle$ in (2.26), $V(E)^2$ has the dimensions of an energy.

Table 2.1.: Model parameters for the interatomic potential from [71]: a_s and a_t are, respectively, the triplet and singlet scattering lengths and the C_i coefficients are those appearing in (2.42) (the C_{10} coefficient is reported in [121] to be taken from [122]). The units of measurement are in terms of Bohr's radius a_0 and Hartree energy E_H . In the work from which this table is taken, the magnitude of the exchange energy A_{ex} is a fit parameter.

Parameter	Value
a_s	$-109.6 \pm 2.0 a_0$
a_t	$-213.6 \pm 4.0 a_0$
C_6	$4288 \pm 2 a_0^6 E_H$
C_8	$(4.765 \pm 0.005) \times 10^5 a_0^8 E_H$
A_{ex}	$(2.01 \pm 0.04) \times 10^{-3} E_H$

In order to study a particular Feshbach resonance, there is a need for a particular Hamiltonian to put into (2.26). In our case, the scattering event is between two spin-1/2 atoms, and, as such, will have the further complication that the analysis has to be done taking into account both the singlet $^1\Sigma_g^+$ state and the triplet $^3\Sigma_u^-$ state for each channel. The coupled channel Hamiltonian, for the radial equation, is [126]:

$$H_{\alpha\beta} = \frac{\hbar^2}{2\mu} \frac{\partial^2}{\partial r^2} + E_s \delta_{\alpha\beta} - V_{\alpha\beta}. \quad (2.38)$$

The interchannel potential is:

$$V_{\alpha\beta}(r) = \left(E_{F_1, m_{F_1}} + E_{F_2, m_{F_2}} + \frac{\hbar^2 l(l+1)}{2\mu r^2} \right) \delta_{\alpha\beta} + V_{\alpha\beta}^{\text{int}}, \quad (2.39)$$

where $E_{F_i, m_{F_i}}$ are the hyperfine energies of the involved states, and V^{int} is an interaction potential given by the sum of two terms:

$$V_{\alpha\beta}^{\text{int}}(r) = V_{\alpha\beta}^{\text{el}}(r) + V_{\alpha\beta}^{\text{SS}}(r), \quad (2.40)$$

which are, respectively, the electronic and the spin-spin interaction potentials. An Hamiltonian with this potential cannot be simultaneously diagonalized for all r [126].

The electronic interaction potentials used in [84, 121] for the theoretical study of the Feshbach resonances are parametrized phenomenologically by three different terms:

$$V_{\alpha\beta}^{\text{el}}(r) = V_{\alpha\beta}^{\text{d}}(r) \pm \frac{V_{\alpha\beta}^{\text{e}}(r)}{2} + V_{\alpha\beta}^{\text{c}}(r). \quad (2.41)$$

The first term is called the dispersion term, and has a simple form

$$V^{\text{d}}(r) = -\frac{C_6}{r^6} - \frac{C_8}{r^8} - \frac{C_{10}}{r^{10}}, \quad (2.42)$$

and is given by the first terms of a multipole expansion of the van der Waals interaction between the two atomic clouds. The second term accounts for the exchange energy between

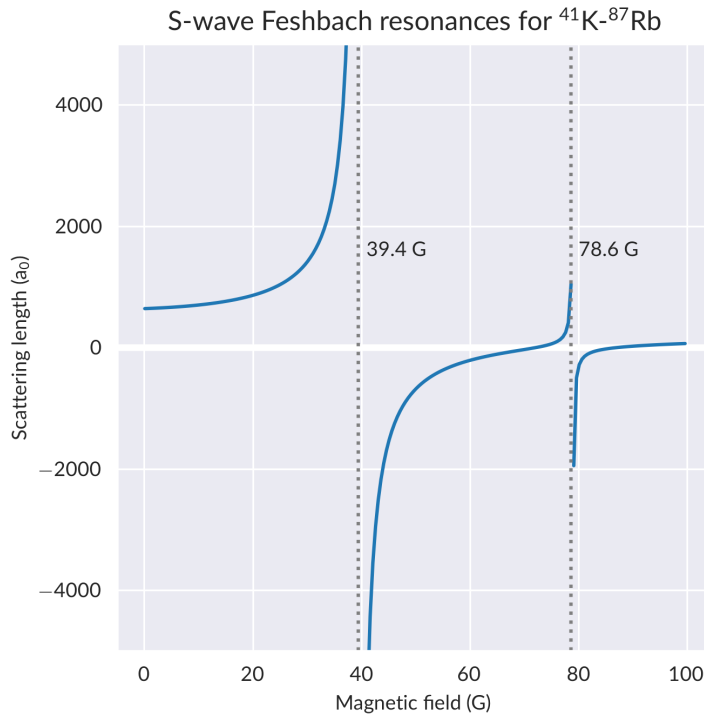


Figure 2.2.: Interspecies scattering length as a function of the strength of an external magnetic field. The two vertical dashed lines mark the positions of the (2,2,0) and (3,2,0) resonances (see Table 2.2), which are the ones used in the experiment for the tuning of the interspecies interactions.

channels in the asymptotic regime [127], where the sign of the interaction depends on the symmetry of the state (+ for the triplet, – for the singlet), and the third is a correction term to account for finite range effects in the close regime [128]; this last term is parametrized, and parameters are changed in order to find the best match with the scattering length of the triplet and singlet states. The latest values for the parameters of this model, as reported in [129], are based on simultaneous tuning of the data for all three isotopes of K, obtained from [84, 124, 129], and are reported in Table 2.1.

For our mixture, the tunability of the interspecies interactions is given by two interspecies Feshbach resonances for both species in the $|F = 1, m_F = 1\rangle$ hyperfine state [71]. The first is for $B_0 = 39.4 \text{ G} \pm 0.2 \text{ G}$, with a width $\Delta = 5.1 \text{ G} \pm 1.8 \text{ G}$, the molecular quantum numbers (f, m_f, l') of the bound state are (2,2,0). The second resonance has molecular quantum numbers (3,2,0), centre field $B_0 = 78.92 \text{ G} \pm 0.09 \text{ G}$, and width $\Delta = 0.35 \text{ G} \pm 0.14 \text{ G}$. In order to tune the interspecies interactions, we use a uniform magnetic field along the vertical axis, with field strengths varying in the range 66 G–77 G: this grants us the ability to explore all the regions of the phase diagram for the double BEC. This magnetic field region is mostly devoid of other resonances, apart from a d-wave resonance at 72.74 G, which is quite close to the zero crossing of the interspecies scattering length; for this reason, we usually prepare

Table 2.2.: Data for the experimentally confirmed interspecies Feshbach resonances in the ^{41}K - ^{87}Rb mixture, with the theoretically calculated resonance field B_{th} , the field from the experimental data B_e , the molecular quantum numbers, and the source of the data. The theoretically calculated field of the (2,2,0) resonance is not available in [71]. Field uncertainties are not reported in [130], except for the B_e of the (3,2,1) resonance for which a range is given: that value is reported here as the middle point of the range, with an uncertainty equal to half the range width.

B_{th} G	B_e G	(f, m_f, l')	Source
—	39.4 ± 0.2	(2, 2, 0)	[71]
44.63 ± 0.02	44.58 ± 0.05	(2, 1, 2)	[129]
47.90 ± 0.06	47.96 ± 0.10	(2, 0, 2)	[129]
52	51.71 ± 0.45	(3, 2, 1)	[130]
65	64.73	(1, 1, 2)	[130]
73	72.74	(1, 0, 2)	[130]
78.67 ± 0.04	78.57 ± 0.05	(3, 2, 0)	[129]

the condensates with a slightly attractive interaction. A summary of the known interspecies Feshbach resonances known for our mixture is presented in Table 2.2, and a graph of the scattering length in the region of the two resonances is in Figure 2.2.

2.2. Bose-Einstein condensation in interacting condensates

In this section, we will focus on the consequence of interactions in a degenerate Bose gas, that is quite different with respect to the case of a perfect gas. Following the treatment of [94], we will obtain the thermodynamic ground properties, and the elementary excitation spectrum of a weakly interacting uniform BEC. Finally, we will describe the treatment of a trapped condensate, by the means of the Gross-Pitaevskii equation.

2.2.1. Ground state and thermodynamic properties

We start by writing the field theoretic Hamiltonian for a Bose gas in a box of volume \mathcal{V} :

$$\hat{H}(\mathbf{p}) = \sum_{\mathbf{p}} \frac{p^2}{2m} \hat{a}_{\mathbf{p}}^\dagger \hat{a}_{\mathbf{p}} + \frac{1}{2\mathcal{V}} \sum_{\mathbf{q}, \mathbf{p}_1, \mathbf{p}_2} V_{\mathbf{q}} \hat{a}_{\mathbf{p}_1 - \mathbf{q}}^\dagger \hat{a}_{\mathbf{p}_2 + \mathbf{q}}^\dagger \hat{a}_{\mathbf{p}_1} \hat{a}_{\mathbf{p}_2}, \quad (2.43)$$

where $\hat{a}_{\mathbf{p}}$ and $\hat{a}_{\mathbf{p}}^\dagger$ are the annihilation and creation operator for a state with momentum \mathbf{p} , and $V_{\mathbf{q}}$ is the momentum-space representation of the two-particle interaction potential

$$V_{\mathbf{q}} = \int V(\mathbf{r}) e^{i\mathbf{q} \cdot \mathbf{r} / \hbar} d\mathbf{r}; \quad (2.44)$$

as mentioned above, the diluteness condition (2.8) implies that we can neglect, at this stage, three-body interactions between the particles.

The small moment limit which we considered in Section 2.1 means that we can consider only the $q = 0$ contribution in (2.44), and construct thus an effective potential

$$V_0 = \int V_{q=0} d\mathbf{r} = \frac{4\pi\hbar^2 a}{m} = g, \quad (2.45)$$

where a is the scattering length for the collision participants, to be substituted into (2.43). In this way, we have substituted a complicated interatomic potential with an approximation that will guarantee the right behaviour in the asymptotic limit: this kind of approximation is called a pseudopotential [131].

It is then possible to employ a method, due to Bogoliubov [132], that consists in describing the field $\hat{\Psi}$ on which (2.43) acts on as

$$\hat{\Psi}(\mathbf{r}, t) = \psi(\mathbf{r}, t) + \delta\hat{\psi}(\mathbf{r}, t), \quad (2.46)$$

where ψ is a classical field, equal to the expectation value of Ψ :

$$\psi(\mathbf{r}, t) = \langle \hat{\Psi}(\mathbf{r}, t) \rangle \quad (2.47)$$

$$= \sqrt{\frac{N_0}{\mathcal{V}}}, \quad (2.48)$$

where the last equation is valid for our uniform potential. In a low-temperature condensate, we can neglect the number of particles in the excited states, making the so called mean-field approximation

$$\delta\hat{\psi} \approx 0, \quad (2.49)$$

from which we can obtain all the necessary thermodynamic properties. The ground state energy is then given by

$$E_g = \frac{N^2 g}{2\mathcal{V}} = \frac{1}{2} g n N, \quad (2.50)$$

where n is the density $n = |\psi|^2 = N/\mathcal{V}$, and we identified $N_0 \approx N$ by using the mean field approximation. From this energy, using the appropriate classical expression [93], the equation of state

$$P = - \left(\frac{\partial E_g}{\partial \mathcal{V}} \right)_{S,N} = \frac{1}{2} g n^2, \quad (2.51)$$

the speed of sound

$$c = \sqrt{\frac{1}{m} \left(\frac{\partial P}{\partial n} \right)_S} = \sqrt{\frac{gn}{m}}, \quad (2.52)$$

and the chemical potential

$$\mu = \left(\frac{\partial E_g}{\partial N} \right)_{S,V} = gn = mc^2 \quad (2.53)$$

are obtained.

2.2.2. Elementary excitations and quantum depletion

The next thing is to obtain a dispersion relation for the elementary excitations, in order to have a known way of studying the perturbations and the dynamics of the condensate. For this, we go beyond the mean field approximation, starting from the field-theoretic Hamiltonian (2.43), and keeping all terms up to quadratic order for $\mathbf{p} \neq 0$, and quartic for $\mathbf{p} = 0$:

$$H = \frac{g}{2\mathcal{V}} \hat{a}_0^\dagger \hat{a}_0^\dagger \hat{a}_0 \hat{a}_0 + \sum_{\mathbf{p}} \frac{p^2}{2m} \hat{a}_{\mathbf{p}}^\dagger \hat{a}_{\mathbf{p}} + \frac{g}{2\mathcal{V}} \sum_{\mathbf{p} \neq 0} \left(4\hat{a}_0^\dagger \hat{a}_{\mathbf{p}}^\dagger \hat{a}_0 \hat{a}_{\mathbf{p}} + \hat{a}_{\mathbf{p}}^\dagger \hat{a}_{-\mathbf{p}}^\dagger \hat{a}_0 \hat{a}_0 + \hat{a}_0^\dagger \hat{a}_0^\dagger \hat{a}_{\mathbf{p}} \hat{a}_{-\mathbf{p}} \right) \quad (2.54)$$

$$= \frac{gN^2}{2\mathcal{V}} + \sum_{\mathbf{p}} \frac{p^2}{2m} \hat{a}_{\mathbf{p}}^\dagger \hat{a}_{\mathbf{p}} + \frac{gn}{2} \sum_{\mathbf{p} \neq 0} \left(2\hat{a}_{\mathbf{p}}^\dagger \hat{a}_{\mathbf{p}} + \hat{a}_{\mathbf{p}}^\dagger \hat{a}_{-\mathbf{p}}^\dagger + \hat{a}_{-\mathbf{p}} \hat{a}_{\mathbf{p}} \right), \quad (2.55)$$

where, in the last passage, we have used the Bogoliubov approximation

$$\hat{a}_0^\dagger \approx \hat{a}_0^\dagger \approx \sqrt{N}, \quad (2.56)$$

and the expansion

$$\hat{a}_0^\dagger \hat{a}_0^\dagger \hat{a}_0 \hat{a}_0 = \hat{a}_0^\dagger \left(\hat{a}_0 \hat{a}_0^\dagger - 1 \right) \hat{a}_0 \quad (2.57)$$

$$= \left(N - \sum_{\mathbf{p}} \hat{a}_{\mathbf{p}}^\dagger \hat{a}_{\mathbf{p}} \right)^2 - \left(N - \sum_{\mathbf{p}} \hat{a}_{\mathbf{p}}^\dagger \hat{a}_{\mathbf{p}} \right) \quad (2.58)$$

$$\approx N^2 - 2N \sum_{\mathbf{p}} \hat{a}_{\mathbf{p}}^\dagger \hat{a}_{\mathbf{p}}; \quad (2.59)$$

this Hamiltonian is known as the Bogoliubov Hamiltonian, and it can be diagonalized using the Bogoliubov transformations

$$\hat{a}_{\mathbf{p}} = u_{\mathbf{p}} \hat{b}_{\mathbf{p}} + v_{-\mathbf{p}}^* \hat{b}_{\mathbf{p}}^\dagger \quad (2.60a)$$

$$\hat{a}_{\mathbf{p}}^\dagger = u_{\mathbf{p}}^* \hat{b}_{\mathbf{p}}^\dagger + v_{-\mathbf{p}} \hat{b}_{\mathbf{p}}, \quad (2.60b)$$

where $\hat{b}_{\mathbf{p}}^\dagger$ and $\hat{b}_{\mathbf{p}}$ are the creation and annihilation operators of the Bogoliubov quasiparticles, which are bosonic quasiparticles that constitute the elementary excitations of the condensate.

It can then be shown that, for these particles, the dispersion relation is [132]:

$$\epsilon(p) = \sqrt{c^2 p^2 + \left(\frac{p^2}{2m} \right)^2} = \sqrt{\frac{p^2}{2m} \left(2mc^2 + \frac{p^2}{2m} \right)}. \quad (2.61)$$

This is known as Bogoliubov dispersion relation: in the low momentum limit, it is a linear phononic dispersion $\epsilon(p) = cp$, while in the high momentum limit it tends to a free particle behaviour $\epsilon(p) = p^2/(2m)$.

It is worth noting that, for $g < 0$, the sound speed becomes imaginary, which in turn means that $\epsilon(p)$ is imaginary if

$$p^2 < p_c^2 = 4m|g|n; \quad (2.62)$$

this leads to the creation of exponentially increasing sound waves that ultimately destabilize the condensate. However, such low momentum perturbations cannot be excited if the size of the condensate is smaller than their wavelength

$$\lambda_c = \frac{h}{p_c} = \frac{h}{\sqrt{4m|g|n}}, \quad (2.63)$$

and, therefore, condensates with dimensions comparable to λ_c are stable even with attractive interactions.

A feature that arises from the introduction of interactions in a Bose gas is that, even at zero temperature, there are still particles with $p \neq 0$. We can calculate the expectation value for a particle in a state $p \neq 0$ by using (2.60):

$$\langle a_{\mathbf{p}}^\dagger a_{\mathbf{p}} \rangle = |v_{-\mathbf{p}}|^2 + |u_{\mathbf{p}}|^2 \langle b_{\mathbf{p}}^\dagger b_{\mathbf{p}} \rangle + |v_{-\mathbf{p}}|^2 \langle b_{-\mathbf{p}}^\dagger b_{-\mathbf{p}} \rangle \quad (2.64)$$

It can be proved [94] that this leads to an occupation number for the excited states of

$$n_{\mathbf{p}} = \frac{1}{2} \left(\frac{p^2/2m + mc^2}{\epsilon(p)} \right); \quad (2.65)$$

the total density of the condensate is, therefore

$$n_0 = \frac{N_0}{\mathcal{V}} \quad (2.66)$$

$$= \frac{1}{\mathcal{V}} \left(N - \sum_{\mathbf{p} \neq 0} n_{\mathbf{p}} \right) \quad (2.67)$$

$$= n \left(1 - \frac{8}{3} \sqrt{\frac{na^3}{\pi}} \right). \quad (2.68)$$

The non condensed part at $T = 0$ is called the quantum depletion, and its role will be crucial when we will consider beyond-mean-field interactions, in Section 2.4.

2.2.3. Gross-Pitaevskii equation

The preceding relations have been obtained from the Hamiltonian of (2.43), which, however, is valid for a uniform potential. It is instead relevant, especially since it is the most common situation in experiments, to look at the Bose gas in a harmonic potential, where

$$V_e(\mathbf{r}) = \frac{1}{2} m \omega_x^2 x^2 + \frac{1}{2} m \omega_y^2 y^2 + \frac{1}{2} m \omega_z^2 z^2. \quad (2.69)$$

An equation of motion can be obtained for ψ in a non uniform potential, by using an argument due to Gross [133, 134] and Pitaevskii [135]: writing the Heisenberg equation for our problem

$$i\hbar \frac{\partial}{\partial t} \hat{\Psi}(\mathbf{r}, t) = [\hat{\Psi}(\mathbf{r}, t), \hat{H}(\mathbf{r}, t) + V_e(\mathbf{r})], \quad (2.70)$$

2. Dual species Bose-Einstein condensates

where $\hat{H}(\mathbf{r}, t)$ is the Hamiltonian (2.43) in the position representation, and using the pseudopotential (2.45), we arrive at the Gross-Pitaevskii equation (GPE):

$$i\hbar \frac{\partial}{\partial t} \psi(\mathbf{r}, t) = \left(-\frac{\hbar^2 \nabla^2}{2m} + V_e(\mathbf{r}, t) + g |\psi(\mathbf{r}, t)|^2 \right) \psi(\mathbf{r}, t), \quad (2.71)$$

This equation has the shape of a Schrödinger equation, with an added self-interaction term that makes it non linear.

As with the Schrödinger equation, if the potential term is time independent, we can factorize the wave function by supposing

$$\psi(\mathbf{r}, t) = e^{i\mu t/\hbar} \psi(\mathbf{r}), \quad (2.72)$$

where the spatial part obeys the time independent GPE:

$$\left(-\frac{\hbar^2 \nabla^2}{2m} + V_e(\mathbf{r}) + g |\psi(\mathbf{r})|^2 \right) \psi(\mathbf{r}) = \mu \psi(\mathbf{r}). \quad (2.73)$$

By rearranging the terms, we can see that, in this equation, the energy functional \mathcal{E} is the grand-canonical energy

$$\mathcal{E} = E[\psi] + \mu \int |\psi(\mathbf{r})| \, d\mathbf{r} \quad (2.74)$$

$$= E[\psi] + \mu N, \quad (2.75)$$

with

$$E[\psi] = \int \frac{\hbar^2}{2m} |\nabla \psi|^2 + V_e(\mathbf{r}) |\psi|^2 + \frac{g}{2} |\psi|^4 \, d\mathbf{r} \quad (2.76)$$

so, the chemical potential is

$$\left(\frac{\partial \mathcal{E}}{\partial N} \right)_S = \mu. \quad (2.77)$$

Being nonlinear, in the general case the GPE has to be solved numerically [136, 137]; it is however possible to have a simple solution when the kinetic energy is negligible with respect to the internal energy [138]:

$$\frac{E_i}{E_k} \propto \frac{Na}{a_{\text{ho}}} \gg 1, \quad (2.78)$$

where a_{ho} is the typical length scale of the harmonic oscillator

$$a_{\text{ho}} = \sqrt{\frac{\hbar}{m\bar{\omega}}}, \quad (2.79)$$

and $\bar{\omega} = \sqrt[3]{\omega_x \omega_y \omega_z}$; this limit is called the Thomas-Fermi limit. In this case, we can neglect the kinetic term in (2.73), which becomes then an algebraic equation with solution

$$n(\mathbf{r}) = \begin{cases} \frac{1}{g} (\mu - V_e(\mathbf{r})) = n_0 \left(1 - \frac{x^2}{R_x^2} - \frac{y^2}{R_y^2} - \frac{z^2}{R_z^2} \right) & \text{if } V_e(\mathbf{r}) \leq \mu \\ 0 & \text{otherwise} \end{cases} \quad (2.80)$$

where the R_i are called Thomas-Fermi radii of the density function

$$R_i = \sqrt{\frac{2\mu}{m\omega_i^2}} \quad (2.81)$$

This density is of a similar form to that given by the Thomas-Fermi equation for the density of electrons in many-body systems [139]. We will use this approximation in the treatment of dipole oscillations in Section 4.1.

2.3. A condensate of two species

Having our theory expressed in form of the GPE (2.71) is advantageous not only for handling non-uniform potentials, but also because it is easy to generalize to the case of a mixture of two species, such as the one in our experiment. If we start from the Hamiltonian

$$H_i = -\frac{\hbar^2}{2m_i}\nabla^2 + V_{ei}(\mathbf{r}) + \sum_{j=1}^2 g_{ij} |\Psi_j|^2 \quad (2.82)$$

where the coupling parameters g_{ij} are now

$$g_{ij} = \frac{2\pi a_{ij}\hbar^2}{\mu_{ij}}, \quad (2.83)$$

and μ_{ij} is the reduced mass, we arrive at the coupled GPE [18]:

$$i\hbar \frac{\partial}{\partial t} \psi_1(\mathbf{r}, t) = \left(-\frac{\hbar^2 \nabla^2}{2m_1} + V_{e1}(\mathbf{r}, t) + g_{11} |\psi_1(\mathbf{r}, t)|^2 + g_{12} |\psi_2(\mathbf{r}, t)|^2 \right) \psi_1(\mathbf{r}, t) \quad (2.84)$$

$$i\hbar \frac{\partial}{\partial t} \psi_2(\mathbf{r}, t) = \left(-\frac{\hbar^2 \nabla^2}{2m_2} + V_{e2}(\mathbf{r}, t) + g_{12} |\psi_1(\mathbf{r}, t)|^2 + g_{22} |\psi_2(\mathbf{r}, t)|^2 \right) \psi_2(\mathbf{r}, t). \quad (2.85)$$

In (2.82) we have neglected the interspecies velocity coupling [140] $\mathbf{j}_i = \rho_{ij} \mathbf{v}_j$ which is otherwise important for the study of the Andreev-Bashkin effect [22].

2.3.1. Phases of the interacting condensates

In order to characterize the phase diagram of our mixture, we will study the topology of the condensates. In the most general case, the number of parameters complicates the argument beyond comprehensibility: as such, following the treatment in [141], we will consider a simplified model of a spherical trap, and add a gravitational field due to its relevance for experiments; this can be further simplified by assuming a cylindrical trap. We start from the coupled Thomas-Fermi equations in the region in which the condensates overlap:

$$g_{11} n_1(\mathbf{r}) + g_{12} n_2(\mathbf{r}) = \mu_1 - V_1(\mathbf{r}) \quad (2.86)$$

$$g_{22} n_2(\mathbf{r}) + g_{12} n_1(\mathbf{r}) = \mu_2 - V_2(\mathbf{r}), \quad (2.87)$$

2. Dual species Bose-Einstein condensates

we can write the solutions as

$$n_1 = \alpha_1 [R_1^2 - r^2 - (z - z_{c1}^2)] \quad (2.88)$$

$$n_2 = \alpha_2 [R_2^2 - r^2 - (z - z_{c2}^2)], \quad (2.89)$$

where R_i are the Thomas-Fermi radii for the respective traps, which are taken to be spherical harmonic traps, with a gravity term causing a displacement of the centres along z . The other quantities defined for (2.88) and (2.89) are: the normalization factors

$$\alpha_1 = g_{22} \frac{1 - \eta g_{12}/g_{22}}{2\delta g^2} \quad (2.90)$$

$$\alpha_2 = g_{11} \frac{\eta - g_{12}/g_{11}}{2\delta g^2}, \quad (2.91)$$

the centres

$$z_{c1} = -\frac{\eta g_{12}/g_{22}}{1 - \eta g_{12}/g_{22}}(z_{01} - z_{02}) \quad (2.92)$$

$$z_{c2} = -\frac{\eta}{\eta - g_{12}/g_{11}}(z_{01} - z_{02}), \quad (2.93)$$

where z_{0i} is the potential minimum for the i -th component, and the parameters

$$\eta = \frac{m_2 \omega_2^2}{m_1 \omega_1^2} \quad (2.94)$$

$$\delta g^2 = g_{11} g_{22} - g_{12}^2. \quad (2.95)$$

The poles of the α_i , that occur for $\delta g = 0$, define three regions, which correspond to different topologies:

1. $g_{12} < -\sqrt{g_{11}g_{22}}$. Here, the two condensates cannot overlap, as both α_i are negative, and thus would require $n_i = 0$. In this region, the condensates collapse under the attractive interspecies interactions [18, 142, 143].
2. $g_{12} > \sqrt{g_{11}g_{12}}$. For the same reasons of the previous case, the two condensates cannot overlap also in this range of scattering lengths, as they are immiscible [144, 145].
3. $-\sqrt{g_{11}g_{22}} < g_{12} < \sqrt{g_{11}g_{22}}$. Here, the two condensates can overlap in two ways, based on the relative magnitude of $\Delta R = |R_1 - R_2|$ and $\Delta z = |z_{c1} - z_{c1}|$:
 - a) External overlap, if $\Delta z > \Delta R$,
 - b) Internal overlap, if $\Delta z \leq \Delta R$. This kind of overlap, in its turn, can be total if

$$g_{12} < \eta \min \{g_{11}, g_{22}\}, \quad (2.96)$$

or partial otherwise.[¶]

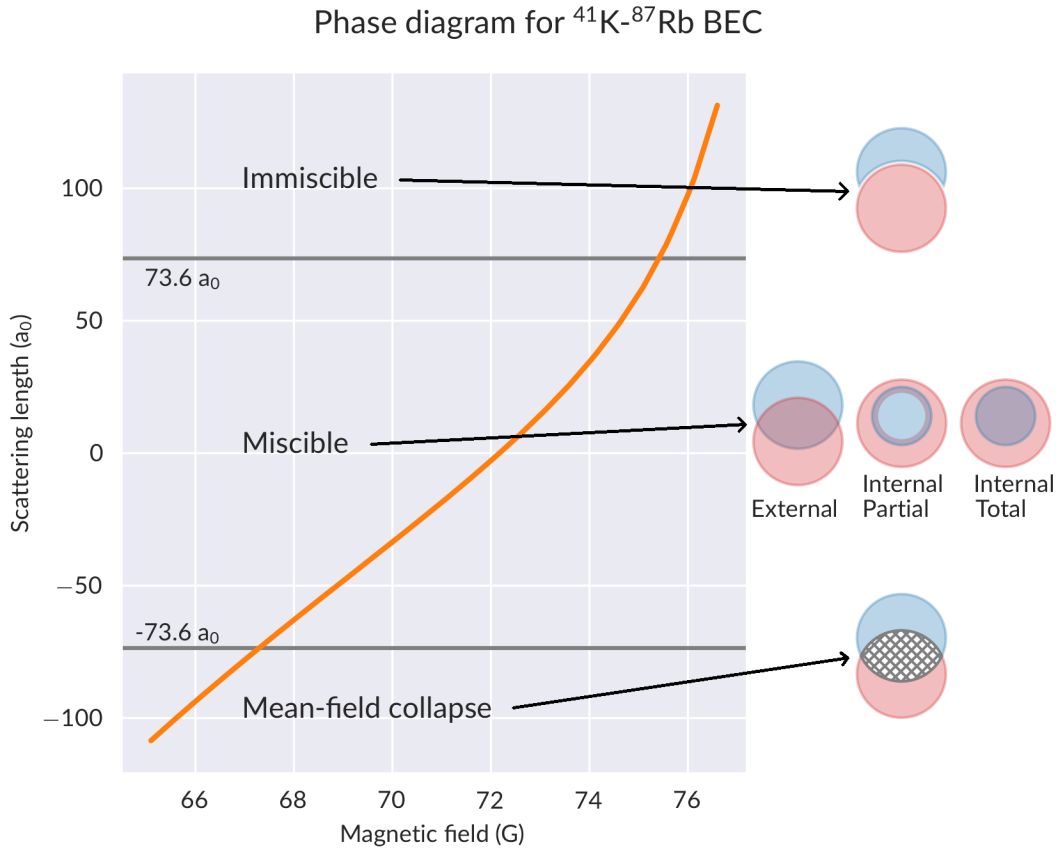


Figure 2.3.: Phase diagram for the ^{41}K - ^{87}Rb mixture. On the left, the three interaction regimes are shown, with a graph of the scattering length by which those regimes are defined superimposed. On the right, pictograms for each of the possible configurations are reported. The blue colour stands for the K condensate, while the red for the Rb one. Due to our trap configuration, the trap centre for K is usually on top of that of Rb. The gray crossed area in the mean-field collapse overlap region signifies that the two condensates cannot coexist there, according to mean-field theory, if both densities are not zero.

A depiction of the phase diagram for the ^{41}K - ^{87}Rb is in Figure 2.3. As the interspecies scattering length is $100.4a_0$ for ^{87}Rb and $62a_0$ for ^{41}K , we see that the critical value separating the three regions is $73.6a_0$. Therefore, the mean field collapse happens for $a_{12} < -73.6a_0$, and the immiscible regime is for $a_{12} > 73.6a_0$. The critical value for the total overlap, instead, depends on the trap frequencies, and is thus dependent on a particular trap configuration; given that partial internal overlap is possible only in the miscible regime, we can set an upper

[¶]For our mixture, this condition reads

$$g_{\text{K-Rb}} < \eta g_{\text{Rb-Rb}} \quad (2.97)$$

boundary for η to have total internal overlap threshold:

$$\eta g_{\text{Rb-Rb}} < \sqrt{g_{\text{K-K}} g_{\text{Rb-Rb}}} \quad (2.98)$$

which, in turn, gives an upper bound for the ratio of the trap frequencies in the direction of gravity:

$$\begin{aligned} \frac{\omega_{\text{K}}}{\omega_{\text{Rb}}} &= \sqrt{\frac{m_{\text{Rb}}}{m_{\text{K}}} \sqrt{\frac{g_{\text{K}}}{g_{\text{Rb}}}}} \\ &= \sqrt[4]{\frac{a_{\text{K}} m_{\text{Rb}}^3}{m_{\text{K}}^3 a_{\text{Rb}}}} \end{aligned} \quad (2.99)$$

$$= 1.56 \quad (2.100)$$

As we will see in Chapter 3, in the direction of gravity we have $\omega_z = 2\pi \times 130$ Hz for K and $\omega_z = 2\pi \times 67$ Hz, and therefore the condensates could not overlap without a compensation scheme: this is consistent with the calculations for the centres of the traps, which give a difference in the position of the minimum of $16 \mu\text{m}$ along the vertical axis; the way in which the two condensates are brought to overlap is explained in detail in Section 3.4.

2.3.2. Elementary excitations of a double BEC

In order to apply the Bogoliubov method to a mixture of two condensates, we will have to start by generalizing (2.54): for the i -th species, the Hamiltonian is

$$H_i = \frac{g_{ii}}{2\mathcal{V}} \hat{a}_{0i}^\dagger \hat{a}_{0i}^\dagger \hat{a}_{0i} \hat{a}_{0i} + \sum_{\mathbf{p}} \frac{p^2}{2m_i} \hat{a}_{\mathbf{p}i}^\dagger \hat{a}_{\mathbf{p}i} + \sum_j \frac{g_{ij}}{2\mathcal{V}} \sum_{\mathbf{p}} S_{ij}^{\text{int}}(\mathbf{p}), \quad (2.101)$$

where

$$S_{ij}^{\text{int}}(\mathbf{p}) = 4\hat{a}_{0j}^\dagger \hat{a}_{\mathbf{p}j}^\dagger \hat{a}_{0j} \hat{a}_{\mathbf{p}j} \quad (2.102a)$$

$$+ \hat{a}_{\mathbf{p}i}^\dagger \hat{a}_{-\mathbf{p}j}^\dagger \hat{a}_{0i}^\dagger \hat{a}_{0j} \quad (2.102b)$$

$$+ \hat{a}_{\mathbf{p}j}^\dagger \hat{a}_{-\mathbf{p}i}^\dagger \hat{a}_{0j}^\dagger \hat{a}_{0i} \quad (2.102c)$$

$$+ \hat{a}_{0i}^\dagger \hat{a}_{0j}^\dagger \hat{a}_{\mathbf{p}i}^\dagger \hat{a}_{-\mathbf{p}j} \quad (2.102d)$$

$$+ \hat{a}_{0j}^\dagger \hat{a}_{0i}^\dagger \hat{a}_{\mathbf{p}j}^\dagger \hat{a}_{-\mathbf{p}i} \quad (2.102e)$$

This equation can be diagonalized using generalized Bogoliubov transformations [146]

$$\hat{a}_{\mathbf{p}i} = u_{\mathbf{p}i} (\hat{\alpha}_{\mathbf{p}} + \hat{\beta}_{\mathbf{p}}) + v_{-\mathbf{p}i}^* (\hat{\alpha}_{\mathbf{p}}^\dagger + \hat{\beta}_{\mathbf{p}}^\dagger) \quad (2.103)$$

$$\hat{a}_{\mathbf{p}i}^\dagger = u_{\mathbf{p}i}^* (\hat{\alpha}_{\mathbf{p}}^\dagger + \hat{\beta}_{\mathbf{p}}^\dagger) + v_{-\mathbf{p}i} (\hat{\alpha}_{\mathbf{p}} + \hat{\beta}_{\mathbf{p}}) \quad (2.104)$$

where now we have two Bogoliubov quasiparticles, due to the lifting of the degeneracy between centre-of-mass motion and relative motion.

The resulting dispersion relation is [146]

$$\eta(\mathbf{p}) = \frac{1}{\sqrt{2}} \sqrt{\epsilon_1^2(p) + \epsilon_2^2(p) \pm \sqrt{(\epsilon_1^2(p) - \epsilon_2^2(p))^2 + \frac{2g_{12}p^2 n_1}{m_1} \cdot \frac{2g_{12}p^2 n_2}{m_2}}}, \quad (2.105)$$

where $\epsilon_i(p)$ is the single-species Bogoliubov dispersion (2.61).

In this expression, we can see the effect of the aforementioned lifted degeneration between the centre-of-mass and the relative motion, that is, the creation of two branches in the excitation spectrum. This effect is analogous, for example, to the separation of the phononic spectrum in solids into optic and acoustic branches when particles of two different masses are introduced [147]. We also note that, in similarity with what happens in the single species case, the lower branch can become unstable in the long wavelength limit: the condition for instability is here $g_{12} > \sqrt{g_{11}g_{22}}$, which is none other than the condition for condensate immiscibility.

2.4. Beyond-mean-field interactions and quantum droplets

The mean-field theory is generally adequate for treatment of phenomena in which the gas parameter na^3 is small, but it is insufficient in cases such as the mean-field collapse regime, in which the predicted densities diverge. However, it is possible to calculate, starting from (2.54), a first correction to the mean field energy, which becomes

$$E_g = g \frac{N^2}{2\mathcal{V}} \left(1 + \frac{16}{5} \frac{8}{3} \sqrt{\frac{na^3}{\pi}} \right), \quad (2.106)$$

the energy due to the second term in (2.106) is called the Lee-Huang-Yang (LHY) energy [148, 149], and corresponds to the zero point energy of the Bogoliubov quasiparticles [58], that causes also the quantum depletion; we also notice that both quantities share the $\sqrt{na^3}/\pi$ dependence, which is a signature of beyond-mean-field behaviour.

In a mixture, the energy density of the LHY term is [150]:

$$\frac{E}{\mathcal{V}} = \frac{8}{15\pi^2} m_1^{3/2} (g_{11} n_1)^{5/2} f\left(\frac{m_1}{m_2}, \frac{g_{12}}{g_{11}g_{12}}, \frac{g_{22}n_2}{g_{11}n_1}\right), \quad (2.107)$$

where f is a positive definite quantity, with the dimensions of a pure number. For the homonuclear case, in which $m_1 = m_2$, f assumes a simple form [58]:

$$f(1, y, z) = \frac{1}{\sqrt{32}} \sum \left(1 + z \pm \sqrt{(1-z)^2 + 4xy} \right)^{5/2}, \quad (2.108)$$

but, in case of an heteronuclear mixture, the expression is much more complicated [151]:

$$f(x, y, z) = \frac{15}{32} \int_0^{+\infty} k^2 \mathcal{F}(k, x, y, z) dk, \quad (2.109)$$

where

$$\mathcal{F}(k, x, y, z) = \sqrt{\mathcal{A}(k, x, z) + \sqrt{\mathcal{B}(k, x, y, z)}} + \sqrt{\mathcal{A}(k, x, z) - \sqrt{\mathcal{B}(k, x, y, z)}} - \frac{1+x}{2x}k^2 - (1+z) + \frac{1}{k^2} \left[1 + z^2x + 4yz \frac{x}{1+x} \right] \quad (2.110)$$

$$\mathcal{A}(k, x, z) = \frac{1}{2} \left[k^2 \left(1 + \frac{z}{x} \right) + \frac{k^4}{4} \left(1 + \frac{1}{x^2} \right) \right] \quad (2.111)$$

$$\mathcal{B}(k, x, y, z) = \frac{1}{4} \left[\left(k^2 + \frac{k^4}{4} \right) - \left(\frac{z}{x} k^2 + \frac{k^4}{4x^2} \right) \right]^2 + \frac{yzk^4}{x}. \quad (2.112)$$

It has been demonstrated that, due to the fact that f is always > 0 , the LHY interaction can stabilize a BEC mixture against collapse even in the $g_{12} < -\sqrt{g_{11}g_{22}}$ regime [58].^{||} To understand this, we can use a simple model for a quantum fluid [152]: the energy density can be written as

$$\epsilon(n) = -\frac{1}{2}\alpha n^2 + \frac{2}{5}\beta n^{5/2}, \quad (2.113)$$

with $\alpha > 0$, $\beta > 0$. The pressure for this is

$$P = -\epsilon(n) + n \frac{\partial \epsilon}{\partial n} = -\frac{1}{2}\alpha n^2 + \frac{3}{5}\beta n^{5/2}. \quad (2.114)$$

As the two terms in (2.113) have opposite sign, and scale with different powers of n , we are inclined to believe that this energy density may have a minimum at finite density. We can find this value of density n_d by imposing that the system is in mechanical equilibrium with vacuum, that is $P = 0$: from this, we get

$$n_d = \left(\frac{5\alpha}{6\beta} \right)^2, \quad (2.115)$$

which is the density value for our droplet. We also remark that the chemical potential

$$\mu(n_d) = -\alpha n_d + \beta n_d^{3/2} \quad (2.116)$$

$$= -\frac{1}{6}n_d\alpha \quad (2.117)$$

is negative, which means that the system is also stable against particle loss. A bound state stabilized by the LHY term in this way is called a quantum droplet.

Quantum droplets are a very peculiar state of matter, as they are stabilized by quantum fluctuations. The first droplets in atomic gases have been obtained experimentally in Dysprosium [59, 153] and Erbium [60] dipolar quantum gases, where the mean-field energy is given by the dipole-dipole interaction. They have been subsequently observed in gases with isotropic interactions in ^{39}K spin mixtures [61, 62], and in the ^{41}K - ^{87}Rb mixture [65].

These droplets receive their name from their analogous counterparts in liquid He, which also exist in equilibrium with vacuum, but for which the attractive and repulsive interactions giving rise to the stabilizing action are of a different nature [154]. Nevertheless, with their

^{||}In a single condensate, this cannot happen, as the LHY and mean-field density always have the same sign.

Helium counterparts they share the property of having a constant bulk density and a spherical shape, as can be seen from the expression for the droplet radius [58]

$$\frac{4\pi}{3}\tilde{R}^3 = \tilde{N}, \quad (2.118)$$

where \tilde{R} is measured in units of characteristic radius

$$\xi = \sqrt{\frac{3}{2} \frac{\sqrt{g_{11}} + \sqrt{g_{22}}}{\sqrt{g_{11}}} \frac{1}{m|\delta g|}} \quad (2.119)$$

and

$$\tilde{N}_i = \frac{N}{n_{i0}\xi^3}. \quad (2.120)$$

This is further confirmed by numerical solutions of the GPE for the ground state, which display a flat top profile that becomes larger for larger \tilde{N} [58].

From the simple model of (2.113), it would seem that a droplet always forms, regardless of other conditions. This is not the case: when the rescaled atom number $\tilde{N} < 22.55$, the bound state is metastable, and it is completely unstable for \tilde{N} below a critical atom number \tilde{N}_c , whose value is approximately 18.65 [58]. This behaviour is well reproduced by a liquid drop model [155]:

$$E_{\text{id}}(\tilde{N}) = E_B\tilde{N} + E_S\tilde{N}^{2/3} + E_C\tilde{N}^{1/3}, \quad (2.121)$$

where the name is due to the analogy with liquid droplets. The first term is called the bulk term, and it is the energy for a uniform liquid with energy per particle E_B ; in order to have a droplet, this term has to be negative. The second is called the surface term, and it accounts for the fact that atoms near the surface feel a different attraction with respect to those in the bulk, giving rise to a surface tension $T = E_S/(4\pi\tilde{R})$; this coefficient is generally positive. The last term is called the curvature term, and it is proportional to the radius of the droplet; while the physical interpretation is less immediate than that of the other two terms, its role is typically of limited in equilibrium droplets [152]. We can thus see that, for smaller \tilde{N} , the binding energy $E_{\text{id}}(\tilde{N})/N$ tends to a positive value, where the droplet can no longer subsist. This divides the phase diagram of quantum gases in the mean-field collapse regime into two regions: a first one, for higher numbers of atoms, where a droplet forms, and another, for lower \tilde{N} , where there is no stable self-bound state but for which, nevertheless, beyond-mean-field interactions are comparable to their mean-field counterpart, called a LHY gas. An example of this phase diagram, for the specific case of the ^{41}K - ^{87}Rb mixture, is shown in Figure 2.4.

The implications of this last point are of crucial importance for the experimental study of quantum droplets: at the high densities that these bound states attain, three body collisions start to become important, and recombination events greatly limit the lifetime of the droplet. For ^{39}K , the longest measured lifetimes for a droplet have been of about 25 ms while keeping the droplets on a light sheet [61]; this is approximately the same lifetime as was observed in the ^{41}K - ^{87}Rb mixture in free space, although numerical simulations of the same systems have predicted lifetimes of more than an order of magnitude longer [65]. In both platforms, droplets in waveguides have been observed after substantially longer times [64, 65]. The longest lifetimes to date have been observed in dipolar quantum gases, where stable droplet cores have been observed after up to 500 ms–1000 ms [60].

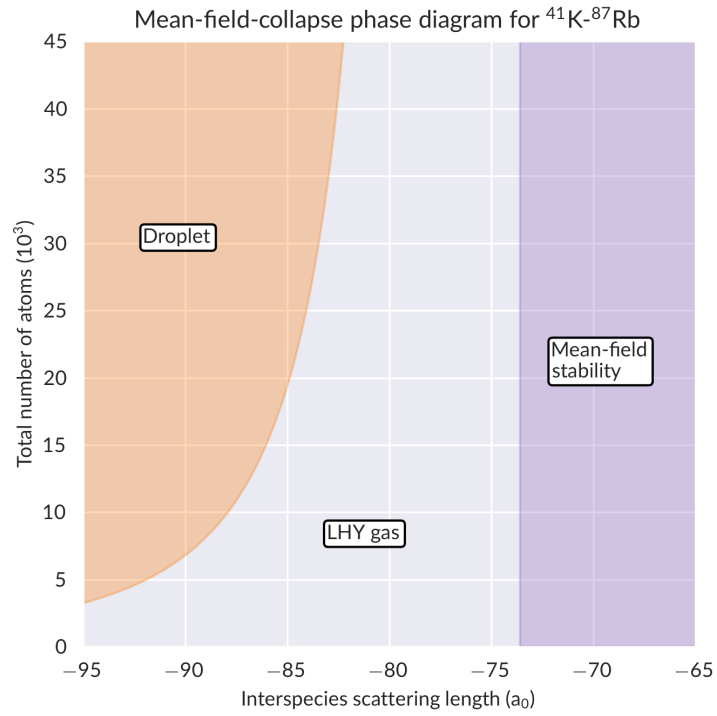


Figure 2.4.: Phase diagram of the ^{41}K - ^{87}Rb BEC in the strongly attractive regime, as a function of the interspecies scattering length a_{12} and of the total number of atoms $N_1 + N_2$. For these parameters, we can define three regions: a first one is the mean-field stable region, where $\delta g > 0$, and the interspecies interactions are not strong enough to overcome the intraspecies repulsion. On the left, there is the mean-field collapse region, in which, above a certain total number $N_c(a_{12})$, the LHY interaction is strong enough to stabilize the gas, thus forming a droplet. Below that critical number, the state is an LHY gas, for which beyond-mean-field interaction are important, but below the threshold of creating a self bound state.

Preparation of a double species Bose-Einstein Condensate

The preparation of a double condensate of ^{41}K and ^{87}Rb in the lowest hyperfine state ($F = 1, m_F = 1$) is the first step in any of the experimental investigations with our mixture.

In this chapter, we will illustrate how this double condensate is obtained. We will begin with a description of the experimental apparatus (Section 3.1), and of the cooling sequence (Section 3.2), at the end of which a double condensate in the $F = 2, m_F = 2$ state is obtained; this is because we find advantageous to employ an hybrid optical and magnetic evaporation technique on a magnetically trappable state [156]. The BECs are then transferred to the desired hyperfine state; the details of this transfer are reported in Section 3.3. The final step of the preparation is to counteract gravity and overlap the condensates, such that the effect of the tunable interspecies interaction can be appreciated (Section 3.4).

After this preparation, the interactions can be tuned in a wide range of values, according to the phase diagram in Figure 2.3. Some examples of condensates obtained with this procedures can be seen in Figure 3.1.

3.1. Experimental apparatus

In this section, we describe the experimental apparatus that has been used for the work of this thesis. The apparatus is nearly identical to that reported in for [65, 156], except for a new and improved optical trapping setup, which substitutes the inclined geometry mentioned in the aforementioned articles with a planar one.

The machine is distributed among two tables, one for the laser sources used for cooling and probing the atoms (see Subsection 3.1.2 for the sources, and Subsection 3.1.3 for the frequency locking), and another which houses both the far-detuned optical dipole optics and the vacuum setup (see, respectively, 3.1.4 and 3.1.1), to which the magnetic field coils are fastened (described in 3.1.5).

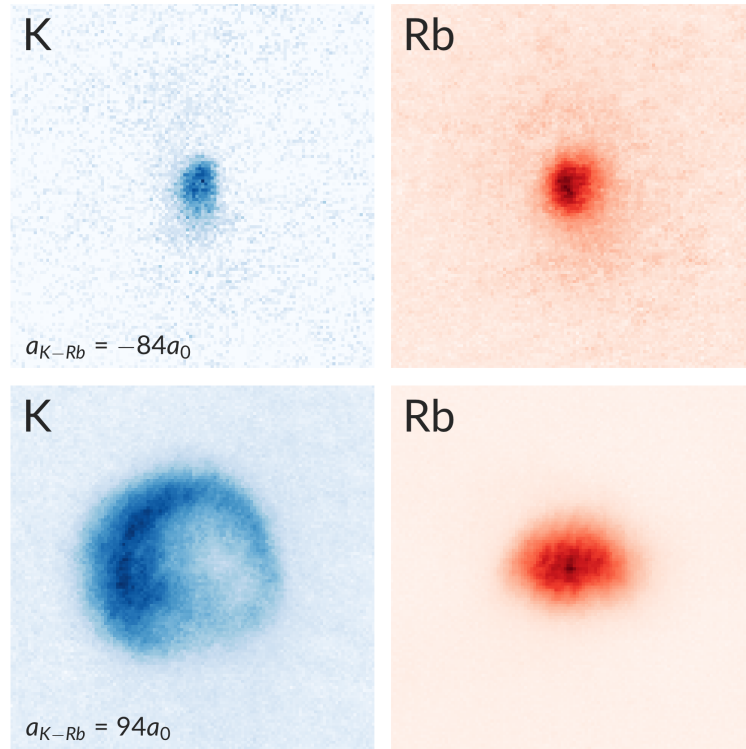


Figure 3.1.: Double BEC in the lowest hyperfine state in two different regimes for interactions: beyond mean field collapse with $a_{K-Rb} = -84a_0$ (first row), and immiscible at $a_{K-Rb} = 94a_0$ (second row). In both cases, the K condensates are imaged after 27 ms of time of flight expansion (TOF), and the Rb condensates are imaged after 30 ms TOF, using absorption imaging. In the mean field collapse case, the total atom number is of the order of 5×10^4 , whereas in the immiscible case we have around 3×10^5 atoms.

3.1.1. Vacuum apparatus

A schematic view of the apparatus is shown in figure 3.2. There are two vacuum chambers in the setup. The first encountered by the atoms is the 2D MOT chamber, which is directly connected to the two reservoirs; those reservoirs are metallic samples at natural isotopic abundance. In order for K to achieve a reasonable partial pressure of approximately 4×10^{-8} Torr, its reservoir is heated to 36°C , while Rb at room temperature (25°C) already has an acceptable vapour pressure of about 4×10^{-7} Torr [157]. An ion pump maintains the vacuum in this chamber at pressures of the order of 1×10^{-8} Torr. The thermal atomic beams are transversally cooled here, and then are pushed by a resonant beam into a differential pumping section, and then into the second chamber. In order to prevent deposition of K, the entrance to the differential pumping section is further heated to 50°C .

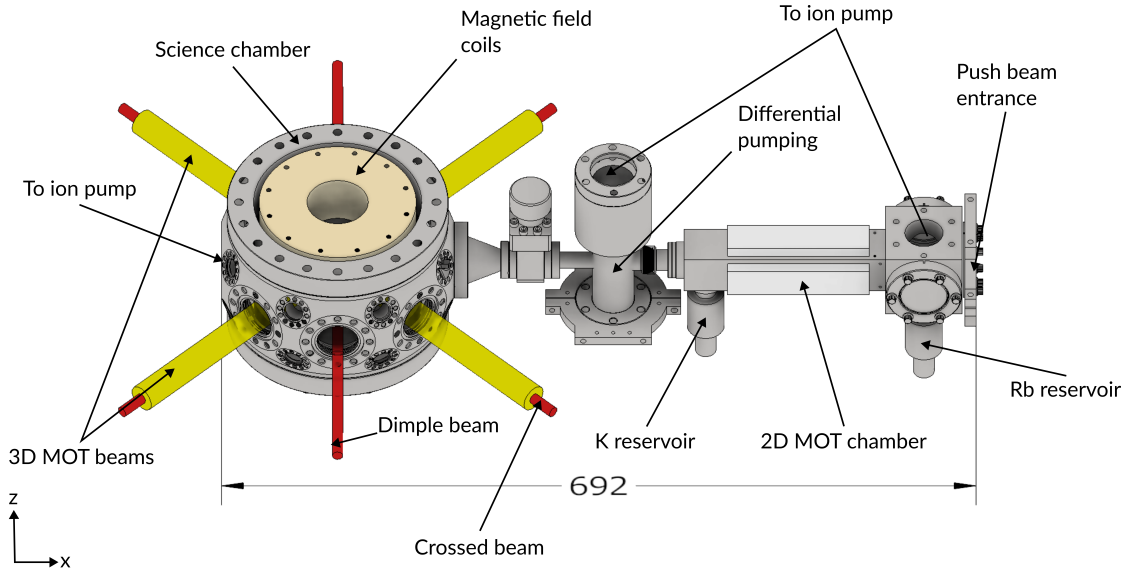


Figure 3.2.: Simplified view of the experimental apparatus. The vacuum setup is described in Subsection 3.1.1; shown here are the MOT chambers, the differential pumping section, the reservoirs, and the ports for the ion pumps. The yellow cylinders represent the 3D MOT beams; only the two horizontal beams are shown, while the third beam, along the vertical direction, is not visible. The coils for the production of the magnetic fields, as described in 3.1.5, are here represented by their outer casing. The two sets of coils are coaxial, and their axis is along the vertical direction.

After the differential pumping section, the atoms are pushed into the science chamber. This section is maintained at a higher vacuum by two combined ion and non evaporable getter (NEG) pumps*; the pressure there is of the order of 1×10^{-11} Torr.

3.1.2. Laser sources

All laser sources needed for optical cooling are arranged on a dedicated table, on which the laser beam is separated into all the needed independent beams, amplified with the usage of taper amplifiers, and modulated by acousto-optic modulators (AOMs). A simplified scheme of the sources table can be seen in figure 3.3.

To cool both species, we use the respective D2 transitions, connecting the $^2S_{1/2}$ and $^2P_{3/2}$ levels. Due to the hyperfine structure of these levels, two wavelengths are actually needed: one to address the $|^2S_{1/2}, F=1\rangle \rightarrow |^2P_{3/2}, F=2\rangle$ transition, and one to address the $|^2S_{1/2}, F=2\rangle \rightarrow |^2P_{3/2}, F=3\rangle$ transition [158]; we call these two light beams, respectively, the *repumper* and the *cooler*. The cooling wavelengths for Rb and K can be seen in figure 3.4.

For K, the source is a Toptica TA Pro Extended Cavity Diode Laser (ECDL) with a wavelength of 767 nm. From this single source, both cooler and repumper lines are derived by modulating with AOMs, as the hyperfine splitting is 254 MHz. On the other hand, Rb has two laser

*SAES NexTorr D200-5

3. Preparation of a double species Bose-Einstein Condensate

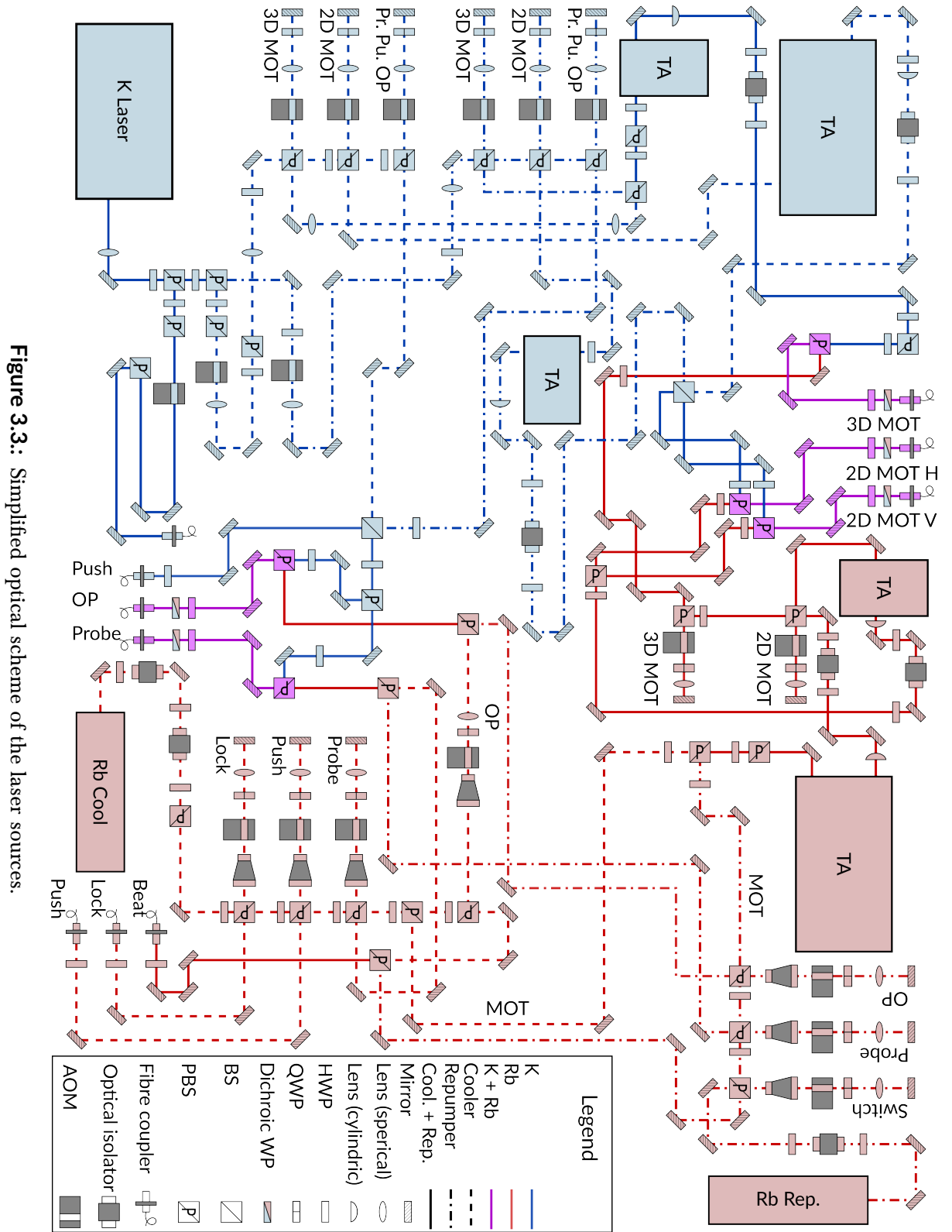


Figure 3.3.: Simplified optical scheme of the laser sources.

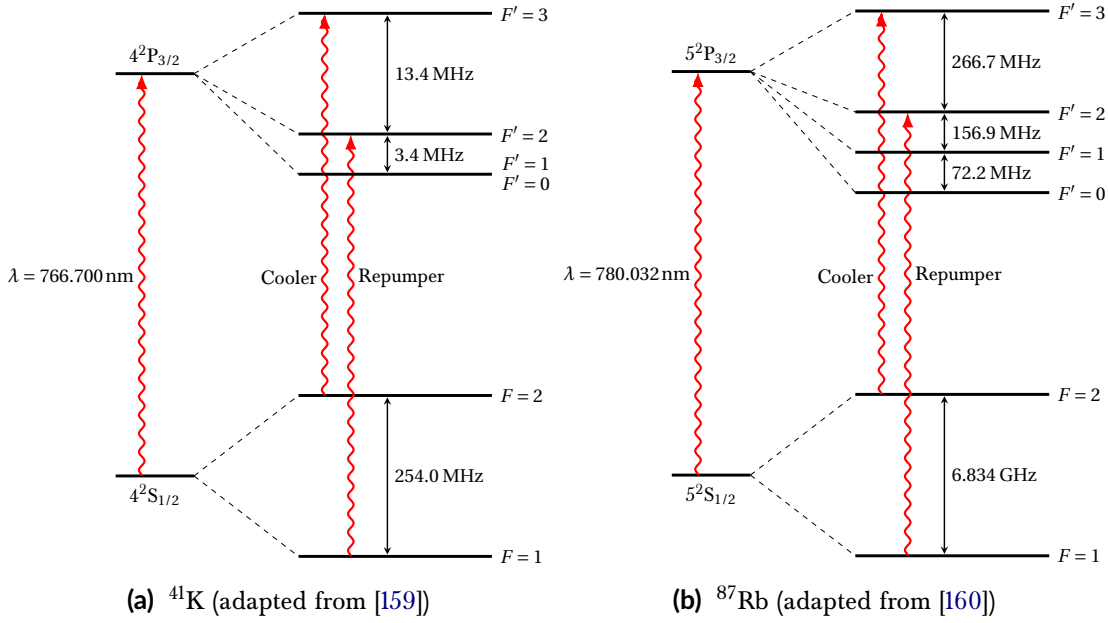


Figure 3.4.: Energy levels of the ^{41}K and ^{87}Rb D2 lines. The cooler and repumper transitions are highlighted. For ^{41}K , the hyperfine structure of the excited state is badly resolved, with a total splitting of about 16.8 MHz. For this, both cooler and repumper lights are usually red detuned with respect to the whole $^2\text{P}_{3/2}$ manifold; such a scheme is customary in laser cooling of K [158].

sources, one for the cooler wavelength, which is a Toptica DL 100 Pro ECDL, and another for the repumper wavelength, which is a Toptica DL 100 Distributed Feedback (DFB) laser; this is because the hyperfine splitting is 6.8 GHz, and such a frequency is outside of the band of typical AOMs.

A small fraction of the 1.3 W output power of the K laser is picked off and sent to the locking setup (not shown in figure 3.3). Then, the light is further separated into cooler and repumper branches. From each of those, three independent beams are derived: one for the 3D MOT, one for the 2D MOT, and one for Probe, Push and OP beams. The 3D MOT cooler and repumper paths join before being injected into a Tapered Amplifier (TA) with nominal power of 500 mW. The 2D MOT beams are separately amplified by two TAs, each with nominal power of 500 mW, and are then joined together. The Push-Probe-OP beam separates into its three constituents, in each of whom the cooler and repumper components are overlapped. All of these lights, apart from the push beam, are overlapped with the corresponding Rb beams and then injected into optical fibres.

The Rb cooling laser is split into five independent beams: the first is sent to the frequency locking setup (not shown in figure 3.3), the second is used for the push beam, the third for the probe beam, the fourth for the MOT, and the fifth is used for the OP beam. A residual is picked off from the last cube, and is then used as a reference for the beat note locking of the repumper laser. For the repumper laser, first a small portion is picked off for usage in the

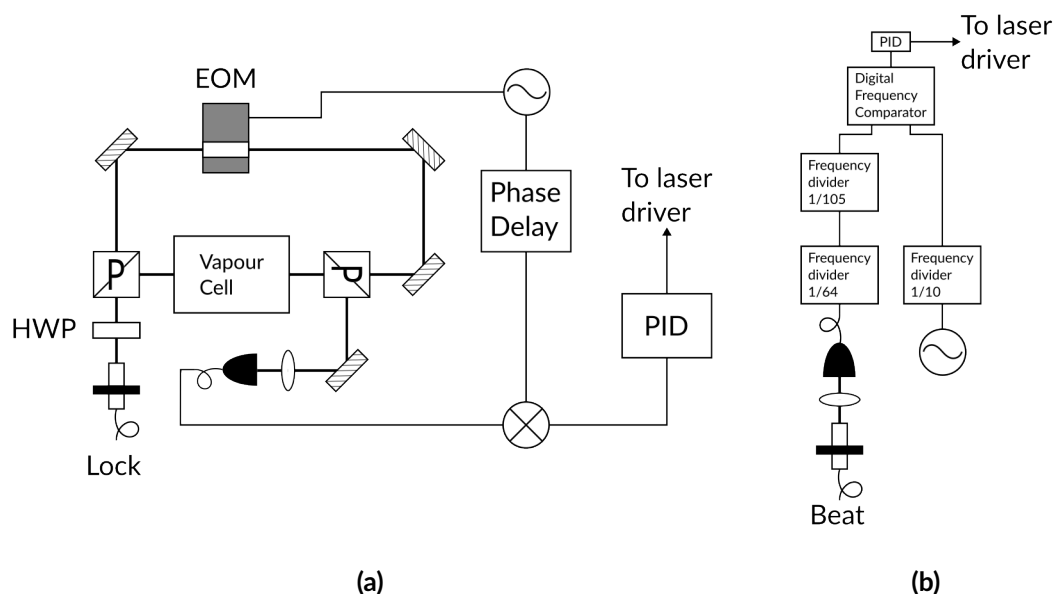


Figure 3.5.: Optical schemes for laser locking using modulation transfer spectroscopy (a) and a beat note scheme (b). The fibre couplers labelled "Lock" and "Beat" come from the respective couplers shown in Figure 3.3.

beat note stabilization, then the light is sent to a common switch AOM, which can be used both to switch on or off the whole Rb repumper line, as well as to add some further frequency offset (this is particularly useful for the high-field imaging of Rb). The repumper beam is then divided in a Probe, and OP and a MOT beam. The MOT beams of both wavelengths are joined together before being injected into a TA with nominal power of 500 mW. The light amplified in such a manner is further divided into a 3D MOT line and a 2D MOT line, with most of the power going into the former, as the latter is then amplified again by another TA, this with nominal power of 1 W. The 2D MOT beams are then separated into a vertical and an horizontal branch, which are then injected into the respective fibres, after being mixed with the K light.

3.1.3. Laser locking

Due to the inevitable fluctuations in the external environment, laser frequencies need to be locked to an absolute reference. For two of the three sources, namely the Rb cooling laser and the K laser, we use an atomic spectroscopy technique, whereas the Rb repumper is locked to its cooler with an offset technique; the optical schemes for the aforementioned techniques can be seen in Figure 3.5.

Modulation transfer spectroscopy is a variation on the basic scheme of saturated absorption spectroscopy. In saturated absorption spectroscopy, the atomic sample is illuminated with two counter-propagating laser beams, the pump and the probe. At a certain laser frequency ω_L , the atoms with velocity $v = (\omega_L - \omega_0)/k_L$ (where ω_0 is the atomic transition frequency) are

excited by the pump beam, which is the stronger of the two; at the same time, the probe beam interacts with those atoms for which $\nu = -(\omega_L - \omega_0)/k_L$. When $\omega_L = \omega_0$, the atoms pumped in the excited state create a dip in the absorption signal seen by the probe; this dip only comprises the part of the ensemble for which $\nu = 0$ [161].

The specificity of modulation transfer spectroscopy is that the pump beam is phase modulated by an electro-optic modulator (EOM); the modulation of the pump is then transferred to the probe beam via wave mixing, enabled by the non-linearity of the atomic medium [162]. For an input field of frequency ω_L , modulated at frequency ω_m ,

$$E = E_0 \sin(\omega_L t + \epsilon \sin \omega_m t) \quad (3.1)$$

we obtain a spectroscopic signal on the probe (considering only the first side bands) [163]

$$\begin{aligned} S(\omega_m) \propto & \frac{J_0(\epsilon)J_1(\epsilon)}{\sqrt{\Gamma^2 + \omega_m^2}} \quad (3.2) \\ & \times [(L_{-1} - L_1 + L_{-1/2} - L_{1/2}) \cos(\omega_m t + \phi) \\ & + (D_1 + D_{-1} - D_{1/2} - D_{-1/2}) \sin(\omega_m t + \phi)], \end{aligned}$$

where

$$L_n = \frac{\Gamma^2}{\Gamma^2 + (\omega_0 - \omega_L - n\omega_m)^2}, \quad (3.3a)$$

$$D_n = \frac{\Gamma(\omega_0 - \omega_L - n\omega_m)}{\Gamma^2 + (\omega_0 - \omega_L - n\omega_m)^2}, \quad (3.3b)$$

Γ is the natural transition line width, and J_i is the i -th Bessel function. The signal is then demodulated with a lock-in amplifier, where an appropriate choice of the phase lag between the modulating and demodulating signal maximizes the derivative component (3.3a) with respect to (3.3b). The resulting error signal is then sent to a PID controller for correction, using both the piezoelectric transducer of the laser cavity and the laser current. The advantage of modulation transfer spectroscopy, as opposed to similar schemes, is that the dispersion signal background is flat [164], and, as such, is particularly fit for usage in stabilization schemes.

The beat note scheme is conceptually and optically simpler. Here, light from the two laser sources is collected on the same photodiode, where the resulting signal is proportional to the intensity

$$I \propto \sin(\Delta\omega t + \phi), \quad (3.4)$$

where $\Delta\omega$ is the frequency difference between the cooler and repumper light which, in the case of ^{87}Rb , is 6.567 GHz. The photodiode signal passes through a chain of frequency dividers, and is then compared to a reference signal. The frequency of the repumper light is then adjusted by acting on the laser diode current.

3.1.4. Optical dipole trap

A 1064 nm, 30 W Azurlight System ALS-IR-976 laser is used to create the optical potentials needed for both the evaporative cooling and the trapping of the condensate. A scheme of the trapping light setup is visible in figure 3.6.

The laser beam, after some conditioning, is split in two: one called the *dimple* beam, and the other called the *crossed* beam. The portion of the intensity which goes to each beam is controllable with a motorized rotating wave plate[†], which can be moved between two predefined positions during the preparation sequence using a TTL signal. Each of the two beams is then modulated by an AOM, and injected into an optical fibre. The AOMs serve both for controlling the intensity of the beams (each separately), and to avoid interference effects between the crossed and dimple beams: for this, one of them is aligned to use the +1 diffraction order, and the other to use the -1 diffraction order; the signal entering each AOM is around 100 MHz, which results in a detuning of around 200 MHz. Each beam is then injected into a fibre, that brings the light closer to the vacuum chamber, and also provides a good amount of shaping.

After the fibres, a small portion of each beam is redirected to a photodiode, which constitutes the sensing part of a PID control loop, that acts on the amplitude of the radio frequency injected in the AOMs, in order to stabilize the power in the trapping beams. The crossed beam goes to a linear photodiode, and, as such, the power output for this beam, as a function of the photodiode voltage, is $P = mV_{\text{pd}} + P_0$; typical values for the parameters are $P_0 = 67$ mW, and $m = 587$ mWV⁻¹. The dimple beam goes to a logarithmic photodiode, for which the power output of the beam, as a function of the photodiode voltage, is $P = P_0 + Ae^{V_{\text{pd}}/\Gamma}$; typical values for the parameters are $P_0 = 1.5$ mW, $A = 7 \times 10^{-7}$ W, $\Gamma = 0.087$ V. The dimple beam is then magnified 1.5 times with a telescope ($f_1 = -100$ mm, $f_2 = 150$ mm), before being focalized by a $f = 500$ mm lens, obtaining a waist of 79 μm , and can provide a maximum of around 5 W of power on the atomic sample. The crossed beam, instead, is magnified 2 times with a telescope ($f_1 = -100$ mm, $f_2 = 200$ mm), and then focalized with a $f = 750$ mm lens, resulting in a waist of 95 μm , and can provide a maximum power of around 6 W on the atoms. The beams intersect in the horizontal plane at an angle of 45°, as shown in figure 3.6.

Given the theoretical framework for trapped gases, we are interested in knowing the harmonic oscillator trap frequencies for a potential like (2.69) given a certain trap configuration. To do so, we shall approximate the real potential produced by the optical dipole trap with an harmonic approximation:

$$U(\mathbf{x}) \approx \frac{1}{2} \mathbf{x}^T \mathbf{H}(U_d)(\mathbf{x}_0) \mathbf{x}, \quad (3.5)$$

where $\mathbf{H}(U_d)(\mathbf{x}_0)$ is the Hessian matrix of the potential calculated at \mathbf{x}_0 . By comparing (3.5) with (2.69), we find that

$$\omega_i = \sqrt{\frac{h_i}{m}}, \quad (3.6)$$

where h_i is the i -th eigenvalue of $\mathbf{H}(U_d)$ (which we suppose is not degenerate). In our case of a far detuned laser, with linear polarization, and of an alkali atom with nuclear spin $I = 3/2$, we have that the optical dipole potential is [165]

$$U_d(\mathbf{x}) = \frac{\pi c^2 \Gamma}{2\omega_0^3} \underbrace{\left(\frac{2}{\omega - \omega_{D2}} + \frac{1}{\omega - \omega_{D1}} \right)}_{\mathcal{F}} I(\mathbf{x}), \quad (3.7)$$

[†]Thorlabs PRMTZ8

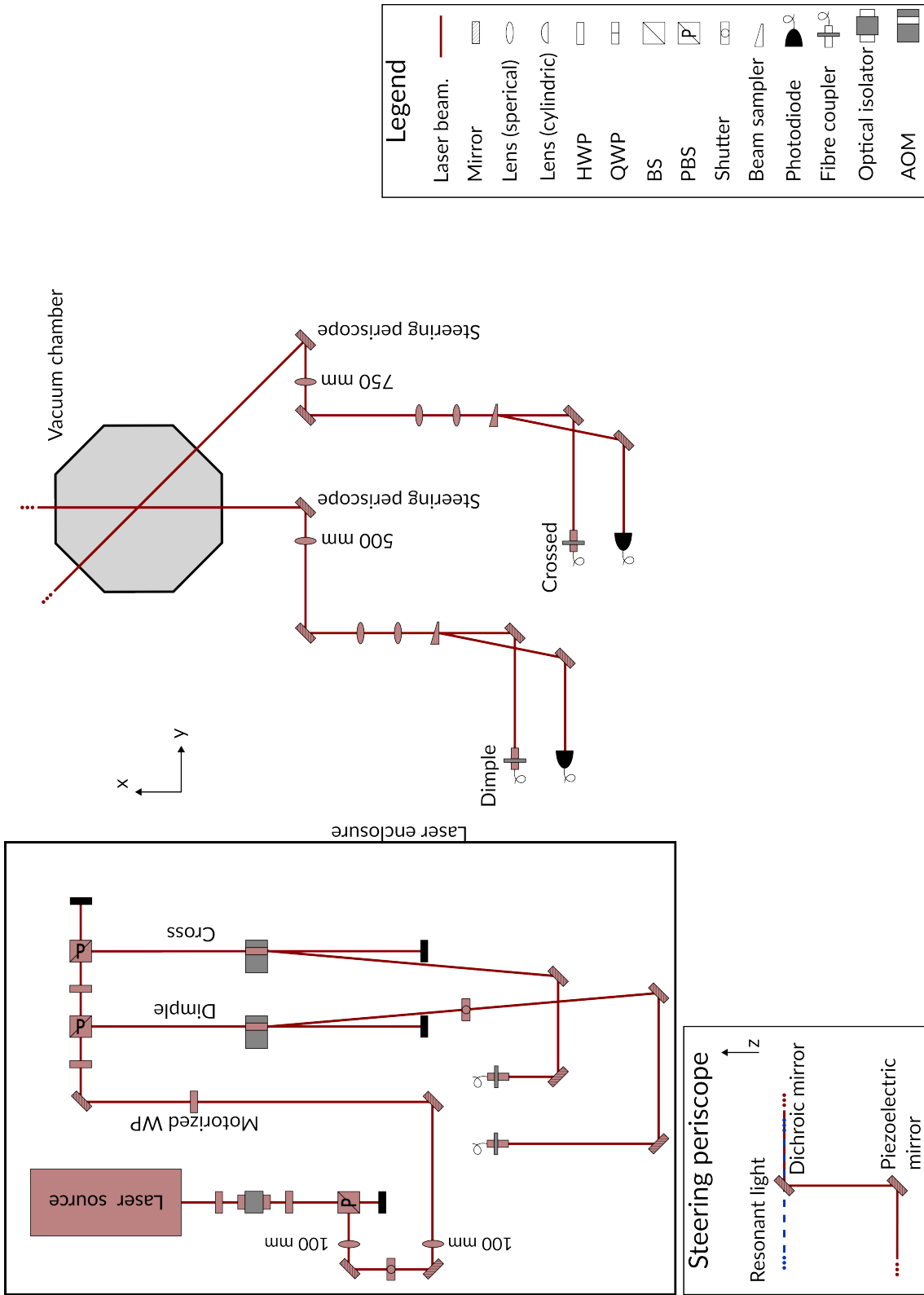


Figure 3.6.: Optical scheme of the trapping laser.

3. Preparation of a double species Bose-Einstein Condensate

where ω_{D1} and ω_{D2} are the angular frequencies of the corresponding transitions in each species.[‡] Given that is the only spatially varying part, the intensity profile is the only non constant factor in the calculation of the Hessian. The intensity distribution of the trapping light can be approximated by a Gaussian beam [166]:

$$I(x, y, z) = \underbrace{\frac{2P_0}{\pi w_0^2}}_{I_0} \left(\frac{w_0}{w(x)} \right)^2 \exp\left(-2 \frac{z^2 + y^2}{w(x)^2}\right), \quad (3.8)$$

where

$$w(x) = w_0 \sqrt{1 + \left(\frac{x}{x_R}\right)^2}, \quad (3.9)$$

and w_0 is the waist at the origin, P_0 the total beam power, and

$$x_R = \frac{\pi w_0^2}{\lambda} \quad (3.10)$$

is the *Rayleigh length* of the laser beam, in which λ is the laser wavelength in the medium in which the propagation takes place. Calculating the Hessian for $I(\mathbf{x})$, we find

$$\mathbf{H}(I)|_{\mathbf{x}=0} = -2I_0 \begin{pmatrix} \frac{1}{x_R^2} & 0 & 0 \\ 0 & \frac{2}{w_0^2} & 0 \\ 0 & 0 & \frac{2}{w_0^2} \end{pmatrix} = \begin{pmatrix} b & 0 & 0 \\ 0 & a & 0 \\ 0 & 0 & a \end{pmatrix} \quad (3.11)$$

The geometry of our trap is such that we have two trap beams which cross at a 45° angle; by linearity of the Hessian matrix, we can write

$$\mathbf{H}(I_{\text{ctd}})|_{\mathbf{x}=0} = \begin{pmatrix} b_d + \frac{a_c + b_c}{2} & \frac{b_c - a_c}{2} & 0 \\ \frac{b_c - a_c}{2} & a_d + \frac{a_c + b_c}{2} & 0 \\ 0 & 0 & a_c + a_d \end{pmatrix}, \quad (3.12)$$

where c and d subscripts stand for crossed and dimple beams, respectively. The frequencies, extracted from the eigenvalues of (3.12), are thus

$$\omega_z = \sqrt{\frac{\mathcal{F}}{m} (a_c + a_d)} \quad (3.13)$$

$$\omega_{x,y} = \sqrt{\frac{\mathcal{F}}{2m} \left((a_c + b_c) + (a_d + b_d) \mp \sqrt{(a_c - b_c)^2 + (a_d - b_d)^2} \right)} \quad (3.14)$$

Given that the typical powers in our trap are $P_d = 200$ mW and $P_c = 500$ mW, we have for Rb trap frequencies $(\omega_x, \omega_y, \omega_z) = 2\pi \times (39, 95, 103)$ Hz, and for K trap frequencies of $(\omega_x, \omega_y, \omega_z) = 2\pi \times (53, 130, 140)$ Hz. This is due to the different values of the factor \mathcal{F}/ω for the two species.

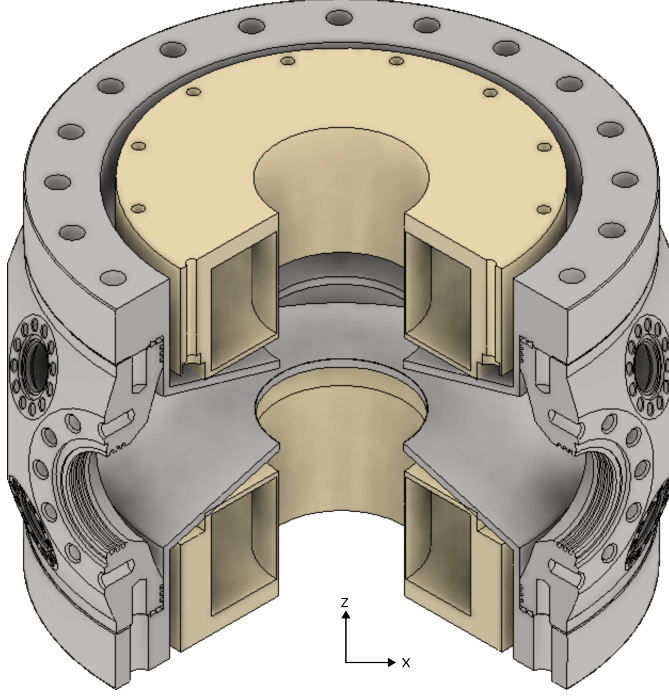


Figure 3.7.: Expanded cutout view of the vacuum chamber (see 3.2) with emphasized position of quadrupole and Feshbach coil housing. The axes are in the same orientation as in Figure 3.2.

3.1.5. Magnetic fields

In order to prepare and manipulate the atoms, the apparatus is equipped with two pairs of coils. The first pair of coils is in a quadrupole configuration, and generates a field which, to first order, is [167]:

$$\mathbf{B}(x, y, z) = Ib' \left(-\frac{x}{2}, -\frac{y}{2}, z \right), \quad (3.15)$$

where I is the current, and $b' = 0.56 \text{ G/cm/A}$. Those coils are called the *quadrupole* coils, and have their symmetry axis along the vertical direction, and the centre of the quadrupole approximately at the centre of the vacuum chamber. Their current is supplied by an Agilent 6617A power supply, and an additional is an Agilent N5744A power supply, in parallel, which has a faster slew rate. The current sign can be additionally flipped by using an H-bridge, which can be triggered with a TTL command.

Another set of coils is set up in an Helmholtz configuration, which is used to give a uniform magnetic field along its symmetry axis. Due to construction constraints, the distance between the coils is not equal to their radius, and so the magnetic field is

$$\mathbf{B}(x, y, z) = I \begin{pmatrix} -b_2 x z \\ -b_2 y z \\ b_0 + b_2 \left(z^2 - \frac{x^2}{2} - \frac{y^2}{2} \right) \end{pmatrix} \quad (3.16)$$

[‡]We neglect all excited levels out of the 5^2P_x manifold.

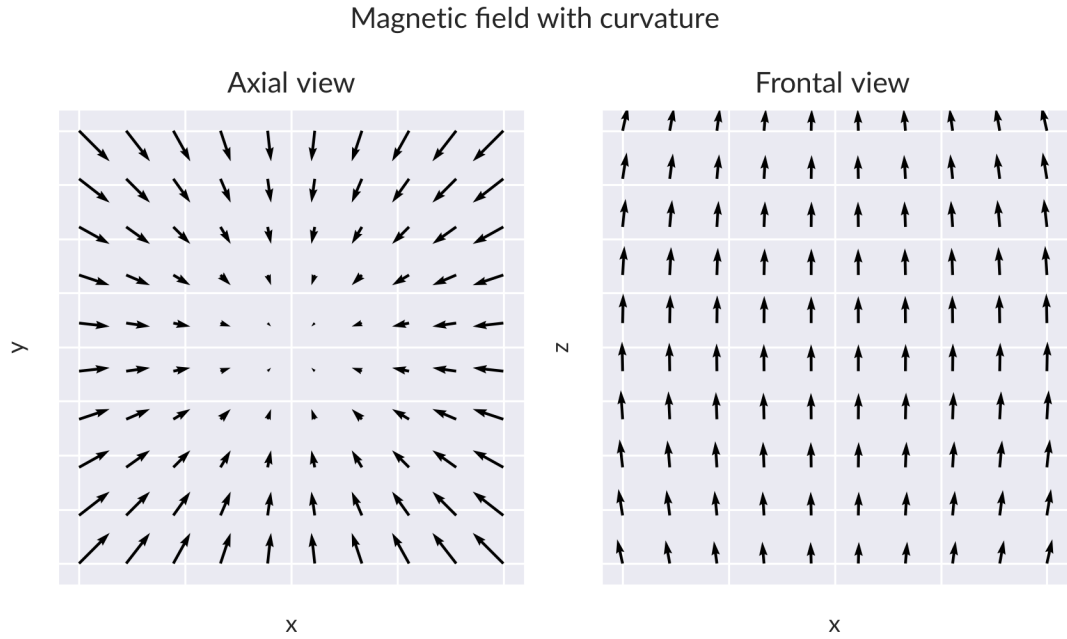


Figure 3.8.: Depiction of the field of (3.16) in two planes. The axial view depicts the magnetic field in the x, y plane, with a positive offset in the z direction to show the curvature (for a negative offset, the curvature is in the other direction). The frontal view depicts the magnetic field in the x, z plane, without any offset. The coefficient ratio b_2/b_0 is exaggerated with respect to the actual values for our experiment to make the curvature more evident.

where $b_0 = 2.40 \text{ G/A}$, and $b_2 = 1.678 \times 10^{-1} \text{ G/cm/A}$; a graph of the field is shown in Figure 3.8. Given their main purpose, these are called the *Feshbach* coils, and are powered by a Delta SM18-220 power supply.

There are three additional pairs of coils, which are used for compensation of external magnetic fields, and to provide an offset field during the quadrupole transfer.

3.2. Cooling sequence

The cooling sequence starts with the loading of the 3D MOT from the 2D MOT, when the atoms are pushed into the science chamber by a *push* beam: the K MOT is loaded for about 8 s, and the Rb MOT is loaded for about 6 s, and happens simultaneously with the last part of the K MOT loading.

Typical orders of magnitude for the number of atoms in the MOTs are 10^9 - 10^{10} atoms for Rb and 10^7 - 10^8 for K. The number of atoms in each MOT can be controlled by a Schmitt trigger stabilization scheme. A Schmitt trigger is a type of digital comparator that compares an input signal I to a threshold T . If $I < T - \Delta T$, where $\Delta T > 0$, then the output is the logical low state, and if $I > T + \Delta T$, the output is the logical high state; if $T - \Delta T < I < T + \Delta T$, then the output is at the same logical level as it was at the previous instant. The Schmitt trigger

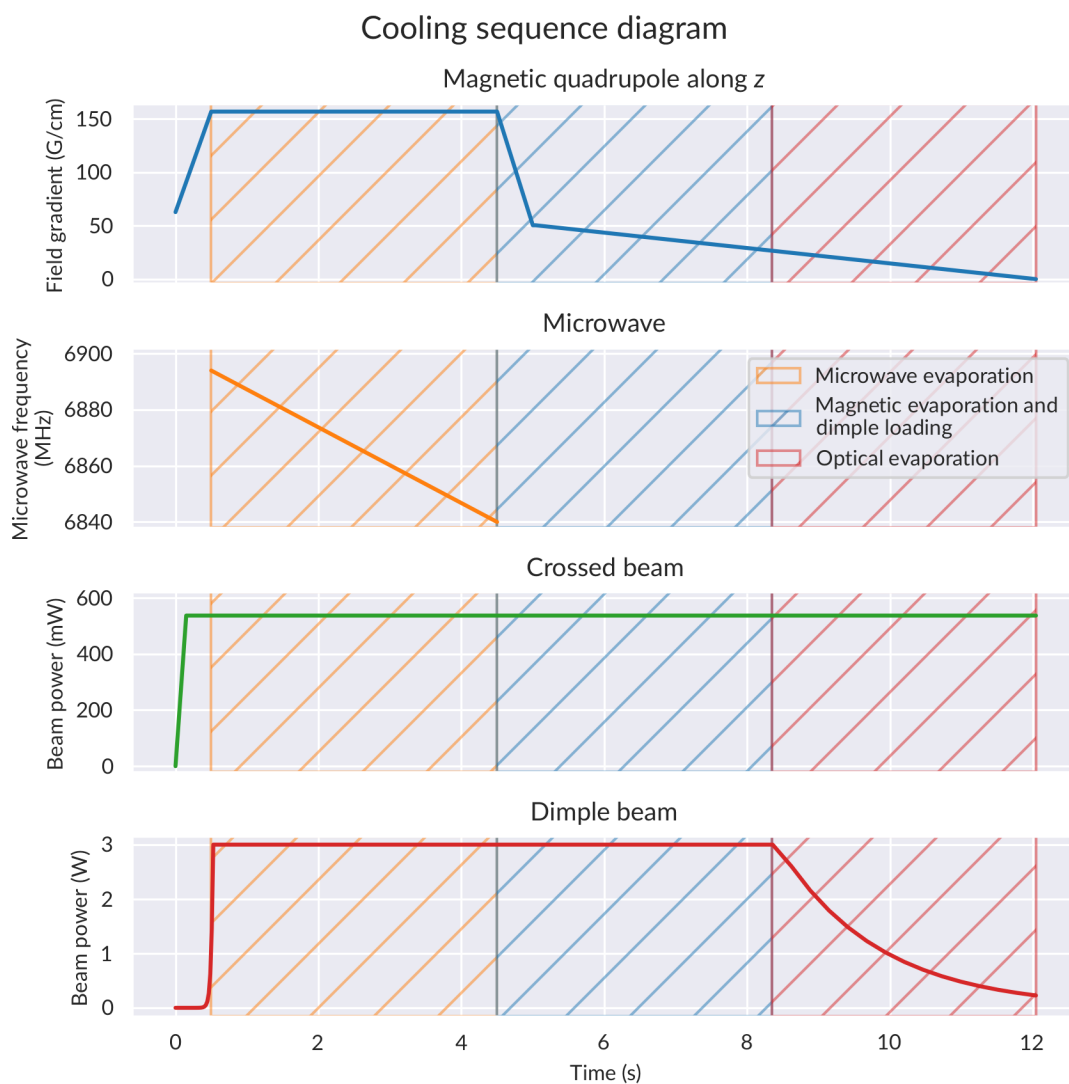


Figure 3.9.: Timing diagram of the cooling sequence, showing the main fields of interest (optical, magnetic, microwave) and the main phases (hatched areas).

here compares the fluorescence level of each MOT to a fixed threshold, and adjusts the loading rate of the MOTs by turning on or off the push beam according to the aforementioned method. The fluorescence is collected by one photodiode for each species, each equipped with an interferential filter to remove the fluorescence signal from the other species.

The atoms then undergo a brief (≈ 20 ms) Compressed MOT (CMOT) phase, which further cools both clouds [168]; as the optimal magnetic field gradient is different for K and Rb, the current in the quadrupole coils during this phase can also be used for a rough control of their number balance. After the CMOT, the Rb atoms are cooled to sub-Doppler temperatures with an optical molasses for 2 ms; while schemes for cooling ^{41}K exist both using its D2 [169]

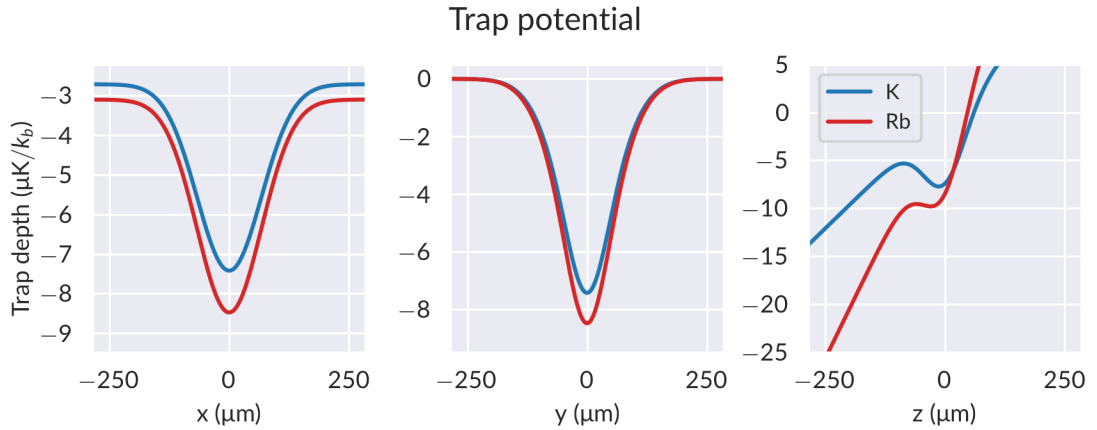


Figure 3.10.: Potential, as seen by the atoms, at the end of the evaporation. The potential is shown in the laboratory reference frame (i.e., the same reference frame as used by equations (3.8)–(3.16)).

and D1 [170] lines, we find that the benefits of having sub-Doppler K are smaller than the costs in terms of added experimental complexity. After this phase, the temperature for Rb is approximately $17 \mu\text{K}$ [171].

The atoms are then optically pumped in order to be in the $F = 2, m_F = 2$ Zeeman level of the ground state, as this is a magnetically trappable state. After that, the magnetic quadrupole trap is turned on to a field gradient of 157 G/cm ; typical numbers are of 3×10^7 K atoms and 4×10^9 Rb atoms [156]. In this magnetic trap, Rb is cooled with forced evaporative cooling, while K is sympathetically cooled by Rb. The evaporative cooling is done by sweeping a microwave from 6.894 GHz to 6.840 GHz (approximately, the transition energy is $k_B \times 1.78 \text{ mK}$ at the beginning, and $k_B \times 191 \mu\text{K}$ at the end of the microwave ramp) in 4 s . In the meanwhile, the optical dipole trap is turned on: the dimple beam is brought to approximately 3 W , and the crossed beam to 500 mW . After finishing the microwave ramp, the quadrupole is decompressed to 22.4 Tm^{-1} in 500 ms , and then ramped to zero current in 7 s .[§] This causes the atoms in the quadrupole to be slowly loaded in the crossed trap, whose centre is $76 \mu\text{m}$ below. After 2 s since the end of the quadrupole decompression, the dimple beam power is ramped from 3 W to 200 mW . This final passage cools the atoms to degeneracy. The potential as seen by the atoms is shown in figure 3.10. The trap frequencies for this configuration are (including gravity), for K $2\pi \times (52, 127, 130) \text{ Hz}$, and for Rb $2\pi \times (35, 85, 67) \text{ Hz}$; due to the different masses and atomic polarizabilities, there is a difference in the vertical plane for the two minima, called *gravitational sag*, which, at the end of the evaporation, is about $16 \mu\text{m}$; a procedure for compensating this effect in the $F = 1, m_F = 1$ state will be detailed in 3.4.

Using this sequence, we obtain a double condensate of K and Rb in the $F = 2, m_F = 2$ hyperfine state, of 4×10^4 – 1.6×10^5 and 1.6×10^5 – 3.0×10^5 atoms, respectively. The species imbalance can be controlled by changing the MOT stabilization cutoffs, or the value of the

[§]Just after the decompression, in order to avoid Majorana spin flip losses, a bias field of approximately 0.25 G along the z axis is added.

CMOT gradient; this capability is ultimately due to the anti-correlation of the number of atoms in the quadrupole between the two species. For a representative condensate with 2×10^5 Rb atoms and 7×10^4 K atoms, we obtain chemical potentials of $k_B \times 6 \times 10^{-9}$ K and $k_B \times 5 \times 10^{-9}$ K, and Thomas-Fermi radii of (20, 8, 6) μm and (10, 6, 6) μm for each species, respectively.

3.3. Hyperfine transfers

The double condensate produced at the end of the cooling sequence is in the $F = 2, m_F = 2$ hyperfine state, which is the highest in the ground state manifold. In order to be able to tune the interactions, we have to transfer the atoms in the $F = 1, m_F = 1$ state. Here, we have two accessible Feshbach resonances, one at $47.96 \text{ G} \pm 0.10 \text{ G}$, and one at $78.57 \text{ G} \pm 0.05 \text{ G}$ [129], which provide a convenient way of tuning the interspecies scattering length by staying at field intermediate between those two.

The transfer protocol used for both uses a rapid adiabatic passage to the target state, though with some minor differences between the protocols for the two atomic species, dictated by technical requirements. Rapid adiabatic passage occurs in a two level system when an electromagnetic field, to which the system is coupled, is slowly swept through the resonance. This ensures that the composite system of the radiation and the two level atom remains in the same dressed state, and thus go from the unperturbed ground state to the respective excited state (or vice versa, as in our case) [172]. This kind of transfer protocol is more robust with respect to the inevitable noise present in both the amplitude and frequencies of the electromagnetic field used for the transition, and in the two level energy separation. The probability of transition is [172]:

$$P_t = 1 - \exp\left(-\frac{\pi\Omega^2}{2\dot{\Delta}}\right), \quad (3.17)$$

where Ω is the Rabi frequency, $\dot{\Delta} = \frac{d}{dt}\Delta$, and $\Delta = \omega - \omega_0$ is the detuning of the angular frequency of the field ω from the transition frequency of the two level system ω_0 . In our case, the energy of the magnetic levels $m = m_I \pm 1/2$ of the hyperfine ground state of alkali atom in a magnetic field B is given by the Breit-Rabi formula [173]:

$$\begin{aligned} \Delta E(B, m) &= -\frac{\Delta E_{\text{hfs}}}{2(2I+1)} + g_I m \mu_B B \pm \frac{\Delta E_{\text{hfs}}}{2} \sqrt{1 + \frac{4m}{2I+1}x + x^2} \\ &= -\frac{\Delta E_{\text{hfs}}}{8} + g_I m \mu_B B \pm \frac{\Delta E_{\text{hfs}}}{2} \sqrt{1 + mx + x^2}, \end{aligned} \quad (3.18)$$

where

$$x = \frac{(g_J - g_I)\mu_B B}{\Delta E_{\text{hfs}}}, \quad (3.19)$$

ΔE_{hfs} is the hyperfine splitting of the unperturbed ground state, I is the nuclear quantum number, which for both species is $3/2$, and g_J and g_I are, respectively, the electronic and nuclear gyromagnetic factors. Relevant values for ^{41}K and ^{87}Rb are shown in table 3.1, and a graph of the transition levels is shown in figure 3.11.

Prior to the transfer, the Feshbach field is ramped from 0 G to 72.8 G in 40 ms. At this point, we first transfer K to the $F = 1, m_F = 1$ hyperfine ground state by sweeping a radio frequency

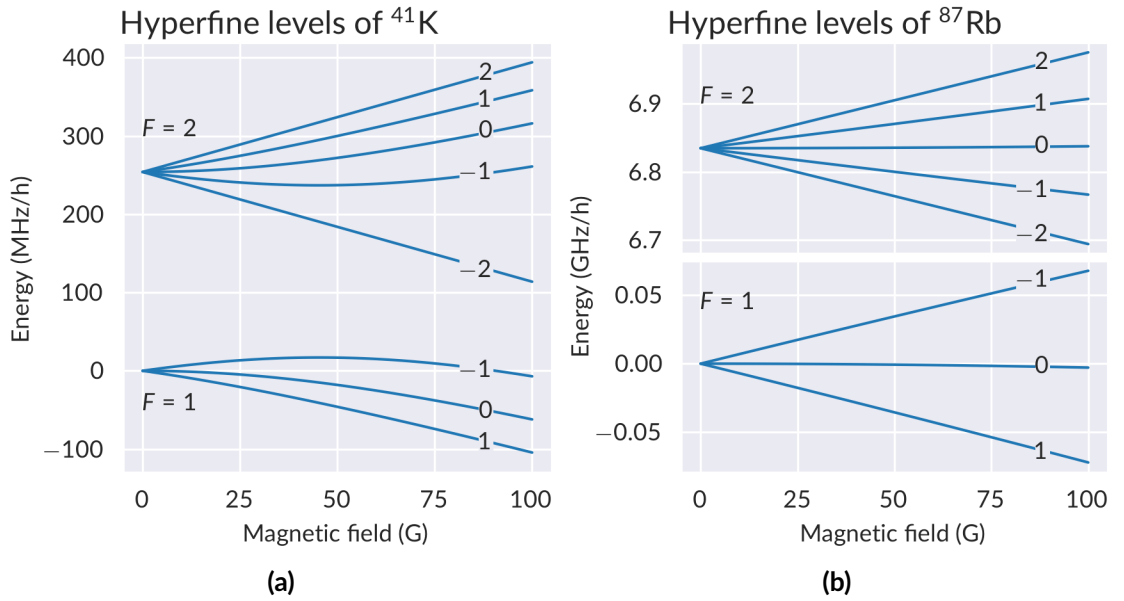


Figure 3.11.: Magnetic level energies as a function of the external field.

Table 3.1.: Nuclear gyromagnetic factors and dipole constants for ^{41}K [174] and ^{87}Rb [174, 175], which are needed to calculate the hyperfine energies with equation (3.18).

	g_I	$\Delta E_{\text{hfs}}/h(\text{Hz})$	
^{41}K	$-7.790600(8) \times 10^{-5}$	254.0138704(12)	$\times 10^6$
^{87}Rb	$-9.951414(10) \times 10^{-4}$	6.8346826109043(9)	$\times 10^9$

from 425.7 MHz to 427.3 MHz, with an efficiency ranging from 70% to more than 95%,[¶] and the fraction left in $F=2, m_F=2$ is pushed away with a pulse of resonant light. Then, we apply a microwave pulse of 5 ms at a fixed frequency of 6.987275 GHz, while ramping the Feshbach field from 72.81 G to 72.57 G, to transfer Rb to the $F=1, m_F=1$ hyperfine ground state; also for this transfer, the efficiency is above 96%.

The optimal central frequency and sweep length have been found by measuring the fraction of the atoms in each of the two states using a Stern-Gerlach-like protocol. The condensate is released from the trap, freely falling for 3 ms, after which the quadrupole field is turned on at 5.5 T m^{-1} for 13 ms; finally, the atoms have another 16 ms of free fall. This ensures a good separation of $F=2, m_F=2$ and $F=1, m_F=1$, due to their magnetic moments of opposite signs.

[¶]We typically cannot observe efficiencies above that, as the fraction of atoms in the starting state is not visible anymore

3.3.1. Feshbach field calibration

The b_0 coefficient from equation (3.16) has been determined by performing microwave spectroscopy on the Bose-Einstein condensate. This ensures that the atoms are in the same region of the magnetic field where they will be during subsequent experiments, which is important due to the inhomogeneity of the Feshbach field itself, and the gradient that is added for the compensation of the gravitational sag.

The calibration is done, with a Rubidium only BEC, in two steps. First, the Feshbach field is calibrated in isolation: this is done by producing a condensate, and then transferring it to the $F = 1, m_F = 1$ state with the Feshbach field kept at a fixed current I_f , by shining a 5 ms pulse of microwave light at a fixed frequency ω_μ ; the fraction in each state is then measured with the above described Stern-Gerlach protocol. By scanning ω_μ , we find a Gaussian transfer efficiency curve; an example of such a curve can be seen in Figure 3.12. We can then compare the Gaussian peak to the transfer frequency $|\Delta E(B^*(I_f), 1) - \Delta E(B^*(I_f), 2)|/\hbar$ in order to extract the value of the magnetic field at the atom position B . We fit the obtained data to a linear model, and we obtain, for the b_0 coefficient, a value of $2.353 \text{ G/A} \pm 0.014 \text{ G/A}$, with the error taken as the standard error of the parameter. The constant part of the linear model is $-0.37 \text{ G} \pm 0.40 \text{ G}$, which does not reject the null hypothesis that the magnetic field at zero current is zero (p -value ≈ 0.4): in other words, while this method is quite adequate for the calibration of the coils in object, it is not currently possible to get information on spurious magnetic fields. The fitted calibration line is reported in figure 3.13a.

The second step of the calibration is adding the effects of the quadrupole field on the Feshbach field. Differently from the Feshbach only calibration, here the BEC is first transferred to the $F = 1, m_F = 1$ state following the standard Landau-Zener procedure described above. Then, the Feshbach current is brought to a fixed value $I_f = 30.5 \text{ A}$, and the gradient current is put to a value I_q . From here, the procedure is identical to the previous calibration, with the only difference that the transfer is done in reverse; this is done to ensure that the atoms are in the exact same position where they would be during the experiment, which is important due to the intrinsic inhomogeneity of the quadrupole field. We then fit the difference between the expected field and the actual field with a linear model

$$B = B_f + \alpha I_q \quad (3.20)$$

and find the effect of the quadrupole on the Feshbach field. We find for the parameter α a value of $9.48 \times 10^{-3} \text{ G/A} \pm 0.12 \times 10^{-3} \text{ G/A}$. For B_f , we obtain a value of $71.365 \text{ G} \pm 0.002 \text{ G}$; in figure 3.13b we report a summary of this calibration. We can compare this with the prediction of the previous model at the same current, which is $71.40 \text{ G} \pm 0.02 \text{ G}$; a z-test performed with this data results in a p value of 0.17, and thus we can say that the two models are not incompatible.

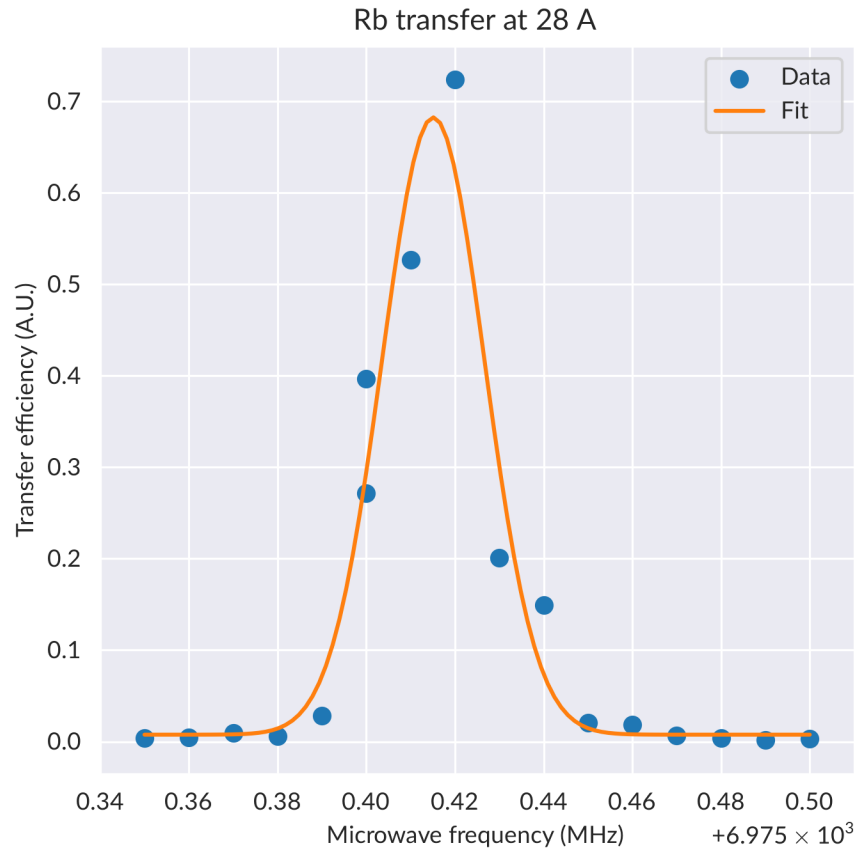


Figure 3.12.: Transfer efficiency curve for Feshbach field calibration acquired at a current of 28 A. The dots represent the average of the individual transfers at the particular frequency, and the continuous line represents a fit with a Gaussian function. The peak frequency is 6975.415 MHz, with a full width at half maximum (FWHM) of 2.7 kHz; for both parameters, the fit uncertainty is of the order of 1 kHz.

3.4. Gravity compensation

As mentioned, the two condensates do not overlap at the end of the evaporation. In the simplest case of an harmonic optical potential plus a gravity term,

$$U_i = \frac{m_i \omega_i^2}{2} z_i^2 + m_i g z_i, \quad (3.21)$$

the gravitational sagging is due to the difference in frequencies

$$\Delta z = \left| \frac{\omega_{\text{Rb}}^2 - \omega_{\text{K}}^2}{g} \right|, \quad (3.22)$$

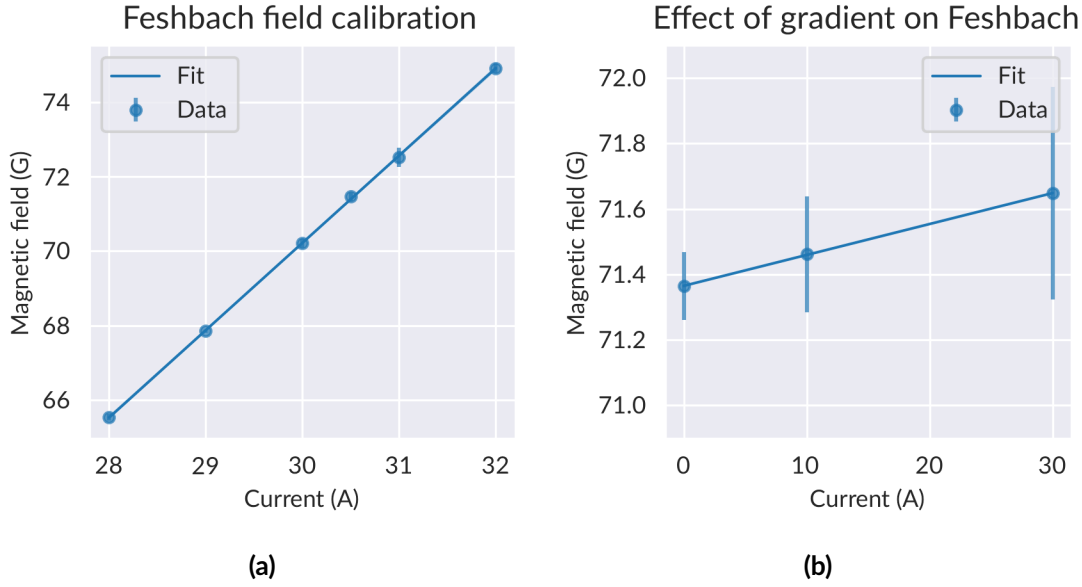


Figure 3.13.: Calibration lines for the Feshbach field alone (a) and for the quadrupole at a fixed Feshbach current of 30.5 A (b). Each data point is the weighted mean of the field extracted from the central peaks for the Gaussian fits, and the error bars are the corresponding standard errors.

which is ultimately due to the difference in polarizability and mass between ^{41}K and ^{87}Rb . This can be countered by adding another potential term which induces an equal and opposite shift, and which, in our case, is the quadrupole field: that is because the two species have, within the region in which we vary our Feshbach field, different magnetic moments μ . With a magnetic term $\mu_i B_q z_i$ added, (3.22) becomes, to first order in z ,

$$\Delta z = \left| \frac{m_{\text{Rb}} \omega_{\text{Rb}}^2}{m_{\text{Rb}} g + \mu_{\text{Rb}} B_q} - \frac{m_{\text{K}} \omega_{\text{K}}^2}{m_{\text{K}} g + \mu_{\text{K}} B_q} \right|. \quad (3.23)$$

The magnetic moment for each species is

$$\mu = -\frac{\partial E}{\partial B} \quad (3.24)$$

$$= g_I \mu_B + \frac{\Delta E_{\text{hfs}} (x' + x'^2 B)}{2\sqrt{x^2 + x + 1}} \quad (3.25)$$

E is given, up to an additive constant, by (3.18), $x = (g_J - g_I) \mu_B B / \Delta E_{\text{hfs}}$ is the same as in (3.19), and $x' = \partial_B x$. A graph of μ as a function of B is reported in figure 3.14. While, a priori, the B for (3.24) would include all fields, in all practical cases the quadrupole correction to the Feshbach field (3.20) is negligible: to make an example, the maximum difference between neglecting and including the quadrupole correction in the values calculated for figure 3.14 is $3 \times 10^{-6} \mu_B$ for Rb, and $8 \times 10^{-5} \mu_B$ for K.

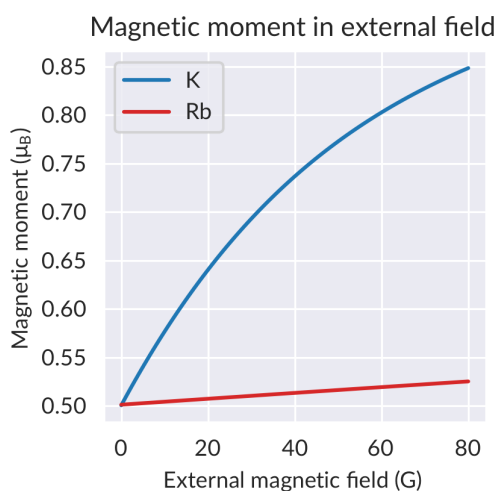


Figure 3.14.: Magnetic moment, in Bohr magnetons, of ^{41}K and ^{87}Rb in the $F = 1, m_F = 1$ state in an external magnetic field, as calculated with (3.24). The red line represents Rb, which is constant to 4% in the selected range, whereas the blue line is ^{41}K . A typical experiment is performed within the 60 G–80 G range.

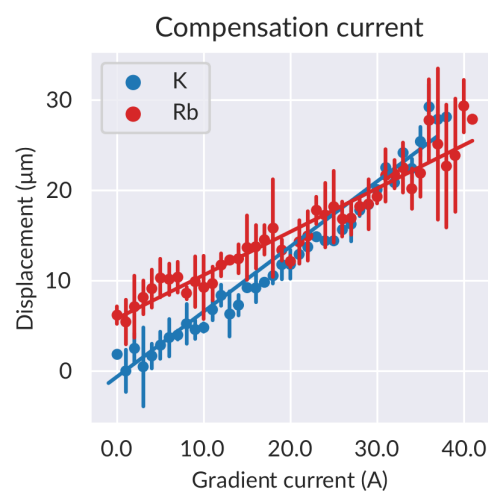


Figure 3.15.: Position of the centre of mass of the condensates as a function of the current. The dots represent the weighted means of the positions for the corresponding fields, and the error bars their corresponding standard error. The two continuous lines represent the linear fits of the position; the point at which they overlap is the calibration result.

The overlapping sequence is done as follows: first, the trap is recompressed, ramping the dimple power to 300 mW and the crossed power to 800 mW in 250 ms, raising ω_z to $2\pi \times 170\text{Hz}$ for K and $2\pi \times 115\text{Hz}$. This is done because otherwise the trap depth would be insufficient to hold the condensates once the quadrupole field is added, as it pushes the condensates in the same direction as gravity.^{||} Then, the field is raised to the compensation value, linearly, in 150 ms. This is done to ensure that atoms in the spurious $F = 2, m_F = 2$ state are separated from the condensates before they reach their final densities.

The compensation value, due to dependence of the trap frequencies themselves on the magnetic field in (3.23), is calculated numerically, and we find a value of 16.5 G/cm; this corresponds to a coil current of 29.5 A. Within this approximation, the residual sagging is less than $1 \times 10^{-2} \mu\text{m}$.

The compensation field value obtained above can be easily checked. For this purpose, we measure the vertical position of the condensate in situ. We first prepare a Rb condensate in the lowest hyperfine state with the same sequence as above, but this time the crossed is compressed to about 1.2 W. At the end of the process, the dimple beam is ramped to 0 W in 10 ms, and, after 12.5 ms, the condensate is imaged (see Section 5.4 for more details on the imaging of condensates with non-zero magnetic fields). The same is then done with a K only

^{||}The zero of the total magnetic field is above the optical trap centre, and $F = 1, m_F = 1$ is an high-field seeking state.

condensate, which is obtained by blasting away Rb atoms before the transfer with a 1 ms pulse of resonant light. By varying the quadrupole field, we can see the translation of the centre of mass of each cloud. Fitting each with a linear function $z_i = z_{i0} + \beta_i I_q$, we find the coil current for which the two species are overlapped:

$$I_q^* = \frac{z_{\text{Rb}0} - z_{\text{K}0}}{\beta_{\text{K}} - \beta_{\text{Rb}}}. \quad (3.26)$$

The fitted coefficients are $z_{\text{Rb}0} = -23.7 \mu\text{m} \pm 0.4 \mu\text{m}$, $\beta_{\text{Rb}} = -0.42 \mu\text{mA}^{-1} \pm 0.02 \mu\text{mA}^{-1}$, $z_{\text{K}0} = -13.9 \mu\text{m} \pm 0.9 \mu\text{m}$, and $\beta_{\text{K}} = 0.83 \mu\text{mA}^{-1} \pm 0.03 \mu\text{mA}^{-1}$; this gives a compensation current of $24 \text{A} \pm 6 \text{A}$; a z-test with the prediction has a p value of 0.64, and thus the two values are not incompatible. A graph of the data with the fits can be seen in figure 3.15.

Dipole oscillations of an interacting bosonic mixture

In this chapter, we will look at the physics of dipole oscillations in our mixture. While for a single trapped gas dipole oscillations are employed to measure the trap frequencies—role for which they are particularly suited due to the fact that the frequencies thus obtained are independent of the interactions [176]—for a mixture interspecies coupling changes the picture. There has been considerable interest in collective excitations in general for this kind of systems, whether they are spin mixtures [41, 177–180], immiscible condensates [26], or strongly imbalanced condensates [88]; dipole oscillations in mixtures have also been employed as a tool for measuring interspecies interactions [35, 181], and to better understand the nature of multi-component superfluidity [34, 182]. Here, we will look at dipole oscillations for various regimes of interspecies interactions, expanding on the results presented on the publication upon which this chapter is based [92].

In Section 4.1, we will look at the theoretical aspects of dipole oscillations; then we will see, in Section 4.2, how the experimental protocols worked, both from the side of exciting the dipole oscillation, and of analyzing the collected data. The results thus obtained will be discussed in Section 4.3 for what concerns the frequencies and amplitudes of the oscillations, in Section 4.4 to expound on the role of population imbalance, and finally in Section 4.5 for some considerations on the damping of the oscillation amplitude.

4.1. Theoretical framework

In this section we will talk about the theoretical framework for dipole oscillations. We will start with the theory for collective excitations for the case of a single condensate in Subsection 4.1.1, where we look at the shape of a condensate during a dipole oscillation using both a first-principle approach from the hydrodynamic equations and an ansatz solution for the GPE. In Subsection 4.1.2, we will look at two semi-classical models for dipole oscillations, namely the

sum rules model for collective excitations, applied to our specific case, and a model based on Ehrenfest's theorem.

4.1.1. Classification of the collective excitations

Collective oscillations are usually classified in terms of multipole expansion terms: monopole, dipole, quadrupole, and so on and so forth. This can be derived from the hydrodynamic theory for a single Bose-Einstein Condensate. The hydrodynamic equations can be derived from the Gross-Pitaevskii Equation (2.71), assuming for the wave function the form

$$\Psi(\mathbf{r}, t) = \sqrt{n(\mathbf{r}, t)} e^{iS(\mathbf{r}, t)}; \quad (4.1)$$

they are [94]:

$$\frac{\partial}{\partial t} n + \nabla \cdot (\mathbf{v} n) = 0 \quad (4.2)$$

and

$$m \frac{\partial}{\partial t} \mathbf{v} + \nabla \left(\frac{1}{2} m \mathbf{v}^2 + V_e + g n \right) = 0, \quad (4.3)$$

where the superfluid velocity is

$$\mathbf{v}(\mathbf{r}, t) = \frac{\hbar}{m} \nabla S(\mathbf{r}, t), \quad (4.4)$$

and V_e is an external potential.

We will look at the case of an harmonic potential (2.69) in the spherical case $\omega_x = \omega_y = \omega_z = \omega$. Making a small perturbation ansatz for the solutions of (4.2)-(4.3), $\delta n(\mathbf{r}, t) e^{-i\omega t} = n(\mathbf{r}, t) - n_0(\mathbf{r})$, where n_0 is a stationary solution, we obtain the linearized equation, valid in the Thomas-Fermi limit [138]:

$$\omega^2 \delta n = -\frac{1}{2} \omega_0^2 \nabla (R^2 - r^2) \nabla \delta n, \quad (4.5)$$

where R is the Thomas-Fermi radius; the equation is valid for $-R < r < R$. Solutions for this equation have the form [138]

$$\delta n = \delta n_0 P_l^{2j} \left(\frac{r}{R} \right) Y_{lm}(\theta, \phi), \quad (4.6)$$

where $P_l^{2j}(x) = 1 + a_2 x^2 + \dots + a_{2j} x^{2j}$, and $Y_{lm}(\theta, \phi)$ are the spherical harmonics, and j is the radial number of nodes.

For the specific case of dipole oscillations ($l = 1, j = 0$), we can write explicitly

$$\delta n_d(\mathbf{r}, t) = \delta n_0 \frac{r}{R} \frac{1}{2} \sqrt{\frac{3}{\pi}} \times \begin{cases} \cos \theta & \text{for } m = 0 \\ \mp e^{\pm i\phi} \sin \theta & \text{for } m = \pm 1 \end{cases} \quad (4.7)$$

and, so,

$$n(x, y, z, t) = n_0 + \Re(\delta n(\mathbf{r}, t))$$

$$= n_0 + \delta n_0 \frac{1}{2} \sqrt{\frac{3}{\pi}} \frac{z}{R} \cos(\omega t), \quad (4.8)$$

assuming that the oscillation is along z .

Given that (4.5) is derived in the Thomas-Fermi limit, we can assume for n_0 a Thomas-Fermi density shape, so

$$n(\mathbf{r}, t) = n_0 \left(1 - \frac{r^2}{R^2} \right) + \delta n_0 \frac{1}{2} \sqrt{\frac{\pi}{3}} \frac{z}{R} \cos(\omega t) \quad (4.9)$$

$$= n_0 \left(1 - \frac{x^2 + y^2}{R^2} - \frac{z^2}{R^2} + \frac{z}{R} \frac{\delta n_0}{n_0} \frac{1}{2} \sqrt{\frac{\pi}{3}} \cos(\omega t) \right) \quad (4.10)$$

and we find that the peak of the density distribution moves along z as

$$z_0 = R \frac{\delta n_0}{n_0} \sqrt{\frac{3}{\pi}} \cos(\omega_z t). \quad (4.11)$$

There is another way of obtaining the wave function for dipole oscillations [94]. If we assume the functional form

$$\Psi(\mathbf{r}, t) = e^{-i(\phi(t) - z\beta(t))/\hbar} \Psi_0(x, y, z - \alpha(t)), \quad (4.12)$$

for the Gross-Pitaevskii equation (2.71), where Ψ_0 is a solution of (2.73). We find that

$$\beta = m\dot{\alpha} \quad (4.13)$$

$$\dot{\beta} = -m\omega_z^2 \alpha, \quad (4.14)$$

which is solved, up to a constant phase factor, by

$$\alpha(t) = A \cos(\omega_z t) \quad (4.15)$$

$$\beta(t) = A \omega_z \sin(\omega_z t), \quad (4.16)$$

giving

$$\Psi = e^{-i(\phi(t) - z\omega_z A \cos(\omega_z t))/\hbar} \Psi_0(x, y, z - A \cos(\omega_z t)), \quad (4.17)$$

and thus

$$n(x, y, z, t) = |\Psi_0(x, y, z - A \cos(\omega_z t))|^2; \quad (4.18)$$

we can fix A by looking at (4.11).

If we compare (4.8) and (4.18), we see that, in both cases, the distributions undergo a rigid translation along the oscillation axis. The actual wave function will be different in the two cases, because in (4.8) the Thomas-Fermi approximation is used, whereas in (4.18) it is not, nevertheless this difference is simply the difference in ground state wave function between the full Gross-Pitaevskii Equation and its approximated form. It is also worth noting that the oscillation frequency is determined only by the trap frequency, in analogy to what Kohn's theorem predicts for the cyclotron frequency of an electron gas [176]; a consequence of Kohn's theorem is that a thermal gas, or the thermal fraction of a partially condensed sample, would also oscillate at the same frequency as a BEC.

4.1.2. Coupled models of dipole oscillations

While the equations (4.2) and (4.3) are useful for treating dipole oscillations of single component BECs with repulsive interactions, for our purposes they are not sufficient, as we have a double species BEC, and we would like to investigate both the attractive and the repulsive regimes. That is because, as we will see later, the presence of the interactions changes the character of the dipole oscillations, introducing a dependence of the frequencies and amplitudes of said oscillations on the strength and sign of the interspecies interaction.

A widely used approach for this kind of calculations is based on sum rules [138, 183]. This approach is based on linear response theory [184]: for a scalar potential $\phi(\mathbf{q}, \omega)$ with an interaction Hamiltonian

$$H_i = F_{\mathbf{q}}^\dagger \phi(\mathbf{q}, \omega) e^{-i\omega t} + F_{\mathbf{q}} \phi(\mathbf{q}, \omega) e^{i\omega t}, \quad (4.19)$$

the response of the observable connected to F is

$$\langle F(\mathbf{q}, \omega) \rangle = \langle \Psi(\mathbf{r}, t) | F_{\mathbf{q}} e^{i(\omega - \eta)t} | \Psi(\mathbf{r}, t) \rangle \quad (4.20)$$

where Ψ is a state of the perturbed Hamiltonian, is proportional to the perturbation via the susceptibility $\chi(\mathbf{q}, \omega)$:

$$\langle F(\mathbf{q}) \rangle = \chi(\mathbf{q}, \omega) \phi(\mathbf{q}, \omega), \quad (4.21)$$

which has the form

$$\chi(\mathbf{q}, \omega) = \sum_n \left| \langle 0 | F_{\mathbf{q}}^\dagger | n \rangle \right|^2 \frac{2\omega_{n0}}{(\omega + i\eta)^2 - \omega_{n0}^2}. \quad (4.22)$$

The real component of the exponential in (4.20) is added to ensure causality [184]; the final values are to be taken after going to the limit $\eta \rightarrow 0$ at the end of the calculation. The density response function can be expressed in term of its spectral density

$$\chi(\mathbf{q}, \omega) = \int_0^{+\infty} S(\mathbf{q}, \omega') \left(-\frac{1}{\omega - \omega' + i\eta} - \frac{1}{\omega + \omega' + i\eta} \right) d\omega', \quad (4.23)$$

which is called the *dynamic structure factor*. In the usual case of a discrete spectrum, the dynamic structure factor is

$$S(\mathbf{q}, \omega) = \sum_n \langle n | F_{\mathbf{q}}^\dagger | 0 \rangle \delta(\omega - \omega_{n0}). \quad (4.24)$$

The sum rules approach hinges on the calculation of the moments of the dynamic structure factor [185]:

$$m_n = \int_{-\infty}^{+\infty} \omega^n S(\mathbf{q}, \omega) d\omega \quad (4.25)$$

$$= \sum_l (\omega_{l0})^n \langle l | F_{\mathbf{q}}^\dagger | 0 \rangle; \quad (4.26)$$

for these moments we have the relations

$$\dots \geq \frac{m_{k+2}}{m_{k+1}} \geq \sqrt{\frac{m_{k+2}}{m_k}} \geq \frac{m_{k+1}}{m_k} \geq \dots, \quad (4.27)$$

where the equal sign holds when the sum (4.24) for the calculation of S has only one term, that is, if only one collective mode is excited. These ratios can be used to define average frequencies:

$$\omega_{1,k} = \frac{m_{k+1}}{m_k} \quad (4.28)$$

$$\omega_{2,k} = \sqrt{\frac{m_{k+2}}{m_k}}. \quad (4.29)$$

For the first few moments, we have simple closed forms in terms of commutators $[\cdot, \cdot]$ and anticommutators $\{\cdot, \cdot\}$ [186]:

$$m_0 = \frac{1}{2} \langle 0 | \{F, F\} | 0 \rangle - \langle 0 | F | 0 \rangle^2 \quad (4.30)$$

$$m_1 = \frac{1}{2} \langle 0 | [F, [H, F]] | 0 \rangle \quad (4.31)$$

$$m_2 = \frac{1}{2} \langle 0 | \{[F, H], [H, F]\} | 0 \rangle \quad (4.32)$$

$$m_3 = \frac{1}{2} \langle 0 | [[F, H], [H, [H, F]]] | 0 \rangle, \quad (4.33)$$

and thus we can express the collective excitation frequency as

$$\omega^2 = \frac{m_3}{m_1}. \quad (4.34)$$

In our case, the observable of interest is the position of the two centres of mass, given by the dipole operator D [187]:

$$D = \alpha_1 \sum_{i=1}^{N_1} x_{1i} + \alpha_2 \sum_{i=1}^{N_2} x_{2i} \quad (4.35)$$

where 1,2 indicate the species, $\alpha_1^2 + \alpha_2^2 = 1$ are mixing parameters, and the Hamiltonian is that of the coupled GPE (2.82). Calculating (4.34), the oscillation frequency is [183]:

$$\omega^2 = \frac{\frac{N_1}{m_1} \alpha_1^2 \omega_1^2 + \frac{N_2}{m_2} \alpha_2^2 \omega_2^2 - g_{12} I \left(\frac{\alpha_1}{m_1} - \frac{\alpha_2}{m_2} \right)^2}{\frac{N_1}{m_1} \alpha_1^2 + \frac{N_2}{m_2} \alpha_2^2}, \quad (4.36)$$

where

$$I = \int \frac{\partial n_{01}}{\partial x} \frac{\partial n_{02}}{\partial x} \mathbf{dr}, \quad (4.37)$$

and n_{0i} is the ground state density of the i -th condensate. The frequencies of the two eigenmodes are obtained then by setting

$$\alpha_1 = \frac{\cos\theta + \sin\theta}{\sqrt{2}} \quad (4.38)$$

$$\alpha_2 = \frac{\cos\theta - \sin\theta}{\sqrt{2}} \quad (4.39)$$

and calculating the mixing angle θ for which the frequency is stationary:

$$\frac{\partial\omega^2(\theta)}{\partial\theta} = 0. \quad (4.40)$$

This equation gives two mixing angles, θ_{\pm} , which correspond to two solutions ω_{\pm} .

While the sum rule theory has its advantage in generality, there is another, more immediately physical approach, based on the Ehrenfest's theorem [183]. The theorem states that [188]:

$$m \frac{d^2}{dt^2} \langle \mathbf{r} \rangle = - \langle \nabla V \rangle, \quad (4.41)$$

where, for a Bose-Einstein condensate, V is the potential in the GPE (or in the coupled GPE for a mixture). If we define $\xi_i = \langle \mathbf{x}_i \rangle$, we obtain

$$\ddot{\xi}_i(t) = -\omega_i^2 \xi_i(t) - \sum_j \frac{g_{ij}}{m_i N_i} \int n_i \frac{\partial}{\partial x} n_j d\mathbf{r}. \quad (4.42)$$

Because we are interested in dipole oscillations, we can use (4.8) and a small oscillation approximation to calculate the integral in the previous equation:

$$n \approx n_0 - \frac{\partial n_0}{\partial x} \xi, \quad (4.43)$$

so that

$$\ddot{\xi}_i(t) = -\omega_i^2 \xi_i - \eta_i \sum_j \xi_j, \quad (4.44)$$

where

$$\eta_i = \frac{g_{12} I}{m_i N_i}. \quad (4.45)$$

This is a matrix equation:

$$\begin{pmatrix} \ddot{\xi}_1 \\ \ddot{\xi}_2 \end{pmatrix} = \begin{pmatrix} \omega_1^2 - \eta_1 & \eta_1 \\ \eta_2 & \omega_2^2 - \eta_2 \end{pmatrix} \begin{pmatrix} \xi_1 \\ \xi_2 \end{pmatrix} = \mathbf{M} \begin{pmatrix} \xi_1 \\ \xi_2 \end{pmatrix}, \quad (4.46)$$

the eigenvalues ω_{\pm} of the dynamic matrix \mathbf{M} are the frequencies of the eigenmodes of the oscillations; it has been shown [183] that this method is equivalent, for dipole oscillations, to the sum rule method. If we define $\Omega_i^2 = \omega_i^2 - \eta_i$, we obtain the eigenvalues

$$\omega_{\pm}^2 = \frac{\Omega_1^2 + \Omega_2^2}{2} \pm \sqrt{\left(\frac{\Omega_1^2 + \Omega_2^2}{2}\right)^2 + \omega_1^2 \eta_2 + \eta_1 \omega_2^2 - \omega_1^2 \omega_2^2} \quad (4.47)$$

and the eigenvectors

$$\mathbf{v}_{\pm} = \frac{1}{\sqrt{\left(\frac{\Omega_2^2 + \omega_{\pm}^2}{\omega_2^2}\right)^2 + 1}} \begin{pmatrix} \frac{\Omega_2^2 + \omega_{\pm}^2}{\omega_2^2} \\ 1 \end{pmatrix}. \quad (4.48)$$

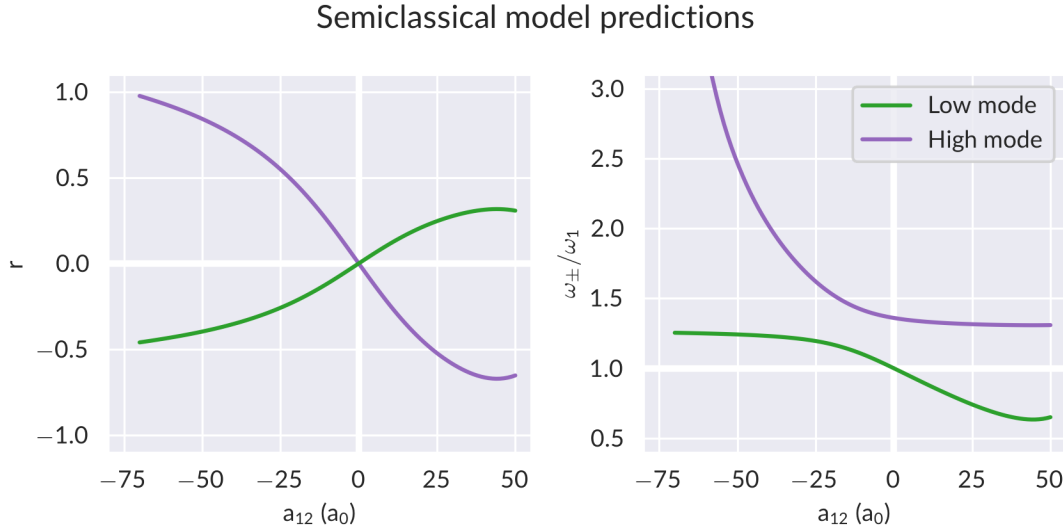


Figure 4.1.: Relative intensity (left) and normalized frequency (right) predicted by the semiclassical approaches (respectively, (4.49) and (4.47)). The quantities for the non-interacting case ($r = 1$, $\omega_{\pm} = 1$) are highlighted.

From (4.47), we can see that the oscillation decomposes in two proper modes, a low frequency mode oscillating at a frequency ω_- , and an high-frequency mode oscillating at a frequency ω_+ , and that, as said above, the oscillation frequency depends on the interspecies interaction via the η_i parameters. We also remark that, in the attractive regime, the low frequency mode corresponds to the in-phase motion of the condensates, while the high-frequency mode corresponds to the out-of-phase motion; in the repulsive regime, the roles are reversed.

The amplitude of the oscillation modes can then be obtained from the eigenvectors by transforming back the motion in the proper coordinates to that in the centre-of-mass coordinates. It is useful to construct two ratios, $r_+ = v_{+1}/v_{+2}$ and $r_- = v_{-2}/v_{-1}$, which represent the ratio between the two modes in the centre-of mass coordinates; they are equal to [183]:

$$(r_{\pm})^{\pm 1} = \frac{1}{2} \left[(1 - \beta) + \frac{\omega_1^2 - \omega_2^2}{2\eta_2} \right] \pm \sqrt{\frac{(1 + \beta)^2}{4} + (1 - \beta) \frac{\omega_1^2 - \omega_2^2}{2\eta_2} + \left(\frac{\omega_1^2 - \omega_2^2}{2\eta_2} \right)^2}. \quad (4.49)$$

An important feature of the models seen so far is that they depend on the assumption that the motion amplitude is small and the translation purely rigid.* As we will see later, these assumptions are not always valid, and, ultimately, the most accurate predictions come from numerical simulations of the full coupled GPE. Nevertheless, these theoretical approaches are useful for understanding the main physical features of dipole oscillations: namely, the dependence of the frequencies and amplitudes on the interspecies interaction parameter g_{12} .

*From sum rule theory, we know that the frequencies found would, in this case, just be an upper bound of the actual motion frequency.

4.2. Experimental protocol

The experimental procedure in our study of the dipole oscillations starts after the last stage of preparation described in Chapter 3, namely with the two non interacting overlapped condensates in a crossed dipole trap. After tuning the interspecies interaction to the target value, a dipole oscillation along the vertical axis can then be excited by suddenly changing the gradient from the gravity compensation value to some other value; in this way, the centres of the two traps are shifted, while the condensates, due to their finite mass, remain approximately in place. For the purposes of what is exposed in this chapter, the quadrupole field is suddenly shifted from the compensation value of 16.5 G/cm to 14.5 G/cm, causing a displacement of $\approx 1 \mu\text{m}$ for Rb and $\approx 2 \mu\text{m}$ for K [92].[†] Given the bare trap frequencies ω_z of $2\pi \times 185 \text{ Hz}$ for K and $2\pi \times 135 \text{ Hz}$ for Rb, we have a worst case scenario $t_s \omega_z / (2\pi)$ of 0.19, which we find sufficient to avoid that the condensates adiabatically follow the displacement of the trap minima.

After the excitation of dipole motion, the condensates are held in the trap for a variable amount of time t_t , then released from the trap, undergoing a ballistic fall for a time t_{TOF} , and finally imaged with absorption imaging. We varied t_t from 0 ms to 20 ms, with a sampling time of 1 ms for non-interacting oscillations, and 0.5 ms for interacting oscillations; each oscillation is repeated five times to achieve a better signal-to-noise ratio. The interspecies interactions are varied between $6.6 a_0 \pm 1.2 a_0$ and $-84.0 a_0 \pm 1.2 a_0$. A graph for a typical oscillation, namely one where $a_{12} = -19.5 \pm 1.2 a_0$, is reported in Figure 4.2.

We explored mainly the attractive side due to the fact that for interspecies repulsion, even in the miscible regime, and even for the small differential shifts used, the condensates tend to go out of the linear regime. This results in a rapid heating of the samples, and the loss of the condensate before a sufficient part of the oscillation can be sampled.

The time of flight has the effect of amplifying the oscillation amplitude: the displacement of the centre of mass from the neutral position is, up to a constant phase:

$$\Delta z(t_t, t_{\text{TOF}}) = z(t_t, t_{\text{TOF}}) - \frac{at_{\text{TOF}}^2}{2} \quad (4.50)$$

$$= x_0(t_t) + v_0(t_t) t_{\text{TOF}} \quad (4.51)$$

$$= A \sin(\omega t_t) + A \omega t_{\text{TOF}} \cos(\omega t_t) \quad (4.52)$$

$$= A \sqrt{1 + (\omega t_{\text{TOF}})^2} \sin\left(\omega t_t + \arctan\left(\frac{1}{\omega t_{\text{TOF}}}\right)\right) \quad (4.53)$$

In our procedure, we have a time of flight for K of 35 ms and for Rb of 38 ms, giving, for the bare trap frequencies, an amplification factor of, respectively, 41 and 32.

As the eigenmode frequencies and amplitudes vary with the number of atoms (see (4.36)), we keep $N_K \approx 7 \times 10^4$ and the population imbalance $\alpha = N_{\text{Rb}}/N_K$ within the range 1.5–4.0; this is done by regulating the MOT fluorescence with the methods exposed in Section 3.2, and subsequently discarding shots outside of the specified α range.

[†]The settling time t_s of the current in the quadrupole coils is of about 1 ms; we define settling time as the time between the rising edge of the input, supposed of negligible width, and the earliest instant after which the difference between the instantaneous value of the signal and its mean steady-state value is within $\pm 2\%$ of the signal excursion [189].

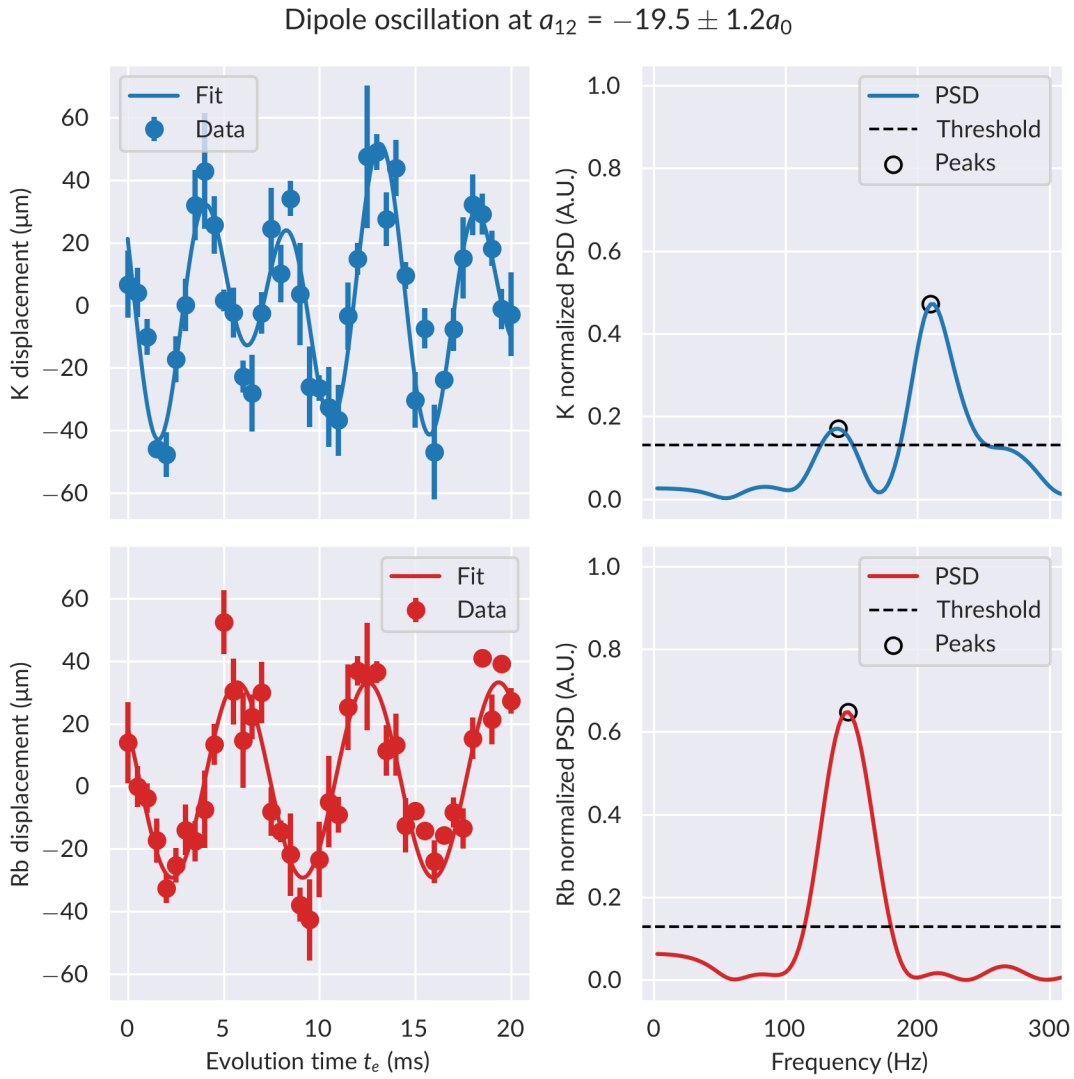


Figure 4.2.: Dipole oscillation of the mixture with an interspecies scattering length of $-19.5 a_0 \pm 1.2 a_0$. On the first row, we can see the data for K, and on the second for Rb. The left column shows the average of the centre of mass for each evolution time, along with an error bar representing its standard deviation of the mean; the continuous line is the prediction of the fitted model. On the right column, we see the spectrum of the data, calculated with the methods described in this section. The dashed line represents the threshold for a false alarm probability below 5%, and the circlets the location of the detected peaks.

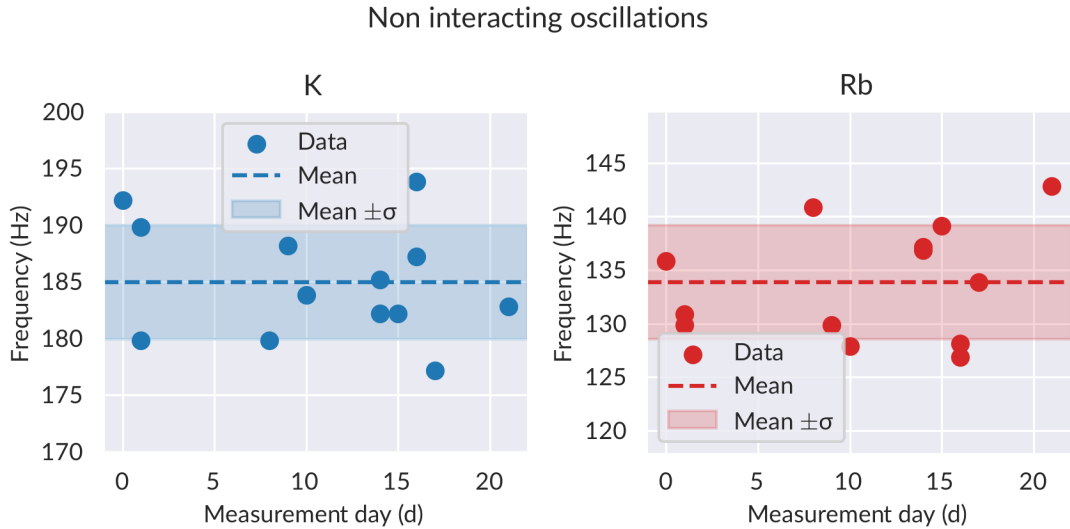


Figure 4.3.: Frequency of non interacting oscillations for K (left panel) and Rb (right panel) for the various days of measurement. A new non-interacting oscillation is taken whenever the optical dipole trap is realigned. A dashed line is put at the average of all the obtained oscillation frequencies, and a band spans a range of plus or minus one standard deviation of the oscillation frequencies centred on the aforementioned average frequency.

As we will see in Section 4.3, the oscillation frequencies and amplitudes are normalized to the respective values for the non-interacting case. In order to counteract drifting effects due to the finite precision of the beam alignment and of the trap laser power stabilization, a non-interacting oscillation is taken each day of measurement and each subsequent time during the day in which the optical dipole trap is realigned. A graph of the non interacting oscillation frequencies, analyzed with the methods discussed below, is visible in Figure 4.3. The mean value for the non interacting frequencies over all the measurements is for Rb 135 Hz, and for K 187 Hz, with a standard deviation of the frequency for both of 5 Hz.[‡]

For each oscillation, the analysis is done in two steps. The first step is a preliminary assessment of the harmonic content of the centre of mass motion: this is done with a Lomb-Scargle periodogram analysis [191, 192]. This kind of spectral estimation technique is particularly suited to our situation as it relaxes two assumptions which are fundamental to other popular methods, such as the simple periodogram [193] or Welch’s method [194], which is that the samples are equally spaced and with negligible uncertainty.[§] The Lomb-Scargle

[‡]The usual, and more correct, way of assessing the stability of an oscillator is using the Allan variance [190]; in our case, the way in which the oscillation frequency is estimated is not amenable to evaluation with this kind of metric, which assumes an oscillator sampled at regular intervals. The irregularity of our sampling times (i.e. the time between two non-interaction oscillations) means that we rarely have three points with the same delay between them, which is the minimum for evaluation of the Allan variance.

[§]Removing the uniform sampling constraint is useful if, for example, there are no acquired points for a certain specific t_e , but this did not happen for the data acquired in the work presented here. The handling of statistical uncertainty, as can be seen in Figure 4.2, is a more pressing concern.

power spectral density (PSD) is given by [192]:

$$P(\omega) = \frac{1}{2} \frac{[\sum_i S(t_i) \cos(\omega(t_i - \tau))]^2}{\sum_i \cos^2(t_i - \tau)} + \frac{1}{2} \frac{[\sum_i S(t_i) \sin(\omega(t_i - \tau))]^2}{\sum_i \sin^2(t_i - \tau)}, \quad (4.54)$$

where $S(t_i)$ is the i -th sample of the signal under consideration, and

$$\tau = \frac{1}{2\omega} \arctan\left(\frac{\sum_i \sin(2\omega t_i)}{\sum_i \cos(2\omega t_i)}\right). \quad (4.55)$$

It is possible to show [192] that the PSD obtained by (4.54) is equal to

$$P(\omega) = \frac{1}{2} \left[\sum_i S(t_i)^2 - \min_{A,B} \sum_i (S(t_i) - Y[A, B, \omega](t_i))^2 \right], \quad (4.56)$$

with

$$Y[A, B, \tau, \omega](t_i) = A \cos(\omega t_i - \tau) + B \sin(\omega t_i - \tau); \quad (4.57)$$

this approach is known as the *least squares spectral estimation*. We can see that the second term in (4.56) is nothing but the χ^2 of our signal; therefore, we can handle the uncertainties in S by substituting it with the reduced- χ^2 for the model Y and the experimentally obtained $S(t_i)$ and σ_i [195]:

$$\chi_r^2 = \sum_i \left(\frac{S(t_i) - Y(t_i)}{\sigma_i} \right)^2. \quad (4.58)$$

We evaluate the PSD from 0 Hz to 1 kHz, with a frequency resolution of 2.5 Hz.[¶] From this data, we get the spectral peaks whose level is over the 5% false alarm probability threshold [200], in order both to have initial starting values for the subsequent fitting procedure and to estimate the number of frequencies to be included into the oscillation model. This is important because, while the theory predicts that both frequencies should appear in all the oscillations for both species, in practice some of them could be so suppressed that the results from the analysis of that frequency would not be accurate.

The second step is then doing a least square fit of the oscillation data directly with a sinusoidal model, which can be either

$$Y_s(t) = A e^{-t/\tau} \sin(\omega t + \phi) \quad (4.59)$$

for the single frequency case, or

$$Y_d(t) = A_+ e^{-t/\tau_+} \sin(\omega_+ t + \phi_+) + A_- e^{-t/\tau_-} \sin(\omega_- t + \phi_-) \quad (4.60)$$

for the double frequency. The minimization of the residual sum of squares is done with the Levenberg-Marquardt algorithm [201, 202], which has the twofold advantage of being

[¶]In the general case of non-uniform sampling, the Nyquist-like frequency is not the usual $N_f = f_s/2$, with f_s the sampling frequency, but much higher [196]. In our case, however, all the samples are at integer multiples of the sampling frequency, and so it reduces to $f_s/2$.

^{||}For this analysis, the software implementation used has been provided by the Astropy package, version 5.3.2 [197-199].

widely available in an already implemented form, and of providing estimates for the standard deviation of the fitted parameter value.** This is because the algorithm minimizes the χ^2 statistic by iteratively solving the system [202]

$$(\mathbf{H}_i + \lambda_i \mathbf{I})\boldsymbol{\delta}_{i+1} = \nabla \chi_{ri}^2, \quad (4.61)$$

where \mathbf{H} is the Hessian matrix of χ_r^2 for our model equation calculated at the point in fitting parameter space $\boldsymbol{\beta}_i = \boldsymbol{\beta}_{i-1} + \boldsymbol{\delta}_i$, χ_{ri}^2 is the reduced- χ^2 for the model calculated at $\boldsymbol{\beta}_i$, and λ_i is a parameter retuned at every step.†† Because of this, it is straightforward to get the covariance matrix $\mathbf{V} = \mathbf{H}^{-1}/2$ from the last algorithm step [205], and so the error estimates $\sigma_i = \sqrt{V_{ii}}$.

4.3. Frequencies and amplitudes of the oscillations

With this method, we obtain the frequencies and amplitudes of the oscillation for each species. First, the oscillation frequency for each eigenmode is averaged across the two species, in the cases for which it appears in both; then they are normalized to the bare oscillation frequencies of K and Rb, for the high and low mode respectively.

A graph of the frequencies for the different interspecies scattering length is shown in Figure 4.4, along with a comparison with both the Gross-Pitaevskii predictions, and with the Ehrenfest theorem predictions.

By looking at the graphs, we can see that the frequencies, as predicted from theory, differ substantially from the bare trap frequencies that would have been measured in the non-interacting case. We remark also that, for the in-phase mode, the accord with predictions, both with the models explored in Subsection 4.1.2 and with the GPE simulations, is good; for the out-of-phase mode, on the other hand, the discrepancies of the experimental results with the GPE simulations are larger, and the Ehrenfest-Sum rules results fail to describe the experimental data.

We can also observe from the figure that the relative magnitude of the in-phase and out-of-phase frequencies depend on the sign of the interactions: while for negative a_{12} the in-phase frequency is lower than the out-of-phase one, for positive scattering lengths the roles are reversed. This can be explained with an intuitive physical picture, derived from the eigenvalue analysis of (4.47): in the case of attractive interactions, the interaction energy is negative, and thus it is energetically favourable for the two condensates to move together, whereas for repulsive interactions, the lower energy motion is the one in which they spend the least time occupying the same portion of space.

The amplitudes of the K and Rb oscillations depend on how the eigenmode was projected on the single species mode, which, in turn, depends on the excitation protocol via the initial conditions of the dynamic equations; for this reason, we normalize the oscillation amplitude for each species to its corresponding value for the non-interacting case; a figure comparing the experimental values with the corresponding GPE predictions can be seen in Figure 4.5. There, we see that, for Rb, the out-of-phase mode is always suppressed below the detection threshold, but for the in-phase mode, there is a match with the prediction from the GPE simulations;

**The software implementation used here is from the Scipy package [203], version 1.10.1.

††The actual updating strategy differs from implementation to implementation; see, for example, [204].

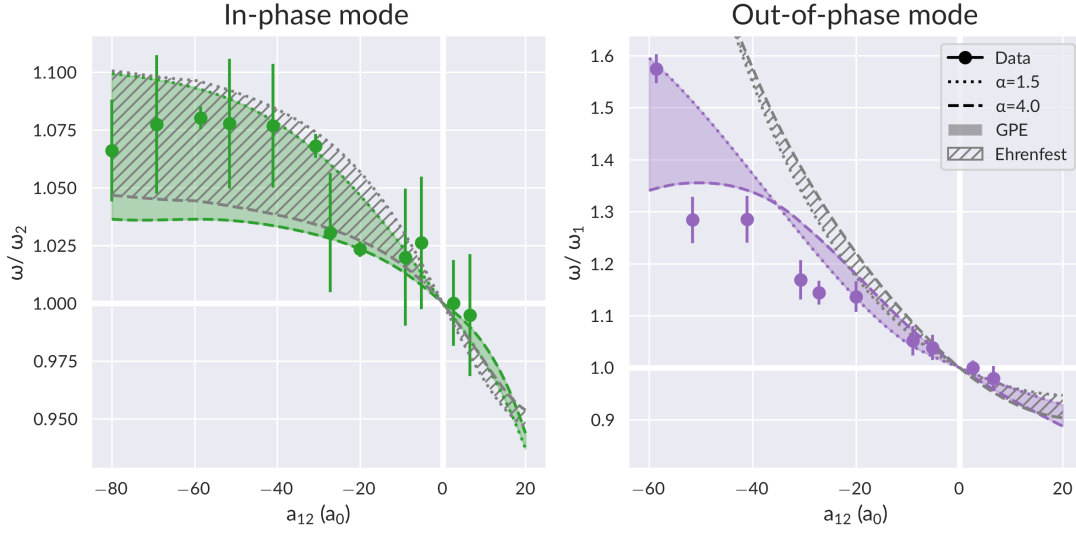


Figure 4.4.: Frequencies of the dipole oscillations for the low frequency mode (left panel) and the high frequency mode (right panel). The data points are the result of the least squares fits, averaged, where applicable, over the results obtained for the two species, and the error bars represent their standard errors. The dotted and dashed lines represent the theoretically calculated frequencies for the case of $\alpha = 1.5$ and $\alpha = 4.0$, respectively; the shaded areas between these lines represent the method used for the calculation of the theoretical values: solid (and color-coded for the respective mode) for the GPE simulations, and hatched grey for the Ehrenfest model values. The low mode frequencies are normalized to the non-interacting Rb frequency (ω_2), whereas the high mode frequencies are normalized to the non-interacting K frequency (ω_1). In both panels, the grid lines where $a_{12} = 0$ and $\omega_{\pm}/\omega_i = 1$ are emphasized.

for K, on the other hand, the out-of-phase mode is the only one visible for $a_{12} \gtrsim -20a_0$, then, in the range $-60a_0 \lesssim a_{12} \lesssim -20a_0$, both modes are visible, and, finally, for $a_{12} \lesssim -60a_0$, the out-of-phase mode is suppressed. This indicates that, in this last regime, the strength of the interspecies interaction is such that the two species oscillate in unison.

A more quantitative estimate of the discrepancy between the predicted and the experimentally measured frequencies can be made if we take the overlap integral between the probability distribution of ω and the predicted region. For a given fit result $\bar{\omega}$ with a standard error σ_{ω} , the overlap with the theoretically predicted region $[\omega_1, \omega_2]$ is

$$O = \int_{-\infty}^{+\infty} \mathbb{1}_{[\omega_1, \omega_2]}(\omega) \frac{1}{\sqrt{\pi 2 \sigma_{\omega}^2}} e^{-\frac{(\omega - \bar{\omega})^2}{2 \sigma_{\omega}^2}} d\omega \quad (4.62)$$

$$= \int_{\omega_1}^{\omega_2} \frac{1}{\sqrt{\pi 2 \sigma_{\omega}^2}} e^{-\frac{(\omega - \bar{\omega})^2}{2 \sigma_{\omega}^2}} d\omega \quad (4.63)$$

$$= \frac{1}{2} \operatorname{erf}\left(\frac{\omega_2 - \bar{\omega}}{\sqrt{2} \sigma_{\omega}}\right) - \frac{1}{2} \operatorname{erf}\left(\frac{\omega_1 - \bar{\omega}}{\sqrt{2} \sigma_{\omega}}\right) \quad (4.64)$$

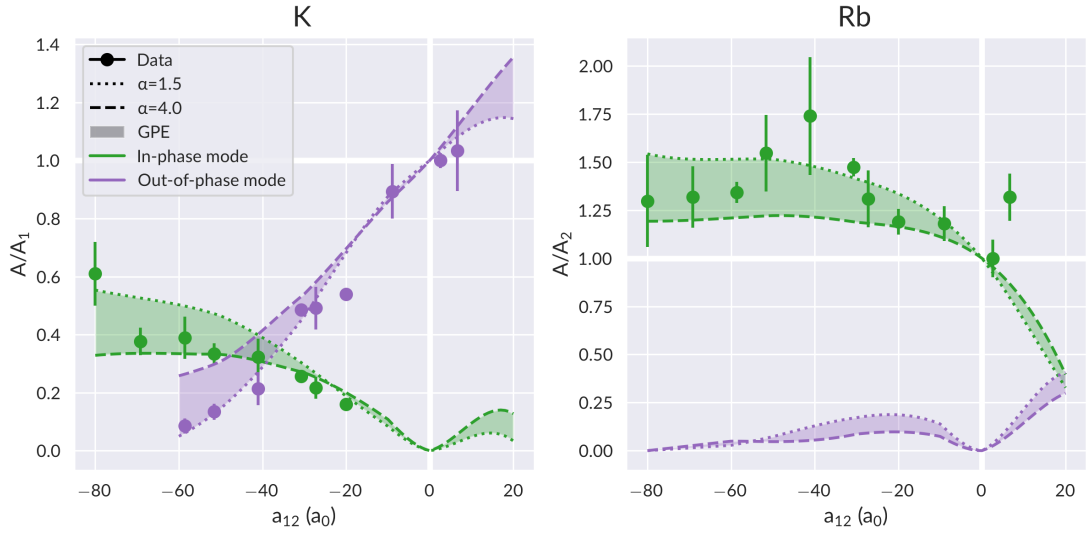


Figure 4.5.: Amplitudes of the dipole oscillations for K (left panel) and Rb (right panel). The data points are the results of the least squares fits, and the error bars represent their standard errors. The dotted and dashed lines represent the amplitudes extracted from the GPE simulations for the cases of $\alpha = 1.5$ and $\alpha = 4.0$, respectively. The amplitudes of the low frequency mode are represented coloured green, while those of the high frequency mode are coloured purple. Each amplitude is normalized to the amplitude of the respective species (A_1 for K, and A_2 for Rb) in the non-interacting case. In both panels, the grid lines where $a_{12} = 0$ and $A/A_i = 1$ are emphasized.

where $\mathbb{1}_S$ is the indicator function for the set S :

$$\mathbb{1}_S(x) = \begin{cases} 1 & \text{if } x \in S \\ 0 & \text{otherwise} \end{cases} \quad (4.65)$$

and erf is the error function of the standard Gaussian

$$\text{erf}(x) = \int_0^x \frac{1}{\sqrt{2\pi}} e^{-\frac{\xi^2}{2}} d\xi. \quad (4.66)$$

In order to make the comparison of different values possible, we normalize O by its maximum value O^* , which would occur if $\bar{\omega} = (\omega_2 + \omega_1)/2$. In Figure 4.6 the values of $|O/O^*|$ for both modes, comparing Ehrenfest and GPE predictions, are shown. There, we can see that, while for the in-phase mode both overlaps are comparable, for the out-of-phase mode the normalized overlap of the Ehrenfest prediction is consistently less than 1%, once we go below $\approx -20a_0$.

With respect to the Ehrenfest model, we can see that GPE simulations systematically predict lower energies. This is because, for the out-of-phase mode, the assumptions made in both the Ehrenfest and the sum rules treatment of the problem are not valid anymore: namely, the linearity assumption central to this problem is not fulfilled anymore. When the oscillations are

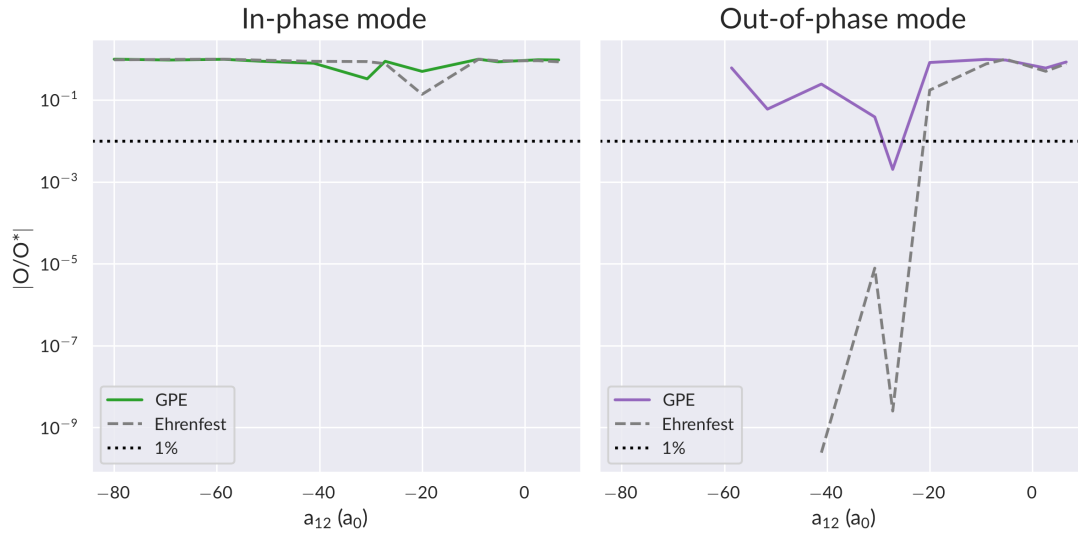


Figure 4.6.: Absolute value of the normalized overlap between the empirical frequency distribution and the theoretical prediction. The continuous lines represent overlaps with the GPE predictions, the dashed lines the overlaps with the Ehrenfest model predictions, and the dotted line a constant at 1%. In the right panel, Ehrenfest values for $a_{12} < -40a_0$ are cutoff, as the overlap is below the floating point precision of the machine on which these quantities were calculated ($\sim 10^{-16}$).

not linear, the modes in the multipole expansion are mixed, and therefore the rigid translation, that constitutes the dipole oscillation, is not the only collective excitation that is initially excited, that is to say that the initial density distribution changes shape. This is consistent with the sum rules theory, which states that the frequency it predicts is just an upper bound for the actual frequency, whenever there is more than one mode, i.e. out of the linear regime: from what we have said before, we see that the Ehrenfest predictions (which are identical to the sum rules predictions) are consistently higher than both the GPE and the experimentally detected values.

From Figure 4.5, instead, we can see that the out-of-phase amplitude of Rb is always suppressed below the detection threshold and, as such, has never been observed; the symmetric case is also true for K where the in-phase mode is never detected for $a_{12} > -20a_0$: this is because the mode which is due to the other species is suppressed until sufficient mixing is achieved, i.e. until the interactions are sufficiently strong. The out-of-phase mode is, for scattering lengths $a_{12} < -60a_0$, absent also in the K oscillation, as in this region the two condensates tend to stick together.

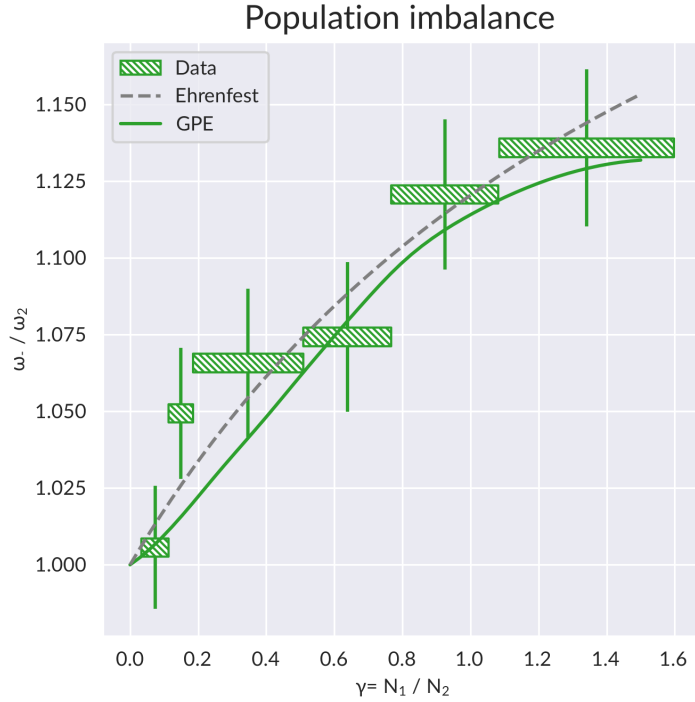


Figure 4.7.: Effect of the population imbalance on the oscillation frequency, keeping fixed the intraspecies scattering length at $a_{12} = -83.4a_0$. The hatched rectangles represent the experimental data, where the horizontal width of the rectangle represents the width of the binning interval, and the error bars the standard error on the fit result. The continuous line represents the GPE prediction, while the dashed line the Ehrenfest prediction.

4.4. Role of population imbalance

In the strongly attractive regime, as we have seen before, the in-phase mode is strongly enhanced over its competitor. The frequency of this mode tends to the bound state value

$$\omega_b = \sqrt{\frac{N_1 m_1 \omega_1^2 + N_2 m_2 \omega_2^2}{N_1 m_1 + N_2 m_2}}, \quad (4.67)$$

which as an intuitive physical interpretation as the weighted mean of the two bare frequencies, where the weights are the total masses of the condensates. In order to assess the precision of (4.67), we compare it with experimental data taken at a fixed interspecies scattering length, $a_{12} = -83.4a_0$, and with a wide range of α , from 0.74 to 14.3. The oscillation data is binned into six bins, in order to have an appropriate number of points at each evolution time t_e for each of the bins, and then they are fitted. We can see in Figure 4.7 the comparison between the experimental frequencies, the frequencies extracted from the GPE with an added LHY

term to the energy functional, and the classical bound state prediction

$$\frac{\omega_b}{\omega_2} = \sqrt{\frac{\gamma \frac{m_1}{m_2} \left(\frac{\omega_1}{\omega_2}\right)^2 + 1}{\gamma \frac{m_1}{m_2} + 1}}, \quad (4.68)$$

where $\gamma = 1/\alpha = N_1/N_2$. We can see that there is a good agreement between the predictions and the data for both predictions: more quantitatively, a Kolmogorov-Smirnov goodness-of-fit test [206] for $(\omega_{\text{th}} - \omega_{\text{exp}})/\sigma_\omega$ does not reject the null hypothesis that the residuals belong to standard normal distributions (p-values ≈ 0.6 and ≈ 0.2 for the GPE and Ehrenfest predictions, respectively), and a two sample Kolmogorov-Smirnov test does not reject the null hypothesis that the residuals come from the same distribution (p-value ≈ 0.5).

Given that, as mentioned above, the GPE simulation includes a LHY term in the energy functional, which is necessary due to the fact that $-83.4a_0$ is well within the mean-field-collapse region; on the other hand, the frequency prediction (4.67) does not include beyond-mean-field effects, as the bare trap frequencies are insensitive to intraspecies interactions. The inability of distinguishing between the two makes us conclude that, within our experimental precision, we are not able to see beyond mean field effects on the dipole oscillation of the droplet.

In order to confirm whether the oscillating gas is actually in a droplet state, we follow the time-of-flight expansion of the cloud, varying the time of flight from 10 ms to 25 ms, while keeping the interspecies interaction strength at the same value of $-83.4a_0$. The cutoff for the TOF is equal to the lifetime for this kind of droplets, as measured in [65]: this is much shorter than the TOF for the oscillation measurement, which is 35 ms for K; for this reason, the presence of a droplet state could not be directly confirmed during the measurement of the oscillation frequency. Because the atomic cloud expand during the TOF, we conclude that, in conditions identical to those encountered during the dipole oscillation, droplet states did not form. The only way in which we were able to create a non-expanding droplet was by going further on the attractive side, but the density of the resulting condensate greatly increased the three body losses, making it impossible to meaningfully see any in-trap dynamics.

4.5. Oscillation damping

The amplitude of the dipole oscillations was experimentally observed to decay with time; this consideration was already included in the fitted model equations (4.59) and (4.60). In order to have a more controlled insight into what happens with the decay, we acquired, for interspecies scattering lengths of $a_{12} = -58.6a_0$ and $a_{12} = -19.5a_0$, one set of measurements with initial displacement of $3.5 \mu\text{m}$ for K and $1.5 \mu\text{m}$ for Rb, along with their respective non-interacting oscillations; for the corresponding oscillations, the initial amplitudes were $2.35 \mu\text{m}$ for K and $0.74 \mu\text{m}$ for Rb. These oscillations are visible in Figure 4.8, with the results of the fit reported in Table 4.1.

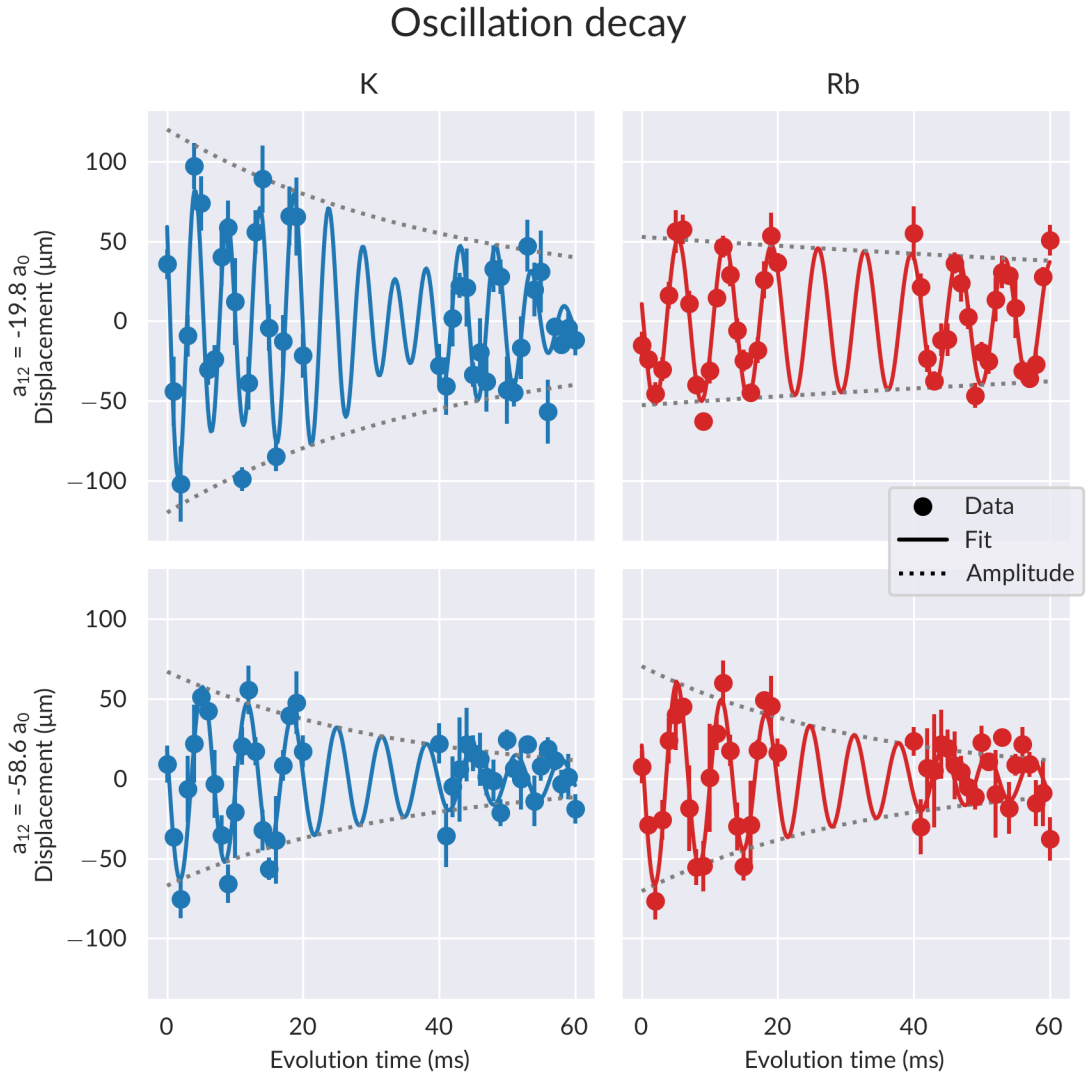


Figure 4.8.: Dipole oscillation decay for a large initial displacement (Rb: $1.5 \mu\text{m}$, K: $3.5 \mu\text{m}$), for two different values of a_{12} ($-19.5 a_0$, $-58.6 a_0$). The dots represent the mean of the points acquired for the same evolution time t_e , and the error bars their standard error, the continuous line represents the prediction from the fit results, and the dotted lines the envelope of the oscillation, as predicted by the fit.

Table 4.1.: Oscillation decay times for the oscillations shown in Figure 4.8. The decay times are obtained by fitting with the procedure detailed in Section 4.2. We indicate with $+\infty$ a decay time for an observed mode when $1/\tau$ would be compatible with 0; we indicate with a dash (—) the lack of a decay time due to an unobserved mode.

$a_{12} (a_0)$	K		Rb	
	τ_L (ms)	τ_H (ms)	τ_L (ms)	τ_H (ms)
0	—	80(20)	130(40)	—
-19.8	$+\infty$	30(10)	160(50)	—
-58.6	40(10)	—	41(8)	—

From these results, we can see that the damping time depends on the interspecies interaction. When the condensates are not interacting, the damping is purely dependent on the anharmonicity of the trap, which couples the dipole mode to other collective modes. For moderately attractive interactions ($a_{12} = -19.8a_0$), the damping times of the low frequency mode are unchanged with respect to the non interacting case (the comparison is only possible in Rb, where the low mode is present also without interspecies coupling), while the lifetime of the high-frequency mode is remarkably shorter. Finally, in the strongly interacting regime ($a_{12} = -58.6a_0$), the damping time is the same in both species, as is to be expected for almost unison motion.

Concerning the damping of the high mode at moderately attractive interactions, we note that, for this mode and in this interaction regime, the motion of the condensate is out-of-phase and, therefore, one possible hypothesis is that the relative velocity, in some parts of the oscillation, exceeds the critical superfluid velocity, thereby exciting other modes. For our case, the critical (rescaled) momentum \tilde{k}_c is given by [207]:

$$2\tilde{k}_c^2 = (\sqrt{\gamma_m} + \sqrt{\gamma_2})^2 \left(1 - \frac{\gamma_{12}}{\sqrt{\gamma_2}}\right) + \alpha\gamma_{12}(\sqrt{\gamma_2} + \gamma_{12})^2 + \beta\gamma_{12}^2(\sqrt{\gamma_2} - \gamma_{12}), \quad (4.69)$$

where we have defined

$$\alpha = (\sqrt{\gamma_2} + \sqrt{\gamma_m})(\sqrt{\gamma_2} - 2\sqrt{\gamma_m\gamma_2} + \sqrt{\gamma_m})\gamma_2^{-3/2} \quad (4.70a)$$

$$\beta = (\gamma_m - 2\sqrt{\gamma_2\gamma_m} + \gamma_2)\gamma_2^{-3/2} \quad (4.70b)$$

$$\gamma_2 = \frac{g_{22}n_2}{g_{11}n_1} \quad (4.70c)$$

$$\gamma_{12} = \frac{g_{12}\sqrt{n_1n_2}}{g_{11}n_1} \quad (4.70d)$$

$$\gamma_m = \frac{m_2}{m_1}, \quad (4.70e)$$

and the critical momentum \tilde{k}_c is related to the critical relative velocity v_c by

$$\tilde{k}_c = \frac{m_2v_c}{\sqrt{2m_2g_{11}n_1}}. \quad (4.71)$$

We can therefore calculate v_c : from the simulations, we know that, for $a_{12} = -19.8a_0$, the maximum density of the condensates is $180 \mu\text{m}^{-3}$ for K and between $254 \mu\text{m}^{-3}$ and $367 \mu\text{m}^{-3}$ for Rb, depending on the atom number; the critical relative velocity is, therefore, between 8.2 mms^{-1} and 8.9 mms^{-1} . Also from the simulation data, we can say that the maximum velocity is within the interval 2.05 mms^{-1} – 2.18 mms^{-1} .

Given that this range is much lower than the critical velocity range, we can say that the damping of the out-of-phase mode is less likely due to counterflow instability; however, the calculation was done assuming that the relevant density for the calculation of the critical velocity is the maximum density, which is strictly true only for homogeneous condensates: for trapped condensates, even in the simple case given by the local density approximation, there could still be (and, from a strictly mathematical point, there is certainly) a region in which the critical velocity is below the observed maximum velocity. In conclusion, counterflow instability cannot be ruled out, although within our current framework is a disfavoured explanation for the oscillation damping.

High resolution imaging of a Bose-Bose mixture

The implementation of a high resolution imaging system has been planned for the K-Rb experiment since the design of the vacuum apparatus, where the re-entrant viewports have the express purpose of being closer to the atomic cloud, enabling imaging at higher numerical apertures. The necessity for a high-resolution system is further corroborated by the aim of imaging quantum droplets, whose size is below the resolution of the current imaging ($\approx 5 \mu\text{m}$), and of further studies into multicomponent superfluidity of the K-Rb mixture, where the production of vortices, for example, would also not be detectable with the aforementioned system.

To do so, we characterize and mount an high-resolution objective that was developed in [208]. In Section 5.2, we will look more in detail at the design of the objective and of the MOT compensation scheme; we will then proceed to the characterization of its performance in Section 5.3. In-situ imaging of the mixture necessitates the tuning of probe beam frequency and polarization: those concerns are addressed in Section 5.4. Finally, the high-resolution image of a double condensate is shown in Section 5.5.

5.1. Absorption imaging of degenerate quantum gases

Absorption imaging is the most widely used technique to probe degenerate quantum gases, due to its versatility and relative simplicity [209].

Let's assume that an electric field with amplitude E_0 and frequency ω is impinging on an atomic cloud. The electric field, while being absorbed and refracted by the cloud, is

$$E'(z) = E_0 e^{i\omega(\tilde{n}z/c - t)}, \quad (5.1)$$

where \tilde{n} is the complex refractive index [210]; for a gas of two level atoms, \tilde{n} is [209]

$$\tilde{n} = 1 + \rho \frac{\sigma_0 \lambda}{4\pi} \frac{i - \delta}{1 + \delta^2}, \quad (5.2)$$

where ρ is the atomic density,

$$\sigma_0 = \frac{3}{2\pi} \lambda^2 \quad (5.3)$$

the resonant cross-section,

$$\delta = \frac{\omega - \omega_0}{\Gamma/2} \quad (5.4)$$

the detuning, ω_0 is the transition frequency, and Γ its width.

The intensity of this beam is given by the Lambert-Beer law

$$I(z) = I_0 \exp\left(-\frac{4\pi}{\lambda} \text{Im}(\tilde{n})z\right) \quad (5.5)$$

$$= I_0 \exp\left(-\rho(z) \frac{\sigma_0}{1 + \delta^2} z\right); \quad (5.6)$$

the total absorption of the cloud is

$$I = I_0 \exp\left(-\frac{\sigma_0}{1 + \delta^2} \int \rho(z) dz\right) \quad (5.7)$$

$$= I_0 e^{-\text{OD}}, \quad (5.8)$$

where in the last passage we have defined a quantity called optical density. We see that

$$OD(x, y, z) \propto \int \rho(x, y, z) dz \quad (5.9)$$

$$= \int |\Psi(x, y, z)| dz, \quad (5.10)$$

and, therefore, by imaging the optical density, we will obtain the spatial distribution of the wave function of the atomic cloud.

Experimentally, the intensity distribution will not be uniform and, therefore, a simple logarithm of $I(x, y)$ will not give the desired information. A more general form of the transmitted intensity is [209]:

$$I(x, y) = I_0 \left(P(x, y) e^{-\text{OD}(x, y)} + S(x, y) \right) + N(x, y), \quad (5.11)$$

where P is the normalized beam profile in the object plane, S is the light scattered after the object plane, and N is the external background light. Therefore, if we acquire an image of the same beam, but without the atoms,

$$I_2(x, y) = I_0 \left(P(x, y) + S(x, y) \right) + N(x, y) \quad (5.12)$$

and another of the background

$$I_3(x, y) = N(x, y) \quad (5.13)$$

we can calculate the optical density, by supposing S small,

$$OD(x, y) = -\ln \frac{I(x, y) - I_3(x, y)}{I_2(x, y) - I_3(x, y)}. \quad (5.14)$$

Table 5.1.: Technical data for the asphere [211] and meniscus [212] lenses in the objective.

	Asphere	Meniscus
Diameter mm	$40.000^{+0.000}_{-0.025}$	30.0 ± 0.1
Clear aperture mm	39.00	>27
Centre thickness mm	14.7 ± 0.1	2.40 ± 0.05
Coating	600 nm–1050 nm	Uncoated
Material	N-SF5 (Schott)	UVFS
Producer	Edmunds Optics Inc.	Fuzhou Solid Photon
Catalogue number	16-986	Custom

While the performance of the imaging system should theoretically be the same for each shot, it is nevertheless important to remark that the optical density obtained in (5.14) is accurate as long as there are no external vibrations, which shift P , S and N and cause additional noise in the optical density image. Therefore, mechanical vibrations shall be reduced as much as practically possible, and, with high magnification imaging systems such as the one described in this chapter, a way of reducing this noise may also be needed, as we will see in Section 5.5.

5.2. Design

The high-resolution objective to be used in this experiment had been previously designed [208]: the design characteristics will be briefly summarized in Subsection 5.2.1. Due to the fact that the tube occupies a space in which the MOT beam also passes, a scheme for the compensation of the objective is needed: we will talk about this scheme in Subsection 5.2.2

5.2.1. Description of the objective

The objective is composed of two lenses: an asphere and a meniscus. The aspheric lens is an Edmunds plano-convex lens, with a numerical aperture of 0.5 and an effective focal length of 40 mm. The meniscus is a custom ordered Solid lens, it has a focal length of 1000 mm and a diameter of 30 mm, and its purpose is the compensation of the glass of the vacuum chamber viewport. More technical data on the objective can be found in Table 5.1. A technical drawing of the objective, showing the lenses and the tube, is shown in Figure 5.1

The objective tube has a diameter of 53 mm: this was chosen in order to fit inside the internal hole of the housing of the magnetic coils; similarly, its free length (84 mm) was chosen as to be able to clear completely the height of said housing while the objective rests on the vacuum chamber window.

The objective body and the retaining ring for the aspheric lens are made of polyether ether ketone (PEEK) plastic: this material was selected both for its excellent mechanical stability properties, and for its lack of magnetism. The spacer ring is made of machined aluminium, in order to ensure the best possible dimensional tolerances: while aluminium is not completely amagnetic, its effects on the atoms consist of the introduction of a spurious magnetic field, which however can be eliminated by appropriately setting our compensation coils, and of a

reduced efficiency of the atomic transfer at low magnetic fields of around 5 G–10 G, which however can be compensated by transferring the atoms at higher fields (72.8 G, see Section 3.3).

The optical system formed by the viewport, the meniscus, and the objective lens was simulated with ray tracing software [208]. These simulations give some figures of merit with which the optical performance of a system can be characterized.

The most used and usually most relevant figure of merit is the resolution, which is the minimum distance between two point-like sources to be distinguishable. Due to the wave nature of electromagnetic radiation (in the regimes relevant to our discourse), the image of a point-like object is not another point, but rather a diffraction pattern: for a perfect system with radial symmetry, this pattern is given by an Airy function. The most common definition of resolution, called Rayleigh’s criterion, prescribes that two points are resolved when the peak of one point is on the minimum of the other; from this, we can obtain the formula for the resolution of an optical system [213]:

$$\delta = 1.22 \frac{\lambda}{\text{NA}}, \quad (5.15)$$

where λ is the wavelength of the imaging light and NA is the numerical aperture

$$\text{NA} = n \sin(\theta), \quad (5.16)$$

with n the refractive index of the propagation medium, and θ the maximum acceptance angle for an object at the focal length. For a non perfect imaging system, the function will, in general, be different from an Airy pattern; the intensity distribution of the image of a point-like object is called the point-spread function (PSF) of the system.

A second metric, closely related to the PSF, is the Strehl ratio. This is defined as the fraction of the light that falls inside the central maximum of the PSF, and can be used to measure aberrations. This is because the Strehl ratio can be related to the RMS value of the difference between the ideal and the real wave fronts on the surface of the optical system, σ_ϕ [214]:

$$\text{SR} = e^{-\sigma_\phi^2} \quad (5.17)$$

An optical system is considered, by convention, diffraction limited if $\text{SR} \gtrsim 0.8$. The PSF and SR are usually given for the point in the image plane which intersects the optical axis. If we, instead, calculate the SR as a function of the distance r from the optical axis, we can define the diffraction limited field of view as

$$r_{\text{fov}} = \min\{r \text{ s.t. } \text{SR}(r) \leq 0.8\}. \quad (5.18)$$

Another relevant figure of merit is the cutoff frequency. Due to the finite resolution we mention above, we can think of any optical system as a filter: we can think of the PSF as the impulse response function of the system. Due to the linearity of the optical system (in the far field), we can write the output intensity I_o as the convolution between the PSF and the input intensity I_i [213]:

$$I_o(x, y) \propto \int |\text{PSF}(x - x', y - y')| I_i(x', y') dx dy. \quad (5.19)$$

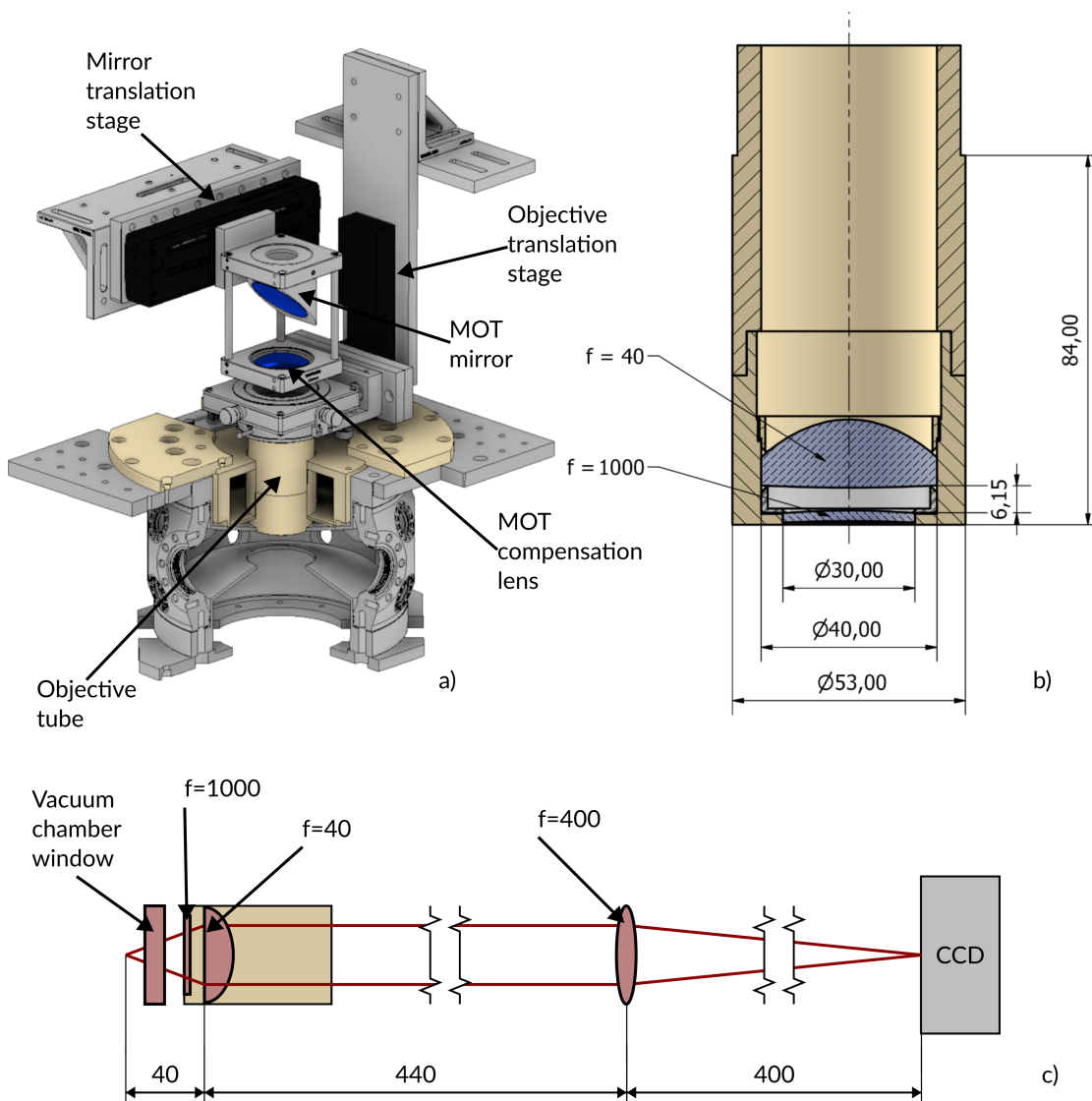


Figure 5.1.: High resolution imaging system: view of the objective inside the apparatus (a), technical drawing of the objective (b), and (simplified) optical scheme (c) in the $10\times$ configuration. The objective is in the vertical direction, which allows to be closer to the atoms due to the re-entrant viewports. The vertical direction is, however, also the direction of one of the MOT beams. In order to be able to have two beams in the same direction, a remote controlled translation stage moves a cage in which a mirror and a 75 mm lens are coaxially mounted. MOT compensation is treated in more detail in Subsection 5.2.2. In (b) we see that the objective is composed of two lenses, an asphere with focal length of 40 mm, and a meniscus with focal length 1000 mm, which is used for compensation of the vacuum chamber window. As for (c), the image is magnified 10 times before being collected on a CCD. All the optics are mounted on a breadboard above the vacuum chamber, and parallel to the horizontal plane; the optical axis is bent 90° between the two lenses (not shown in (c)).

Table 5.2.: Optical data for the objective, from the simulations in [208]. The depth of field is an upper bound, and the actual depth of field is lower.

	Illumination wavelength	
	780 nm	766 nm
δ (μm)	1.34	1.32
Effective f (mm)	39.43	39.4
Effective NA	0.3553	0.3551
k_0 (lp/mm)	915.1	932.3
On axis SR	0.917	0.914
r_{FOV} (mm)	0.187	0.179
DF (mm)	$\ll 0.025$	

A convolution in the Fourier domain becomes a multiplication, therefore

$$\mathcal{F}[I_o](k_x, k_y) = \text{OTF}(k_x, k_y)\mathcal{F}[I_i](k_x, k_y), \quad (5.20)$$

where $\mathcal{F}[g]$ denotes the Fourier transform of g ; from this equation, we can see that the intrinsic properties of the optical system are completely described by the optical transfer function (OTF), which is defined as the normalized Fourier transform of the PSF:

$$\text{OTF}(k_x, k_y) = \frac{\mathcal{F}[\text{PSF}](k_x, k_y)}{\int |\text{PSF}(x, y)|^2 dx dy}. \quad (5.21)$$

It can be shown [213] that, for coherent light on a circular aperture, the *OTF* of a perfect optical system with diameter D , effective focal length f , and imaging wavelength λ is not null up for frequencies

$$k = \sqrt{k_x^2 + k_y^2} \leq k_0 = \frac{D}{2\lambda f}, \quad (5.22)$$

which defines the cutoff frequency k_0 . The cutoff frequency is generally measured in lp/mm (line-pairs per mm); a line-pair is defined in object space as two rising edges from maximum to minimum light intensity (or vice-versa), therefore $1 \text{ lp/mm} = 2 \text{ mm}^{-1}$.

Finally, one last parameter is the depth of field (DF), which is the maximum distance that an object can be from the focal plane in order to be acceptably focused.

The figures of merit here defined, taken from the simulations in [208], are reported in Table 5.2. From there, we can see that the objective performs reasonably well within the target resolution of $1 \mu\text{m}$ – $2 \mu\text{m}$, which is the expected size of a double BEC well within the MF collapse regime (see Section 5.5). We can also remark that the objective is diffraction limited, having an SR above 0.9. It is also important to notice that there is significant chromatic aberration: the distance between the focal plane for K and for Rb is of $20 \mu\text{m}$, which is more than the depth of field, and which will have to be compensated (see Section 5.5 for more details).

After the objective, a second lens acts as a tube lens, as we can see from Figure 5.1c. This second lens is a $f = 400 \text{ mm}$, $D = 50.8 \text{ mm}$ from Thorlabs,* which grants a total magnification

*Catalogue number LA1725-B.

factor of 10. The (linear) pixel size of the CCD used[†] is $16\ \mu\text{m}$ [215], and, therefore, a pixel in the object plane would cover $1.6\ \mu\text{m}$. In order to improve pixel usage, a second telescope with magnification 2 was later mounted with its object plane on the image plane of the tube lens.

5.2.2. MOT compensation

As we can see from Figure 5.1a, the objective is in the path of the vertical MOT beam coming from above, and would be focalized on the atomic sample, were it not for some kind of objective compensation.[‡]

Whereas the design of the objective lens needs specialized software, ray tracing the system needed for MOT compensation is much easier, using matrix optics. This kind of treatment of optical systems is valid in the paraxial approximation: for a ray of light coming at an angle θ with the optical axis, the paraxial approximation is $\sin(\theta) \approx \theta$, which is valid in the $\theta \ll 1$ regime (paraxial condition).

Here, we can represent a ray of light as a vector [216]

$$\begin{pmatrix} y \\ \theta \end{pmatrix}, \quad (5.23)$$

where theta is the aforementioned angle, and y is the ray's height from the optical axis. The action of a single optical element on the ray is then represented by a 2×2 (real) matrix, and the whole system will then be represented by the product of the matrices representing the optical elements.

For this design, we will need only two matrices: the translation matrix, representing empty space between two elements,

$$\mathbf{T}(d) = \begin{pmatrix} 1 & d \\ 0 & 1 \end{pmatrix}, \quad (5.24)$$

and the thin lens matrix

$$\mathbf{L}(f) = \begin{pmatrix} 1 & 0 \\ -1/f & 1 \end{pmatrix} \quad (5.25)$$

After some preliminary trials, we concluded that a three lens configuration, with $f_1 = -1000\ \text{mm}$, $f_2 = 75\ \text{mm}$, and $f_3 = 40\ \text{mm}$ as the respective focal lenses, could provide a good compensation, while keeping at a minimum the number of optical elements needed. The total transfer matrix for this system will then be:

$$\mathbf{M} = \mathbf{T}(d_3)\mathbf{L}(f_3)\mathbf{T}(d_2)\mathbf{L}(f_2)\mathbf{T}(d_1)\mathbf{L}(f_1); \quad (5.26)$$

in writing this, we have neglected both the viewport and the compensation meniscus.

As we are interested in keeping the beam as similar as possible to the input MOT beam, we will look at magnification

$$m_y = \frac{y_{\text{out}}}{y_{\text{in}}} \quad (5.27)$$

[†]Andor (Oxford Instruments), iXon Ultra 897 EMCCD.

[‡]As mentioned in Section 3.1, each the MOT beams are not made from a single retroreflected beam, but by two independent beams. In this case, the vertical MOT beam coming from below has already interacted with the atoms, and therefore does not need any compensation.

and beam divergence

$$m_\theta = \theta_{\text{out}} - \theta_{\text{in}}; \quad (5.28)$$

we are interested in making the former as close as possible to 1, and the latter as close as possible to 0. In order to do so, we define $d_3 = 80$ mm, in order to account for the travel through the vacuum chamber and have a reasonable safety factor. We will then find the optimal distances d_1 and d_2 by solving the optimization problem

$$\min f(d_1, d_2) \quad (5.29)$$

$$800 \text{ mm} \leq d_1 \leq 1000 \text{ mm} \quad (5.30)$$

$$130 \text{ mm} \leq d_2 \leq 150 \text{ mm} \quad (5.31)$$

$$1000 \text{ mm} \leq d_1 + d_2 \leq 1100 \text{ mm}, \quad (5.32)$$

where the target function is either

$$f_y = (m_y - 1)^2 \quad (5.33)$$

to find the parameters that correspond to the best magnification, or

$$f_\theta = (m_\theta \bmod 2\pi)^2 \quad (5.34)$$

to find those that give the best divergence. The constraints are given by the mechanical dimensions of the apparatus.

Solving the problem,[§] we find that the optimal parameters for f_y are $d_1 = 870$ mm and $d_2 = 130$ mm, while for f_m they are $d_1 = 950$ mm and $d_2 = 150$ mm. These values are at the extremes of the acceptable region, so we try to find another optimum for f_θ inside the region; this also gives a compromise between the two functions. We find it at $d^1 = 908$ mm and $d^2 = 134$ mm; we will use this point for further characterization of the compensation system. These results are summarized in Figure 5.2.

We then proceed to ray trace the system, using the parameters found so far. The input beam is collimated, and has a diameter of 25 mm, as this is the diameter of the $\lambda/4$ wave plate that sets the MOT beam polarization. The results of this ray tracing can be seen in Figure 5.3. The magnification and divergence give acceptable results, with $|m_y| \approx 1.4$ and $m_\theta \approx 0^\circ$.

However, the beam is cut at the last lens (we consider its diameter as the diameter of the objective entrance): the beam radius is 1.34 mm too big. To see if this loss is acceptable, we put an iris on the path of the MOT beam which will be affected, and progressively close it: we find that the MOT is well within acceptability limits for apertures higher than 13 mm, concluding therefore that the restriction due to the objective entrance aperture does not preclude a successful compensation with this scheme.

In order to switch between the probe and the MOT compensation, we will have to move the 75 mm lens and the MOT mirror (see Figure 5.1) out of the way after the MOT. This is done by mounting both the lens and the mirror on a coaxial mount, and by placing this mount on a translating stage,[¶] which can then be toggled between the MOT and the probe position by a TTL signal from our control system.

[§]The solution is found the constrained optimization routines of the Scipy Python package [203], using a constrained trust-region algorithm [217].

[¶]Thorlabs DDS100/M linear direct-drive translation stage.

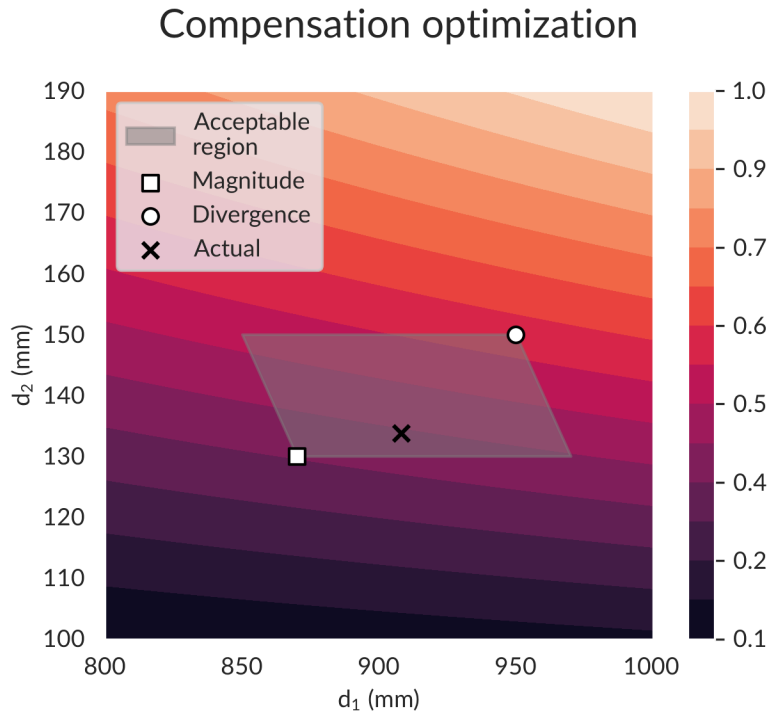


Figure 5.2.: Optimization of the MOT compensation scheme. The contour plot represents the length of the vector (m_y, m_θ) , and the shaded area the region for which the constraints are valid. Three points are also included, corresponding to the minimum of f_y , the minimum of f_θ , and a compromise point in between.

5.3. Objective performance

In order to evaluate the actual performance of the objective, we will have to acquire its PSF and MTF. We have mounted to this purpose the objective on a test bench, with an optical setup identical to that used in Figure 5.1. More specifically, the same lenses as those used in the final setup of the optical system, in its 10x configuration, have been used for this test, and a glass window, equivalent to those used for the vacuum chamber, was put between target and objective, to simulate the effects of the viewport. The illumination was provided by a 780 nm ECDL.

The evaluation of the MTF is usually done by imaging a standard pattern, known as the 1951 USAF resolution test chart [218]. This test chart is made of three-line elements, repeated in a horizontal and vertical orientation, and labelled with a number from 1 to 6; they are further collected into groups of six, each in turn also designated with a number. The spatial frequency k , in lp/mm, for the element e of the group g , is

$$\log_2 k = g + \frac{e-1}{6}. \quad (5.35)$$

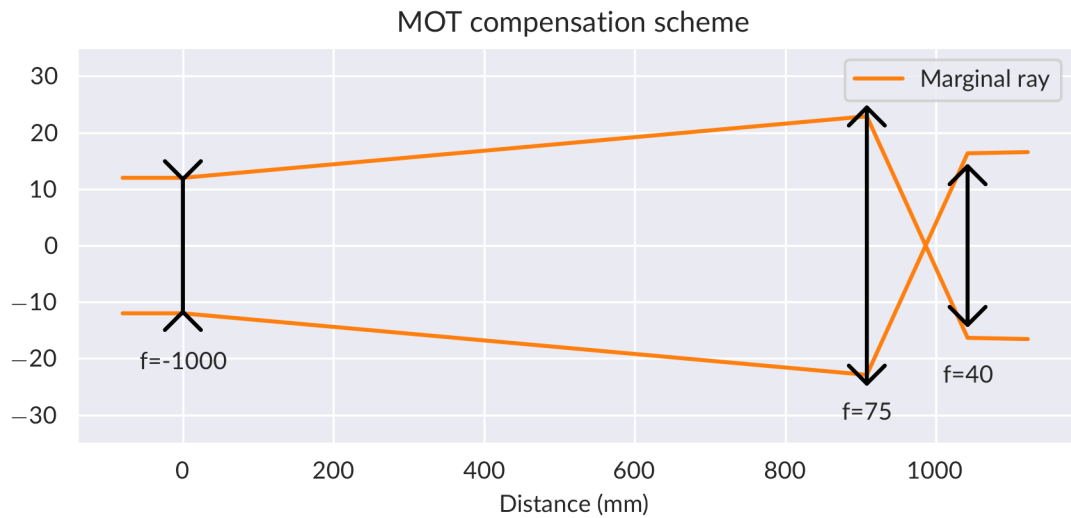


Figure 5.3.: Optical scheme for the MOT compensation. The orange line represents the ray tracing of a marginal ray, going from the left to the right. We can see that this system preserves collimation to a good degree, and that the magnification is close to 1. On the last lens (corresponding to the objective), we see that the laser beam is cut by the aperture of the objective, but the reduction in diameter is still within a value amenable to the MOT.

Test target

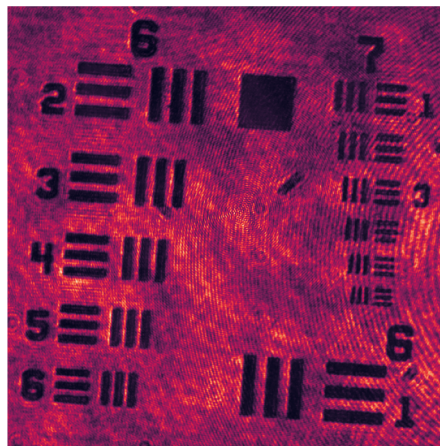


Figure 5.4.: Image of the USAF 1951 resolution chart, acquired using a test assembly of the high-resolution imaging system. The visible groups in this image are group 6 and 7, the smallest present in the target at our disposal. We can see that both horizontal and vertical lines in the sixth element of the seventh group are clearly visible. The performance of the optical system is therefore sufficient to image frequencies up to, at least, 228 lp/mm.

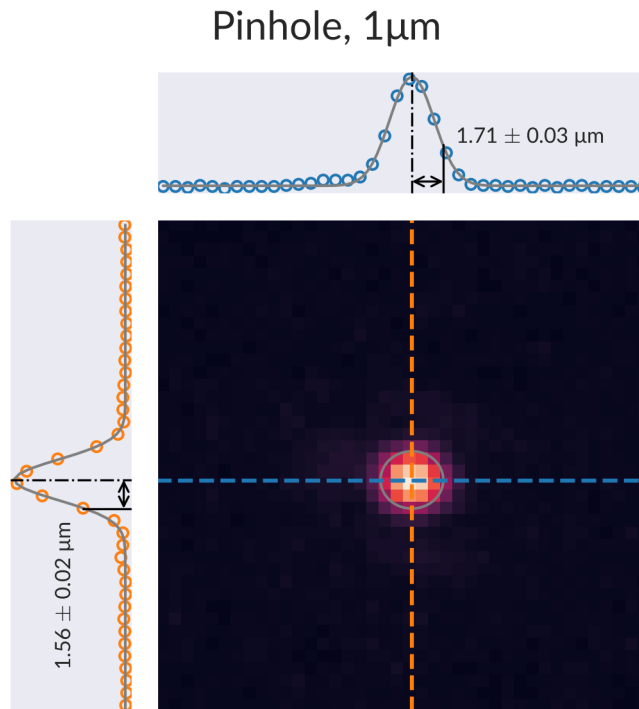


Figure 5.5.: Image of a pinhole with diameter of 1 μ m. This image well approximates the PSF. In the left and upper panels, we can see the slices of the image passing through the centre, also indicated by the dashed line of the corresponding colour in the intensity image. The gray continuous line is the result of the fit of the respective image slice, with the waist and its width indicated. The two measured waists are $1.71 \mu\text{m} \pm 0.03 \mu\text{m}$ and $1.56 \mu\text{m} \pm 0.02 \mu\text{m}$ in the horizontal and vertical directions, respectively. Their difference indicates a slight astigmatism of the optical system. The theoretical waist from the simulated PSF is $1.52 \mu\text{m}$, which indicates agreement with the vertical waist, and a small (13%) discrepancy with the horizontal waist.

It is then possible, by visual inspection of the resulting image, to have some rough indication of the capabilities of the optical system at the spatial frequency of the observed element.

The image of the sixth and seventh groups of a test target is shown in Figure 5.4. From there, we can see that, in the smallest element of the group seven, the lines are visible in both directions, and that means that the optical system performs to specification, at least up to 228 lp/mm. From the test target, we can also see that the effect of fringing, due to the coherence of the optical source, has an impact on image quality, particularly in the vicinity of optical defects. This is a known problem for imaging with lasers, and solutions have been proposed to obviate it [219]; however, due to the additional technical complexity and the limited quantity of light available for the probe beam, we decided against implementing such a measure, and therefore it was not tested.

The PSF instead is well approximated by imaging an object whose size is below the expected resolution. We tested the resolution of the imaging by projecting a pinhole with a diameter

of $1\ \mu\text{m}$; the image of this pinhole can be seen in Figure 5.5. In order to extract quantitative information, we took a slice of the image, passing through its centre, and fitted it with a Gaussian function; this was done for each of the two directions. The obtained values for the waists, in pixels, are then divided by the magnification factor of 10, and multiplied by the pixel size of the camera used for the acquisition, of $6.7\ \mu\text{m}$. This gives us waists of $1.56\ \mu\text{m} \pm 0.02\ \mu\text{m}$ for the vertical direction, and $1.71\ \mu\text{m} \pm 0.03\ \mu\text{m}$ for the horizontal direction.^{||} The same value, extracted by fitting the same function to the simulation PSF, is $1.52\ \mu\text{m}$ [208], so in the horizontal direction the agreement is good, while in the vertical direction there is a 13% discrepancy. This difference in values could indicate an astigmatism either of the objective in itself, or a slight misalignment of the optical system; either way, such a discrepancy is to be expected in any optical system.

We also tested the dispersive characteristics of the objective. For this purpose, we recorded the distance between the focal points of the $1\ \mu\text{m}$ pinhole with two wavelengths: 780 nm, and 635 nm. We find that the focus is displaced by $2.18\ \mu\text{m}\text{nm}^{-1}$, which would give $30.5\ \mu\text{m}$ as the distance between the foci for K and Rb.

Due to the performance of the objective within our design targets, we decided to mount it on the apparatus.

5.3.1. Magnification calibration

To have a reliable estimate of the condensate size, the actual magnification of the imaging system, as mounted on the apparatus, has to be assessed.

In order to achieve this, we use a method with two separate calibrations. First, we calibrate the pixel size of our frontal imaging, and, then, we do a series of fixed translations of a Rb condensate, and image the results in the two directions. By comparing the slopes of the two, we get the wanted magnification.

The calibration of the frontal imaging is made by acquiring the ballistic fall path of a Rb BEC. We then fit the position as a function of time with a second degree polynomial, and compare the second degree term (divided by 2) with the standard acceleration of gravity [220]; we obtain a pixel size in object space of $3.8\ \mu\text{m}$. This value agrees with previous calibrations of the pixel size done in the same way.

We then proceed to move the condensate in the vacuum chamber by using the compensation coils. We know that, in order to move the condensate on a line perpendicular to the dimple beam, and lying on the horizontal plane, the current in the compensation coils named x and y have to be changed by the same quantity, but with opposite signs [221]. We move the coils with current magnitudes varying from 80 mA to 200 mA. For each current value, we acquire the position of the centre of mass of the condensate for both the vertical and the horizontal imaging. The positions of the centres of mass are then fitted, as a function of the coil current, with a line.

In Figure 5.6 we can see the results of this calibration. The slope for the frontal imaging is $361\ \text{px}/\text{A} \pm 2\ \text{px}/\text{A}$, while that of the vertical imaging is $914\ \text{px}/\text{A} \pm 1\ \text{px}/\text{A}$, giving a relative magnification of 2.53 ± 0.02 . This means that, for a pixel size in the object plane of the

^{||}The uncertainties are taken from the covariance matrix calculated from the fit Hessian; the σ on each pixel value is specified as the square root of the pixel intensity, supposing a counting statistic.

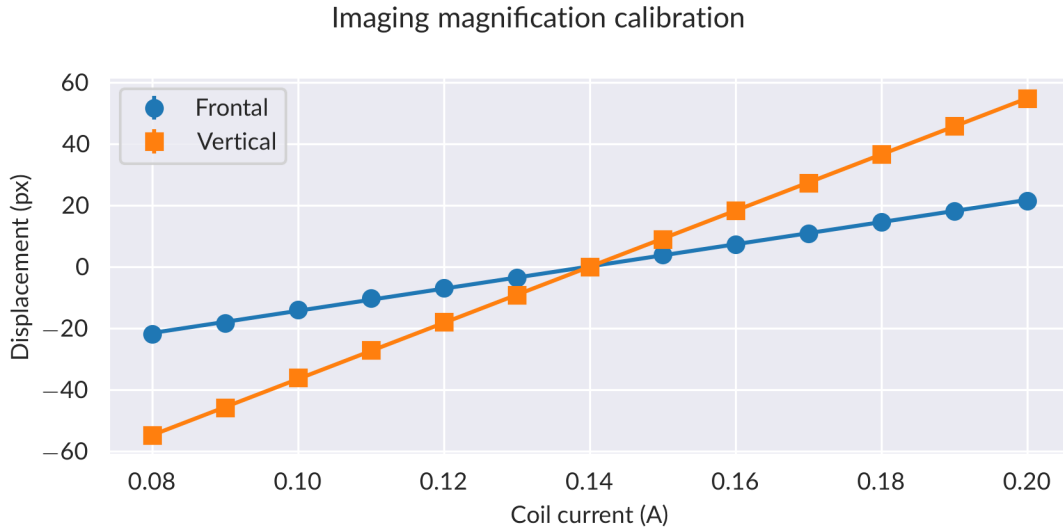


Figure 5.6.: Displacement of the centre of mass of the condensate, as a function of the current in the compensation coils. The blue circles represent the data acquired from the frontal imaging, and the orange circles the data acquired with the vertical imaging; the solid lines represent the fitted calibrations. The zero of the displacement is arbitrarily chosen at the midpoint of the current excursion; this does not influence the analysis, which is done by comparing the slopes only.

frontal imaging of $3.8 \mu\text{m}$, we have a pixel size in the object plane of the vertical imaging of $1.50 \mu\text{m} \pm 0.01 \mu\text{m}$.

Given that, as mentioned before, the camera used for the high-resolution imaging has a pixel size of $16 \mu\text{m}$ [215], we have an effective magnification of 10.7, which is compatible with the design value of 10.

5.4. High-field imaging

Given that we want to image the dynamics of the mixture, we have to do the imaging in the closest possible conditions to those in which the dynamics happens, without any possible disturbance that may be induced by the switching off of the fields. This includes the switching off of the magnetic fields, and implies the necessity of doing imaging at magnetic fields of around 70 G, whereas usually our TOF imaging is done at 0 G.

The first step is finding one or more suitable transitions on which to probe the condensates. We start by finding the energy difference between the ground state $^2S_{1/2}$, $F = 1$, $m_F = 1$, and the excited manifold $^2P_{3/2}$; this can be done by finding the eigenvalues of the Zeeman Hamiltonian

$$\mathbf{H} = \mathbf{H}_{\text{hfs}} - \boldsymbol{\mu} \cdot \mathbf{B}, \quad (5.36)$$

The quantization axis is chosen along the z axis (which would correspond to the symmetry axis of the Feshbach coils in the apparatus); as such, the symmetry is cylindrical along this

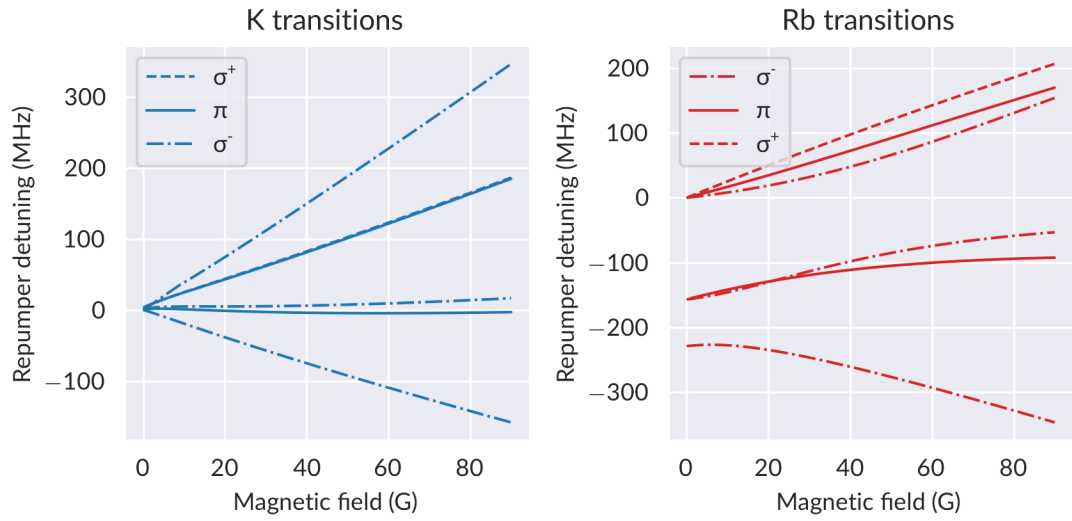


Figure 5.7.: Allowed transitions from the $F = 1, m_F = 1$ $^2S_{1/2}$ to the $^2P_{3/2}$ for ^{41}K and ^{87}Rb , as a function of the external magnetic field. The line styles represent the polarization of the transition, assuming the probe beam to be along the quantization axis.

axis, and the Hamiltonian commutes with the z component of F :

$$[\mathbf{H}, F_z] = 0. \quad (5.37)$$

The Hamiltonian is thus block-diagonal, with each block corresponding to an eigenvalue M of F_z . While F is not a good quantum number for every field strength, we will use it to label the transitions, understanding that we are referring to the level which is adiabatically connected to the corresponding state in the low-field limit. The strength of the transition, instead, is given by the square modulus of the matrix elements, in the same basis, of the optical dipole Hamiltonian

$$\mathbf{H}_{\text{opt}} = -\mathbf{d} \cdot \mathbf{E}. \quad (5.38)$$

A more detailed treatment of these calculations, along with the numerical codes employed, is found in Appendix A.

The detunings from the repumper transition, as a function of the magnetic field, are shown in Figure 5.7; the strengths of the corresponding transitions are shown in Figure 5.8. For K, there are three conveniently located transitions: a π -polarized transition, which is almost constant with magnetic field, a σ^- transition roughly 10 MHz above, and a σ^+ transition 130 MHz below; due to the probe beam being along the polarization axis, the π transition is not visible. For rubidium, instead, the only reachable transitions are the σ^- and π that start from the $F' = 1$ state; as with K, the π transition cannot be used.

For K, we searched for the transitions by imaging the K condensate alone at 0 G, for reference, and at 67.2 G, looking for peaks of the detected optical density. The $F' = 0$ transition strength impedes a good imaging of the condensate clouds at high densities: the dimensions

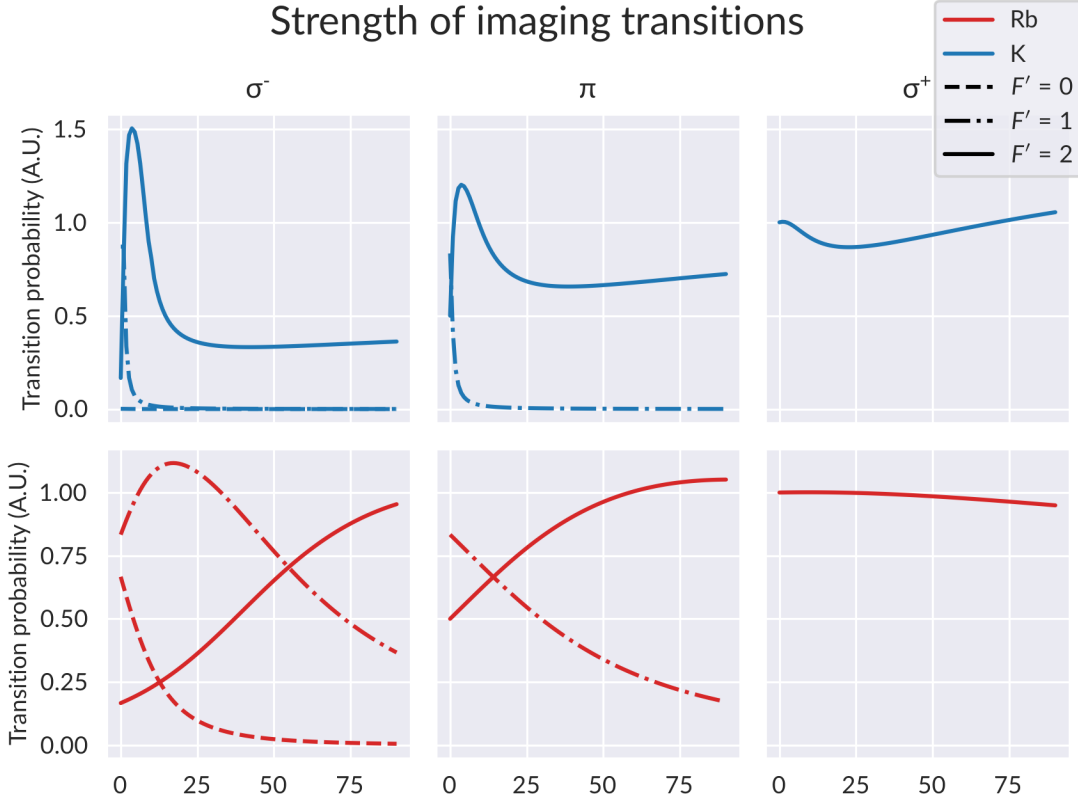


Figure 5.8.: Relative strengths for the imaging transitions, which are optical dipole transitions starting from the hyperfine ground state $F = 1, m_F = 1$, as a function of the external magnetic field. The probabilities are normalized in order to have strength 1 for the σ^+ , $F' = 2$ transition.

of this condensate at 67.2 G are higher than those of condensates of the same species imaged at 0 G: fitting with a Gaussian, the former had a $\bar{\sigma} = \sqrt{\sigma_x \sigma_y}$ of approximately $13 \mu\text{m}$, while the latter of $8 \mu\text{m}$; we also found that decreasing the imaging pulse length, from $151 \mu\text{s}$ to $51 \mu\text{s}$, does not significantly change the sigmas. Therefore, we turned to the weaker $F' = 1 \sigma^-$ transition. Here, aided by a further reduction of the imaging pulse to $30 \mu\text{s}$, we were able to see a $\bar{\sigma}$ of around $5 \mu\text{m}$ at 67.2 G.

Due to the fact that Rb imaging is usually perturbed by the K imaging being done before, and by the fact that between the two images a minimum of 2 ms has to pass in order for the Rb condensate to fall into the focal plane of the objective, we are able to image the Rb atoms at zero field, and we are therefore not concerned with the frequency of the transition because, as we can see in Figure 5.7, there are three degenerate transitions at that field strength. In order to avoid saturation effects, as seen with K, we do only a repumper pulse of $11 \mu\text{s}$.

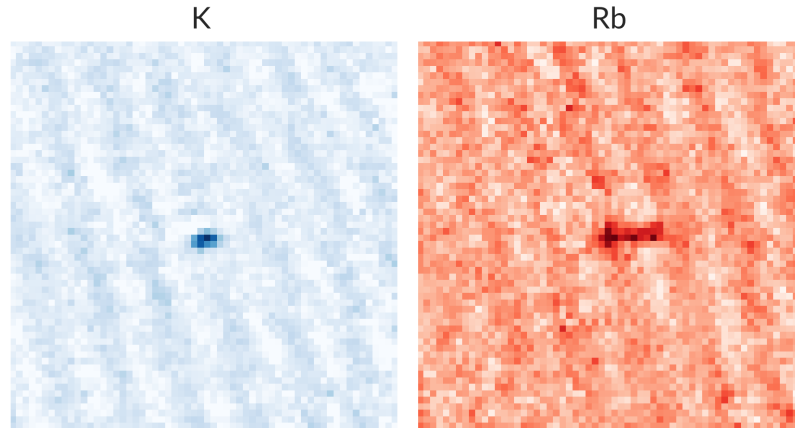


Figure 5.9.: High-resolution absorption image of the mixture in the beyond-mean-field collapse regime. The interspecies scattering length is $a_{12} = -85a_0$, and the two condensates have approximately the same number of atoms ($\approx 40^3$). The K condensate is imaged in situ at 67 G, while the Rb condensate is imaged after 2 ms TOF, with the field turned off.

5.5. In situ images of a Bose-Bose mixture

We proceed to image the mixture with the high-resolution setup developed thus far. We produce the double condensate in the $F = 1, m_F = 1$ state, using the procedure explained in Chapter 3, and we tune the interspecies interactions to $-85a_0$, well below the mean-field-collapse threshold, and aim to have an approximately balanced number of atoms, $N_K \approx N_{Rb} \approx 40 \times 10^3$. The trap frequencies are $2\pi \times (65, 190, 179)$ Hz for K and $2\pi \times (48, 138, 131)$ Hz for Rb, in the $x, y,$ and z directions respectively.

The image of the double BEC can be seen in Figure 5.9, where the K is imaged in situ at 67 G, and the Rb after 2 ms TOF, at zero magnetic field, and using only the repumper light. The image is then subjected to a noise removal algorithm, which is reported briefly in Appendix B. We can check that the resolution is as expected by fitting the image of the K cloud with a Gaussian, and comparing it with the numerically simulated distribution. We find that the transversal and longitudinal sigmas from the experimental image are, respectively, $\sigma_t = 1.2 \mu\text{m}$ and $\sigma_l = 2.2 \mu\text{m}$, which are in good agreement with the predicted values $\sigma_t = 1 \mu\text{m}$ and $\sigma_l = 2 \mu\text{m}$ [222].

After this confirmation that the imaging system is in good order and performs as predicted, we proceed to add a further telescope after the first one; the two lenses of which it is composed have focal length 100 mm and 200 mm, in order to have an additional magnification factor of 2. We calibrate the effective magnification as detailed above, obtaining a pixel size of $0.8 \mu\text{m}$ in object space.

Finally, we prepare the mixture in a quantum droplet state, and image it. The droplet preparation procedure starts with two non interacting condensates, whose trap frequencies are analogous to those used for the attractive mixture image (Figure 5.9), and with atom numbers of the order of 3×10^4 for K and 1×10^5 for Rb. Then, we linearly ramp the Feshbach field,

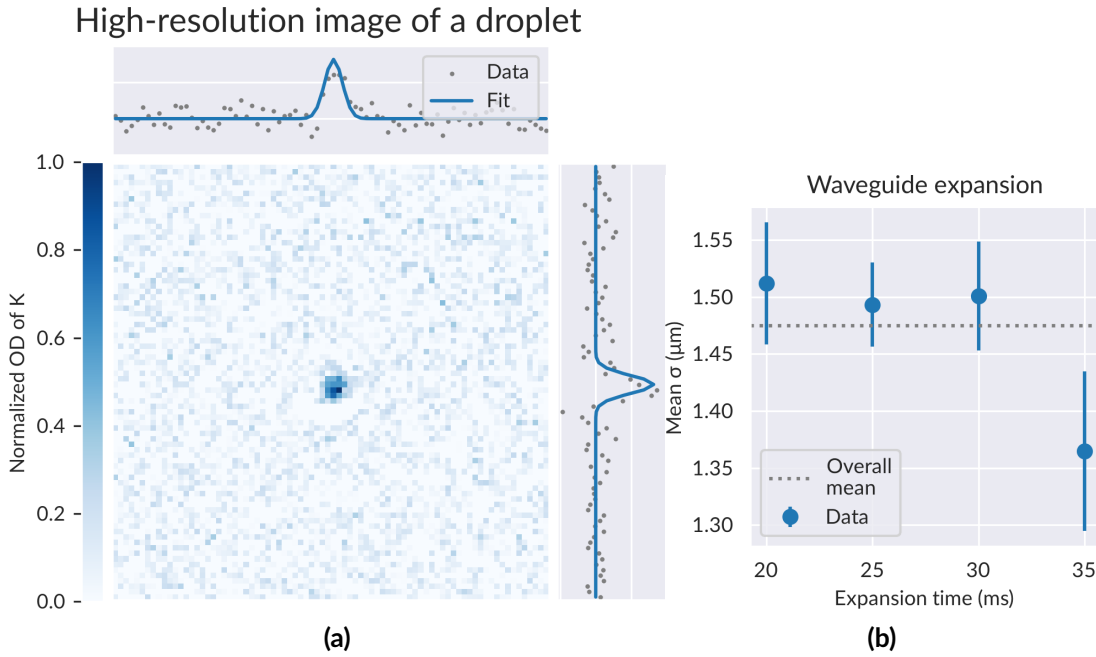


Figure 5.10.: High-resolution image of a quantum droplet (a), and geometric average of droplet σ during waveguide evolution (b). The droplet is imaged after 30 ms of waveguide evolution; in the marginal axes we can see the data of an image slice along the Gaussian centre (grey dots), along with a slice of the corresponding Gaussian fit (blue lines). These states do not expand during their waveguide evolution, as can be seen in (b), where we have the blue dots as the average of the geometric mean of σ_x and σ_y for various realizations of quantum droplets; a dotted grey line represents the overall mean size.

bringing the scattering length a_{12} down to $-66 a_0$ in 20 ms, and then further to $-89 a_0$ in 10 ms. Afterwards, we ramp down the dimple beam to 0 W in 10 ms, reaching trap frequencies of $2\pi \times (2, 116, 153)$ Hz for K and $2\pi \times (1, 85, 112)$ Hz for Rb. From there, we let the droplet expand in the waveguide for a variable time between 20 ms and 35 ms, and then we image the condensate with the same pulse sequence as was used for obtaining Figure 5.9.

We can see an image of the K condensate in a localized state, after 30 ms of waveguide expansion, in Figure 5.10a; fitting this image with a Gaussian, we obtain a $\sigma_x = 1.2 \mu\text{m}$ and $\sigma_y = 1.3 \mu\text{m}$. It is worth noting that the state is self bound, as there is no size change during the waveguide evolution up to 35 ms, where the droplet begins to vanish, probably because of three-body losses, as can be seen in Figure 5.10b. While this is not the final step in the characterization of a droplet state in the waveguide, as an expansion sequence would have to be taken for various scattering lengths to ensure the proper dependency of the condensate size on the interspecies interactions, it is nevertheless possible to conclude that this imaging system is adequate in imaging droplet-sized objects.

Characterization of a Digital Micromirror Device

In this Chapter, I will summarize the work done during my internship, from January to April 2023, in the Quantum Gases Experiment group of Prof. Leticia Tarruell at ICFO - The Institute of Photonic Sciences. The aim of this period was to characterize a Digital Micromirror Device (DMD), which is a device capable of modulating light, in order to create an arbitrary intensity profile; moreover, this intensity profile can be changed in real time, allowing the implementation of dynamical potentials. Due to its high flexibility, generation of atomic optical potentials with a DMD is rapidly gaining traction within the quantum gases community.

More specifically, I evaluated the characteristics of a Vialux V-9501 DMD, and its suitability for the ^{39}K experiment, where it would be used for the aforementioned generation of arbitrary optical potentials.

The chapter is structured as follows: Section 6.1 is devoted to the explanation of the optical setup of the imaging apparatus in which the DMD has been used. We will then pass on in Section 6.2 to the procedures used for calibration of the DMD image, and the compensation of the image defects. Finally, in Section 6.3, I will give an account of some of the more relevant performance measures of the DMD.

6.1. DMD Setup

In Figure 6.1 the DMD setup is shown. It is composed of two main parts: an illumination assembly, before the DMD, and an imaging assembly after it.

The illumination assembly sources the light from a 767 nm ECDL (not shown in the figure), which is then injected into an optical fibre and transported to the output coupler shown in figure. The output polarization is cleaned by a combination of a half-wave plate and a polarizing beam splitter. A small fraction is then diverted by a beam sampler and directed to a photodiode; the signal of this photodiode is connected to a PID controller, whose output is in turn connected to the current modulation input of the laser controller: in this way, the current

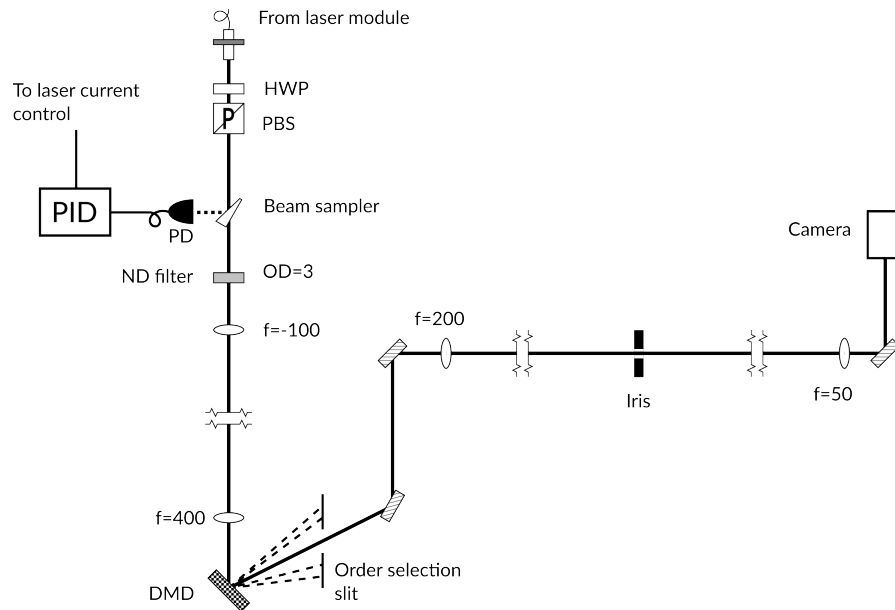


Figure 6.1.: Optical scheme of the DMD setup. The illumination is provided by a laser module (not shown); the diode current of the laser is modulated by the output of the PID controller to ensure a constant output power.

can be slightly adjusted around its nominal set point to ensure a constant power output for the illumination assembly. The output power with this stabilization was (measuring after the coupler) of around 19 mW. Afterwards, the beam goes onto a neutral density (ND) filter, with an OD of 3: this was deemed necessary as the unattenuated beam is adequate for aligning the system with the aid of an IR visor, but would saturate the imaging camera,^{*} even at its lowest exposure time. Afterwards, the beam is magnified by a factor of 4 using a telescope; the beam is big enough to cover a good fraction of the DMD active area, but, at the same time, the amount of light spilling out of this area is minimized.

The laser beam then encounters the DMD,[†] which is a chip made of a square array of small (7.56 μm) mirrors. Each of these mirror is hinged about its diagonal, and can be oriented in one of two positions, with an angle of, respectively, 12° or -12° with respect to the chip plane, enabling thus a selective reflection of an incoming beam. By placing the outgoing optical path onto one of these two directions, we can shape the beam with arbitrary intensity profiles; the only limit to this is the discrete spatial distribution and state (on or off) of the mirrors.

Being composed of multiple mirrors at an angle, the DMD surface acts as a diffraction grating, it is therefore necessary to orient the DMD in a specific direction, with respect to the incoming beam, to achieve a good diffraction efficiency. We see an illustration of this in Figure 6.2a, where we also define the angles that will be used in the following paragraph: we use θ_i and θ_r to describe the angle, respectively, of the incoming and reflected ray with respect

^{*}FLIR Blackfly S BFS-U3-16S2M-CS USB.

[†]The chip on the tested device is a DLP9500 from Texas Instruments [223].

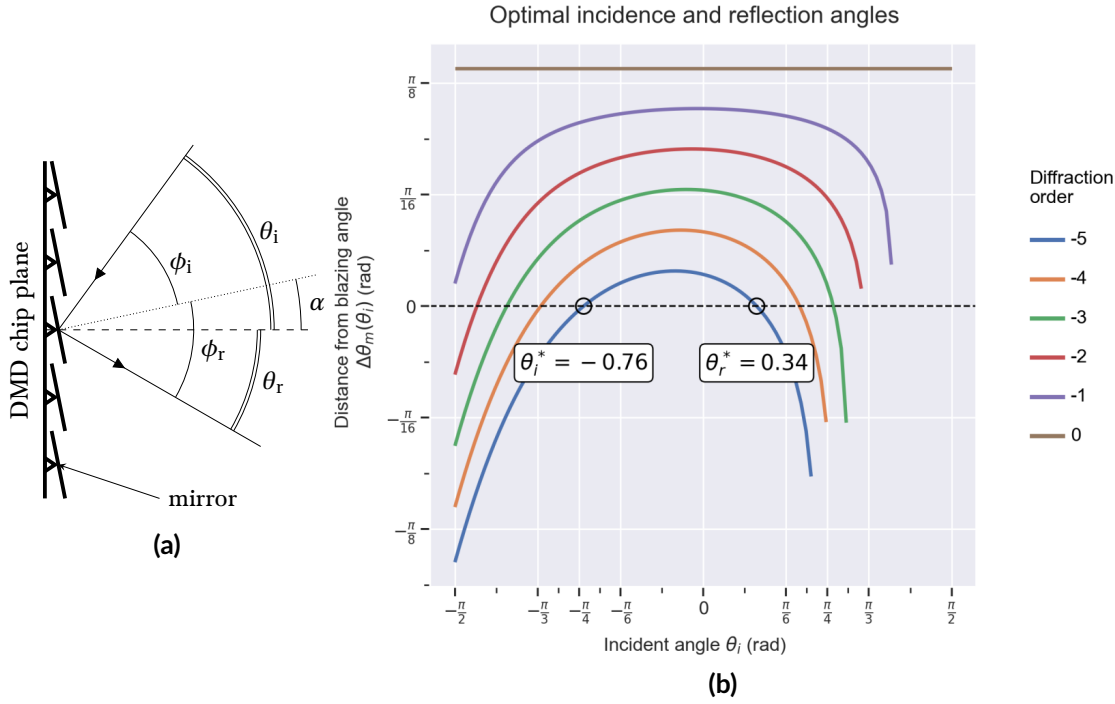


Figure 6.2.: Angle definitions (a) and optimal orientation (b) for the DMD orientation. In (a), the mirrors are shown at $\alpha = 12^\circ$ from the DMD plane, meaning that they are in the on direction; in the off direction, they would sit at -12° . In (b), the two circlets highlight the optimal incident angle θ_i^* and its corresponding reflection angle θ_r^* .

to the normal to the DMD surface, and ϕ_i and ϕ_r to denote those same angles with respect to the mirror normal. The maximum of the diffraction efficiency is achieved, for the diffraction order m , when the diffracted angle is equal to the reflected angle [224], satisfying the blazing condition:

$$\phi_r = \phi_m = -\phi_i, \quad (6.1)$$

which, translated to the DMD plane, means that

$$\theta_r = \theta_m = -\theta_i - 2\alpha. \quad (6.2)$$

The grating equation gives an expression for θ_m :

$$\sin(\theta_m) + \sin(\theta_i) = \frac{m\lambda}{a}, \quad (6.3)$$

where λ is the wavelength, and a is the pitch of the grating (i.e. the mirror diagonal, $10.7 \mu\text{m}$); this equation can be inverted, giving

$$\theta_m = \arcsin\left(\sin(\theta_i) - \frac{m\lambda}{a}\right), \quad (6.4)$$

which, in turn, can be recast as a constraint equation for θ_i :

$$\theta_i + 2\alpha + \arcsin\left(\sin(\theta_i) - \frac{m\lambda}{a}\right) = 0. \quad (6.5)$$

Equation (6.5) can be solved numerically for $m = -1, \dots, 5$, the solutions are shown in Figure 6.2b. We see that, for increasing $|m|$, the two angles are closer both to each other, and to the DMD normal. We select the -5 diffraction order, to minimize the reflection angle and thus defocusing aberrations: for this order, the optimal angles are $\theta_i^* = 44^\circ$ and $\theta_i = 19^\circ$. The DMD is mounted on a goniometric stage, which enables precise rotation; by setting the rotation to the optimal angle, and then adding a slight rotation, we achieve the blazing condition. In this configuration, the total reflection efficiency in the selected order is 30%.

The imaging assembly comes after the DMD, and its purpose is to image the density distribution into the camera—or, in the final configuration, on the atomic plane. First, a diffraction order is selected using a slit; then, after two steering mirrors, the beam is demagnified by a telescope: this telescope is formed by two achromatic lenses, the first with a focal length of 200 mm, and the second an aspheric lens with a focal length 50 mm, which is of the same type as the one that will be eventually used in the apparatus, for a demagnification factor of 4. At the focal point of the first lens, there is an iris, whose aperture can be modified to filter the high frequencies of the projected image. Finally, the picture is collected by a camera, for subsequent analysis.

6.2. Image calibration and optimization

After projection, the final image is rarely as intended. Completely counteracting these defects is normally done with holographic techniques, in which the Fourier transform of the desired pattern is projected, and the imaging is done on the conjugate Fourier plane of the DMD with the aid of an additional lens [225]. There are, however, other techniques, more readily implemented with our direct imaging setup [226, 227], which we will implement here: we will show a geometric calibration technique, to counteract rotations and magnifications, and an intensity optimization technique, to counteract the varying intensity of the illumination beam.

6.2.1. Geometric calibration

The DMD mirrors hinge about one of their diagonals: because of this, in order to have the illumination beam and the projection beam aligned on the same plane, the DMD needs to be rotated by 45° . While this bears no prejudice on the optical performance of the system, every image projected with the DMD will be rotated by the same amount. Another, and more serious, defect introduced by the imaging setup after is the stretching of the image: this is due to both an intrinsic component, due to the focal ratio of our setup, and to aberrations: those two introduce, respectively, a common magnification to both axes belonging to the object plane, and a differential amount for the two.[‡] Another critical unwanted transformation is

[‡]Our setup was intended for test purposes, hence the placement of the camera after the first telescope. A final setup for mounting on the experiment would have greater demagnification, and, if present, another telescope after

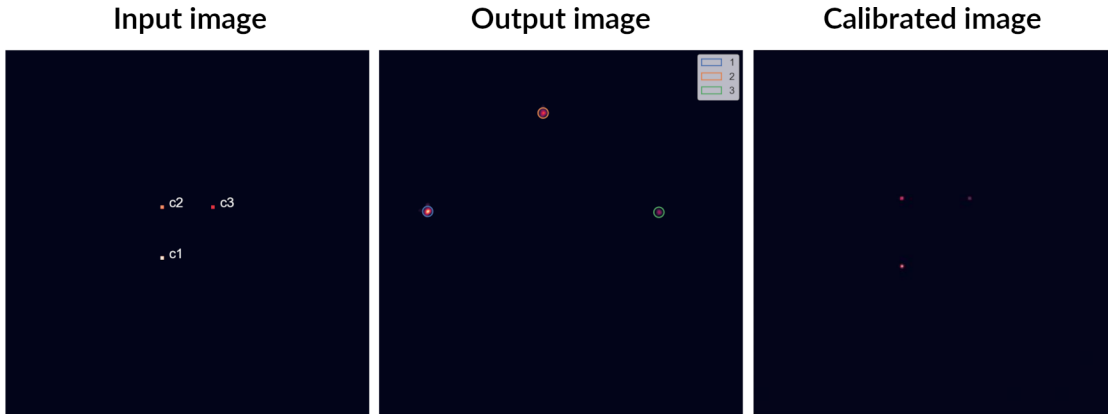


Figure 6.3.: Geometric calibration of the DMD. The first image on the left is the projected image, with the three alignment dots labeled. The second is the uncalibrated output image, where the three alignment dots have been detected and classified. On the right we have a picture of the input image, after passing through the calibration procedure.

shearing, where one of the image axes is rotated with respect to the other. Finally, the image centre will, in general, be off-centred with respect to the centre of the camera.

The general combination of a translation, a shear, and a (generally inhomogeneous) magnification is called an affine transformation. In two dimensions, an affine transformation of a point \mathbf{x} can be represented by a matrix

$$\begin{pmatrix} \mathbf{x}' \\ 1 \end{pmatrix} = \begin{pmatrix} \mathbf{A} & \mathbf{b} \\ \mathbf{0} & 1 \end{pmatrix} \begin{pmatrix} \mathbf{x} \\ 1 \end{pmatrix}, \quad (6.6)$$

where \mathbf{b} is the translation vector, and \mathbf{A} is a 2×2 matrix representing the other transformations. We suppose that our system will impart an affine transformation \mathbf{M} on the projected image; therefore, transforming the image with \mathbf{M}^{-1} prior to the projection will counteract those defects, giving as output our desired image.

In order to fully specify \mathbf{M} , we need the image through the transformation of three distinct points. For this purpose, we synthesize an image with three dots in an inverted "L" shape, with decreasing intensities. Then, we acquire the image of those three dots, and find the centres of the dots using the DAOFIND algorithm [228]; then each dot is paired to its corresponding input by matching the relative intensities. Having the coordinates, the affine transform is found using the `getAffineTransform` function from the OpenCV library [229]: this outputs the $(\mathbf{A}|\mathbf{b})$ matrix, which can subsequently be inverted and used to transform the input image using either the `warpAffine` function from OpenCV, or by manually implementing (6.6). We can see the three aforementioned steps in Figure 6.3, in which we show the input image, the uncalibrated output, with the dots classified, and the same image after calibration.

the atomic plane for imaging the projected intensity pattern. As such, the common magnification component can be virtually eliminated, leaving for correction just the differential amount.

6.2.2. PI optimization

After the geometric calibration, a second correction can be done to the image, compensating for the varying intensity of the illumination beam. For a same input value of, say, 50% intensity, the actual output value could be higher or lower, depending on illumination intensity. To counteract this, provided that the target intensity is lower, in the image region, than the lowest illumination intensity, is to reduce the input intensity where the illumination is brighter.

This is achieved using a PID-like scheme. Suppose we have a target image \mathbf{R} : the first step for this procedure is to set the projection image $\mathbf{X}_0 = \mathbf{R}$. The difference between the output \mathbf{Y}_0 and the target is the error matrix: $\mathbf{E}_0 = \mathbf{R} - \mathbf{Y}_0$; we then calculate the next input using the relations

$$\mathbf{X}_{j+1} = \mathbf{X}_j + \mathbf{U}_{j+1} \quad (6.7)$$

$$\mathbf{U}_{j+1} = k_P \mathbf{E}_j + k_I \sum_{l=0}^j \mathbf{E}_l, \quad (6.8)$$

where k_P and k_I are real parameters called, respectively, the proportional and integral gains of the PID. Afterwards, the procedure can be iterated, until the compensated input image converges.

For a good performance of this procedure, we need to find the optimal values for k_P and k_I , which will result in the lowest possible RMS error after a set number of iterations. We use an optimization routine based on the differential evolution algorithm [230], which is a global optimization algorithm; the function to be optimized is the RMS error of the image of a square with a side of 50 μm after ten PID iterations. The obtained gains are then saved for later use.

This image optimization can achieve a 50% to 75% reduction of the RMS value of \mathbf{E} (i.e. the RMS error) in less than five iterations.

6.3. Characterization

6.3.1. Timing properties

In order to measure the timing properties of the DMD, we used a modified setup, where the iris in Figure 6.1 was replaced with a photodiode: in this way, we were able to efficiently collect all of the DMD reflected intensity, which was focalized in a point on the photodiode chip. The signal can then be visualized and analyzed using an oscilloscope.

First, we measured the frame rate by projecting an alternating sequence of black and white images, which correspond to all mirrors, respectively, in the on or off position. The maximum frame rate of 25 kHz was found to be slightly higher than the nominal frame rate of 24 kHz. We found that the maximum difference between the real and the nominal frame rate was, in the worst case, 10%; while this could be a problem if higher precision is required, such as in the case of the generation of a dynamic potential, for this board the frame advancement can be controlled with an external trigger[231].

Then, we measured the dark time: during projection, there is a transition time between two images, in which the mirrors are held neither in the on, nor in the off position, but in an

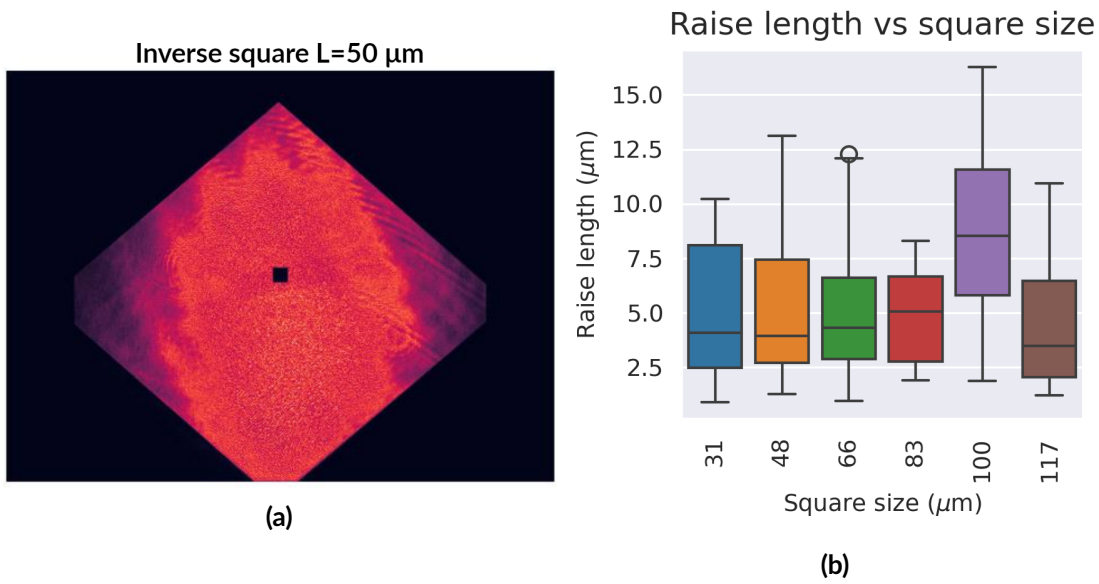


Figure 6.4.: Inverted square, with $L = 50 \mu\text{m}$ (a), and effect of the square size on the distribution of raise lengths (b), as a box plot. In a box plot, the middle line of each box represents the distribution median, and its limits represent the interquartile ranges. The lines extending above and below represent the range of points within 1.5 interquartile ranges; points outside this region are classified as outliers, and displayed singularly.

intermediate parking direction, parallel to the DMD plane (i.e. with $\alpha = 0^\circ$). We projected a sequence of white images, with all the mirrors in the on position; the time with a low signal between each couple of images is the dark time. While the nominal value for this board is $40 \mu\text{s}$, we measured an effective dark time of $17 \mu\text{s} \pm 2 \mu\text{s}$. If static or slowly evolving patterns are needed, this dark time could be ignored; nevertheless, the device can be operated in an uninterrupted mode [231], in which the dark time is reduced to zero. The only disadvantage of the uninterrupted mode is the impossibility of obtaining grey tones on a single pixel by modulating its duty cycle, but this modulation could actually be detrimental in a cold atoms experiment, where noise in the potential could heat the atomic sample: therefore, there are no net drawbacks to the employment of the uninterrupted mode.

6.3.2. Sharpness

Another important feature of the imaging system is the sharpness of the image, which we define as the transition length of the optical system, given a step-type input

$$u(x) = \begin{cases} I_0 & \text{if } x \geq 0 \\ 0 & \text{otherwise} \end{cases}; \quad (6.9)$$

this transition length is dictated by the optical transfer function. It is also worth noting that, while in the case of incoherent illumination we expect an image of a step-type object as a

smoothed out version of u , for coherent illumination we have a sinusoidal oscillation in the bright part [213].

In order to measure sharpness, images of a square

$$s(x, y) = \begin{cases} I_0 & \text{if } 0 \leq |x| \leq L/2 \wedge 0 \leq |y| \leq L/2 \\ 0 & \text{otherwise} \end{cases} \quad (6.10)$$

and of an inverted square $q(x, y) = I_0 - s(x, y)$ were projected, with I_0 set to half the maximum illumination intensity (acquired with a white image), and L ranging from 31.1 μm to 117.4 μm . This was done to evaluate if the sharpness is lower for smaller squares. The images, after being acquired by the camera, were analyzed by finding the width of the edges, which is defined as the distance between the last pixel at 90% I_0 and the first at 10% I_0 .[§] A box plot of the distributions can be found in Figure 6.4b: as we can see from the image, we found no significant trends in the data. Combining all data, we get a mean edge width of 5.5 μm , with a standard deviation of 3.6 μm ; the distribution has a median of 4.6 μm and an interquartile range of 5.2 μm .

6.3.3. Residual light

In the case of a repulsive potential, the amount of residual light in the dark area is a relevant characteristic of the system. To characterize it, we acquire the distribution of the intensity in the dark area of the inverted squares acquired in the previous subsection; from the nominal dark area we subtract a region of 3 px around the edge centre (in its steep direction), to exclude the roughness due to the square border. This data is plotted in Figure 6.5a; we can see that, after the smallest square, for which the residual light is visibly higher, for the others we have a slightly decreasing function of square size.

As we are interested in lowering this residual light, we tried to see if lower values of image intensity would reduce the amount of light scattered into the dark region. For this purpose, we projected a square with $L=75 \mu\text{m}$ (where the effect of the square size on the residual light begins to taper off) at various image intensities, from 20 to 180 on a maximum of 255, and measured the residual light intensity as done before. The data is shown in Figure 6.5b: there, we see that, for lower intensities, the amount of light scattered into the dark region, peak-to-peak, is half the peak-to-peak value of the light scattered for higher intensities (80 or more). We can then say that, in order to reduce the amount of scattered light by a factor of two, we have to reduce the intensity of the image by a factor of four; this trade-off between power and roughness has to be evaluated for each specific situation.

6.3.4. Filtering

In the setup, an iris is put in the focal plane of the first imaging telescope lens to give the ability of filtering the high-frequency components of the image. This filters the corresponding noise in the image, but, at the same time, lowers sharpness: our aim here is to find the response of those two quantities for various diameters of the iris.

[§]In this definition, we assume that the edge direction is from the bright zone to the dark zone.

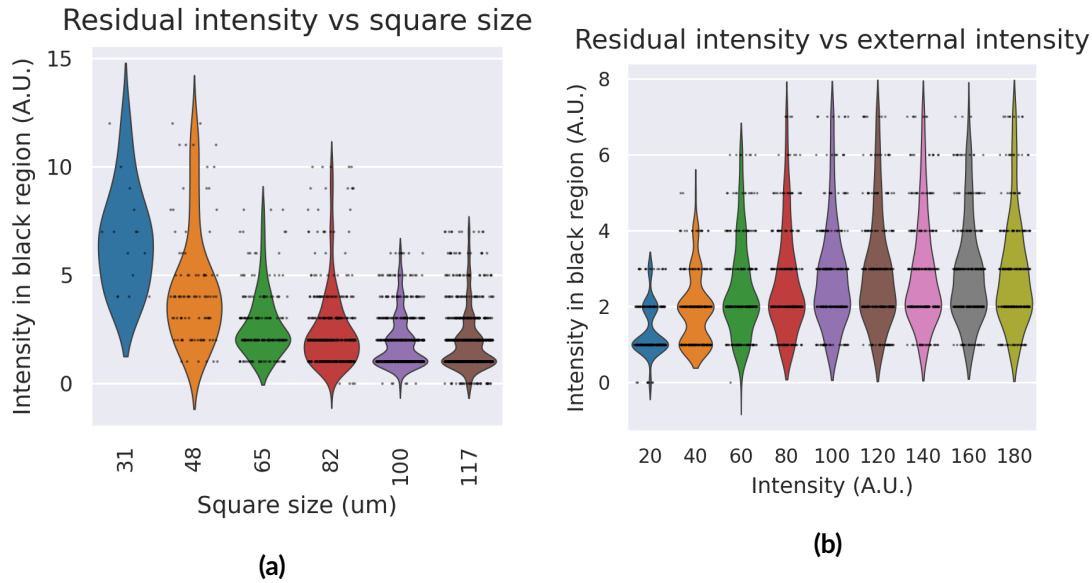


Figure 6.5.: Violin plots of residual light intensities for (a) different square sizes, and (b) for different illumination intensities. The width of the area represent the probability density of the observed distribution, estimated with the kernel density estimation (KDE) technique [232, 233]. Superimposed on this, we also show each observation as a translucent black dot (i.e., blacker areas correspond to more observation where they would otherwise overlap).[¶] It is worth noting the low number of observations for $L = 31 \mu\text{m}$, which would necessitate some caution in reaching conclusions based on that data point alone; nevertheless, it can be seen that the trend of increasing intensity for smaller squares is seen in all of the other data points.

In order to do so, a square with a side of $500 \mu\text{m}$ is projected, and we measure both the RMS error of the output image, with respect to the target image, and the edge width, for various iris diameters. The values of these two functions (with the edge width reported as the median value of its distribution) are shown Figure 6.6. For the RMS error, we see that, as expected, it decreases for smaller diameters; if we define a cutoff as the input (iris diameter) value that causes the signal (RMS error) to fall to 0.25 of its amplitude (i.e. the range of the RMS error), we see that the cutoff diameter is 4.13 mm, with a cutoff error of 2.33. Also as expected, for the median edge width we have the inverse behaviour, with image sharpness falling for smaller apertures; if we define a cutoff in the same way for this function, we find a cutoff diameter of 2.90 mm, with a corresponding median edge width of $7.45 \mu\text{m}$.

We notice therefore the same kind of sharpness-error trade-off that was present in the sharpness data. Also in this case, the exact amount to which one side of the trade-off is to be favoured will be dictated by the specificity of the problem at hand.

6. Characterization of a Digital Micromirror Device

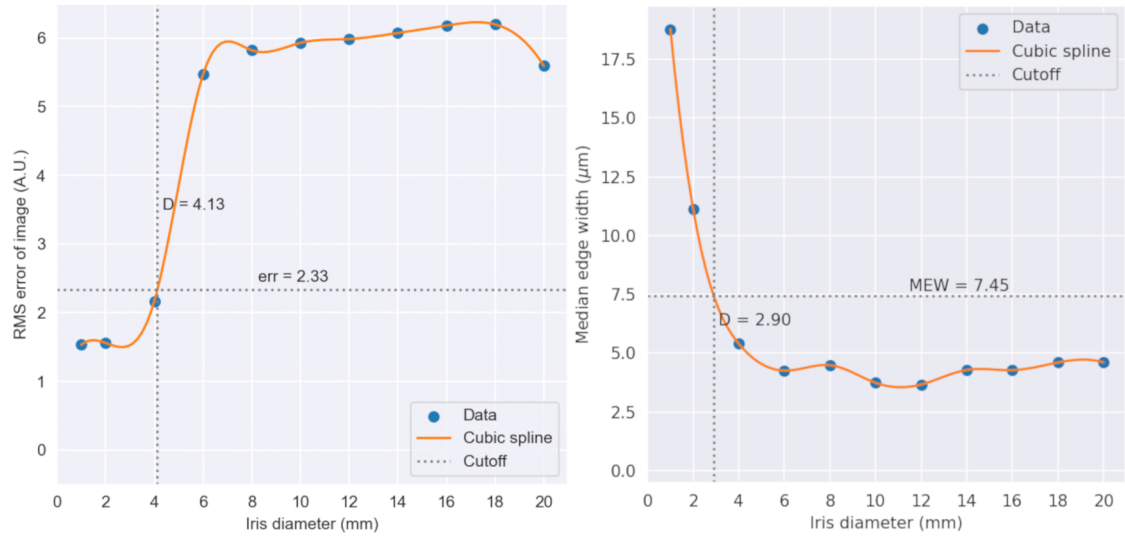


Figure 6.6.: Effect of filtering on a square image. In each image, the data points taken are represented by blue dots; these data points are interpolated by a cubic spline, represented by the orange line. The grey dotted line highlights the value and the diameter of the cutoff point.

Conclusions and outlook

In this thesis, we report experimental investigations of the physics of Bose-Einstein condensate mixtures, with the aim of understanding the physics of multicomponent superfluids.

First, we demonstrated the preparation of a double Bose-Einstein condensate with tunable interspecies interactions, using a ^{41}K - ^{87}Rb mixture in its lowest hyperfine state. The cooling sequence was reworked and improved, and we obtained a reliable way of obtaining condensates in the $F = 2, m_F = 2$ state, with both species reaching orders of magnitude of 10^5 atoms in the condensate part. The hyperfine transfers were calibrated and characterized, leading to an improvement in their transfer efficiency, and in the stability of the procedure. The improved optical dipole trap, along with the magnetic trapping capabilities, makes it possible to manipulate the atomic sample with ease and accuracy, opening novel possibilities for experiments with this mixture.

Then, we showed the study of the dipole oscillations, a collective mode of the mixture. From a theoretical point of view, we have seen that this mode is characterized by a rigid translation of the centre of mass of the condensate, and that, while for a single condensate the effect of the interactions on the mode observables is null, for a mixture interspecies interactions change both frequency and amplitude of this oscillation. On the experimental side, we have devised a protocol for the excitation of this mode, and established the statistical analysis to be done to extract and discuss the quantities of interest, namely frequency and amplitude. We have then compared the results thus obtained with two models of coupled oscillation, concluding that, while semi-classical models have a good accuracy in the prediction of the in-phase mode, for the out-of-phase mode only numerical simulations of the Gross-Pitaevskii equation can give correct results: this is due to the actual violation of the rigid-translation hypothesis for the out-of-phase mode, which is indeed at the heart of the aforementioned semi-classical models.

We implemented an high-resolution imaging system, that makes this apparatus capable of in-situ probing of the double condensate. We looked at the design of the objective, and assessed its adequacy to the specifications, with a nominal resolution of approximately $1.3\ \mu\text{m}$. We designed a compensation scheme for the beam of the magneto-optical trap, which is necessary due to the position that the objective will have in the apparatus, and concluded that it meet its operational requirements. After mounting the objective in the apparatus, we calibrated the magnification, extracting a pixel size compatible with the expected value for the system. We calculated the transition frequencies at high fields, and selected, for K, those gentle enough not to perturb the sample during the probe pulse, resulting in an accurate measurement of the condensate size; for Rb, we decided to image the condensate at zero field,

during the differential time-of-flight expansion needed to bring the cloud into focus—which is different because of the chromatic aberration of the objective. Finally, we photographed the mixture in the mean-field-collapse regime, the most demanding in terms of resolution, and obtained values which are compatible with numerical simulations of the ground state.

We have seen the characterization of a Digital Micromirror device, to be used in the K experiment of the Quantum Gases Experiment group of Prof. Leticia Tarruell at ICFO. We have found the optimal configuration for reflective operation, and found a power efficiency of 30%. We implemented a calibration procedure to correct the macroscopic distortions due to the projection optics. We characterized the performance of the optical system, finding an edge resolution of $16.5 \mu\text{m} \pm 1.5 \mu\text{m}$; moreover, we characterize how the residual noise depends on the projected images.

The work done for this thesis could be useful for various developments in the exploration of multicomponent superfluids. We know from statistical mechanics that the features of a quantum degenerate system depend strongly on its underlying topology: therefore, the study of the mixture in a non-trivial topology could be a very interesting direction in which to move. For this purpose, we could look at the shell configuration: in the immiscible regime, a thin layer of K is predicted to be formed around a Rb core. Moreover, the physics of the miscible-to-immiscible phase transition has been hitherto unexplored in mixtures. On the other side, in the strongly attractive regime, states in the beyond-mean-field regime, such as droplets and Lee-Huang-Yang fluids, are, from an experimental point of view, relatively unexplored. Another goal would be the experimental observation of dissipationless drag, also known as the Andreev-Bashkin effect, which to this day remains elusive.

All those future possibilities are based on the results and the considerations exposed in the chapters before: it is therefore to be expected that, on these foundations, some ulterior brickwork in the edifice of physics could be laid.

Calculation of high-field imaging transitions

In this appendix, we will illustrate the calculation of the transition frequencies and amplitudes for the imaging transitions at arbitrary fields from 0 G to 100 G.

A.1. Transition frequencies

In order to calculate the imaging frequencies, we will have to calculate the change in energy, as a function of the magnetic field, for both the ground state $^2S_{1/2}$, in the $F = 1, m_F = 1$ state, and the $^2P_{3/2}$ excited states, for the relevant hyperfine components. These hyperfine levels can be found with the selection rules for electric dipole transitions [173]:

$$\Delta F = 0, \pm 1, F = 0 \leftrightarrow F' = 0, \quad (\text{A.1})$$

$$\Delta M = 0, \pm 1; \quad (\text{A.2})$$

given that we start from $F = 1, m_F = 1$, the allowed transitions are to the $F' = 0, 1, 2, m_F = 0, 1, 2$ states. This is ultimately achieved by diagonalizing the Hamiltonian (5.36)

$$H = H_{\text{hfs}} - \underbrace{\boldsymbol{\mu} \cdot \mathbf{B}}_{H_{\text{mag}}}. \quad (\text{A.3})$$

For the ground state, it is straightforward because, having $J = 1/2$, the Breit-Rabi formula applies (3.18). We restate it here for ease of consultation (for the case $I = 3/2$ relevant to our atomic species):

$$\Delta E(B, m) = -\frac{\Delta E_{\text{hfs}}}{8} + g_I m \mu_B B \pm \frac{\Delta E_{\text{hfs}}}{2} \sqrt{1 + mx + x^2}, \quad (\text{A.4})$$

where

$$x = \frac{(g_J - g_I) \mu_B B}{\Delta E_{\text{hfs}}}. \quad (\text{A.5})$$

Table A.1.: Hyperfine splittings of the $^2P_{3/2}$ for ^{41}K and ^{87}Rb [160].

F	$\Delta E_{\text{hfs}}/h$ (MHz)	
	Rb	K
0	0	0
1	72.22	0.1
2	229.17	3.5
3	495.82	16.9

The excited state needs a more detailed treatment. The hyperfine splittings of the $F = 3$ state, which constitute the diagonal of \mathbf{H}_{hfs} are shown in Table A.1. The projection quantum number M is a good quantum number for each field strength, as its corresponding operator commutes exactly with the Hamiltonian:

$$[\mathbf{H}, F_z] = 0; \quad (\text{A.6})$$

the total moment quantum number $F = \mathbf{I} + \mathbf{J}$, on the other hand, it is not: we will, nevertheless, calculate the states in the basis $|I, J, F, M\rangle$, understanding that the states with a certain high-field F will be those adiabatically connected to the low-field states with that same F .

Each sub-matrix of $\boldsymbol{\mu} \cdot \mathbf{B}$, with fixed M , has elements

$$\langle I, J, F_1, M | \mathbf{H}_{\text{mag}} | I, J, F_2, M \rangle, \quad (\text{A.7})$$

with $M \leq F_i \leq 3$. The expectation value has to be calculated by expressing the state in the $|L, S, I, m_L, m_S, m_I\rangle$ basis, which gives

$$\begin{aligned} & \langle I, J, F_1, M | \mathbf{H}_{\text{mag}} | I, J, F_2, M \rangle = \quad (\text{A.8}) \\ & = \mu_B B_z \sum_{m_S=-1/2}^{1/2} \sum_{m_L=a}^b \mathcal{C}(I, M - (m_L + m_S), J, m_L + m_S, F_1, M) \\ & \quad \times \mathcal{C}(I, M - (m_L + m_S), J, m_L + m_S, F_2, M) \\ & \quad \times \mathcal{C}(L, m_L, S, m_S, J, m_L + m_S)^2 \\ & \quad \times (m_L + g_S m_S + g_I (M - m_L - m_S)), \end{aligned}$$

where the summation limits

$$a = \max\{-I - m_S + M, -L\} \quad (\text{A.9})$$

$$b = \min\{I - m_S + M, L\}, \quad (\text{A.10})$$

and

$$\mathcal{C}(j_1, m_1, j_2, m_2, J, M) = \langle j_1, j_2, J, M | j_1, m_1, j_2, m_2 \rangle \quad (\text{A.11})$$

are the Clebsch-Gordan coefficients.

Table A.2.: C and C_3 coefficients for calculation of the magnetic part of the Zeeman Hamiltonian.

M	m_S	m_L	C	C_3
0	$-\frac{1}{2}$	-1	$\left(-\frac{1}{2}, \frac{3}{2\sqrt{5}}, \frac{1}{2}, \frac{1}{2\sqrt{5}}\right)$	1
		0	$\left(-\frac{1}{2}, -\frac{1}{2\sqrt{5}}, \frac{1}{2}, \frac{3}{2\sqrt{5}}\right)$	$\frac{2}{3}$
		1	$\left(\frac{1}{2}, -\frac{1}{2\sqrt{5}}, -\frac{1}{2}, \frac{3}{2\sqrt{5}}\right)$	$\frac{1}{3}$
	$\frac{1}{2}$	-1	$\left(-\frac{1}{2}, -\frac{1}{2\sqrt{5}}, \frac{1}{2}, \frac{3}{2\sqrt{5}}\right)$	$\frac{1}{3}$
		0	$\left(\frac{1}{2}, -\frac{1}{2\sqrt{5}}, -\frac{1}{2}, \frac{3}{2\sqrt{5}}\right)$	$\frac{2}{3}$
		1	$\left(-\frac{1}{2}, \frac{3}{2\sqrt{5}}, -\frac{1}{2}, \frac{1}{2\sqrt{5}}\right)$	1
1	$-\frac{1}{2}$	0	$\left(\sqrt{\frac{3}{10}}, \frac{1}{\sqrt{2}}, \frac{1}{\sqrt{5}}\right)$	$\frac{2}{3}$
		1	$\left(-\sqrt{\frac{2}{5}}, 0, \sqrt{\frac{2}{5}}\right)$	$\frac{1}{3}$
	$\frac{1}{2}$	-1	$\left(\sqrt{\frac{3}{10}}, \frac{1}{\sqrt{2}}, \frac{1}{\sqrt{5}}\right)$	$\frac{1}{3}$
		0	$\left(-\sqrt{\frac{2}{5}}, 0, \sqrt{\frac{3}{5}}\right)$	$\frac{2}{3}$
		1	$\left(\sqrt{\frac{3}{10}}, -\frac{1}{\sqrt{2}}, \frac{1}{\sqrt{5}}\right)$	1
2	$-\frac{1}{2}$	1	$\left(\frac{1}{\sqrt{2}}, \frac{1}{\sqrt{2}}\right)$	$\frac{1}{3}$
	$\frac{1}{2}$	0	$\left(\frac{1}{\sqrt{2}}, \frac{1}{\sqrt{2}}\right)$	$\frac{2}{3}$
		1	$\left(-\frac{1}{\sqrt{2}}, \frac{1}{\sqrt{2}}\right)$	1

We proceed to write the Hamiltonian by expressing, for each triplet of M, m_L, m_S , the needed coefficients as a vector

$$\mathbf{C}_i = (\mathcal{C}(I, M - (m_L + m_S), J, m_L + m_S, i, M), \dots) \quad i = M, \dots, 3 \quad (\text{A.12})$$

and a number

$$C_3 = \mathcal{C}(L, m_L, S, m_S, J, m_L + m_S). \quad (\text{A.13})$$

The values for these quantities are reported in Table A.2. The magnetic parts of the Hamiltonian can thus be written as:

$$\mathbf{H}_{\text{mag}} = \sum_{m_S=-1/2}^{1/2} \sum_{m_L=a}^b (\mathbf{C}^T \mathbf{C} C_3)_{(m_S, m_L, M)} \cdot (m_L + g_S m_S + g_I (M - m_L - m_S)). \quad (\text{A.14})$$

It is now possible to write the numeric codes that give the transition frequencies. We will use the Python programming language [234], using the Numpy [235] and Sympy [236] libraries.

The Breit-Rabi function is straightforward, given that we don't have to account for the $M = \pm(I + 1/2)$ states [160]:

A. Calculation of high-field imaging transitions

```
1 import numpy as np
2
3 muB = 1.399624624 # Bohr magneton, in MHz/G
4 gJ = 2.00233113 # Landé g-factor for GS
5 # nuclear g factors:
6 gIK = -7.790600e-5 # for K
7 gIRb = -9.951414e-4 # for Rb
8 # hyperfine GS splittings
9 DFK = 2 * 127.0069352 # for K, MHz
10 DFRb = 2 * 3.417341305452145e3 # for Rb, MHz
11
12 def brx(B: np.ndarray, gI: float, deltaE: float):
13     """Calculate x variable in Breit-Rabi formula"""
14     return (gJ - gI) * muB * B / deltaE
15
16 def br(B: np.ndarray, gI: float, deltaE: float):
17     """Calculate Breit-Rabi formula for F=1, m_F=1"""
18     xx = brx(B, gI, deltaE)
19     term1 = -deltaE / 8
20     term2 = -gI * muB * B
21     qterm = 1 + xx + np.square(xx)
22     term3 = deltaE / 2 * np.sqrt(qterm)
23     return term1 + term2 - term3
24
25 # define field for calculations
26 # 100 equidistant points from 0 G to 100 G
27 B = np.linspace(0, 100, 100)
28
29 # K ground state frequencies
30 gsK = br(B, gIK, DFK)
31
32 # Rb ground state frequencies
33 gsRb = br(B, gIRb, DFRb)
```

For the excited state, we first express the magnetic Hamiltonians obtained using equation (A.14), then we add the hyperfine splitting Hamiltonian, and, in the end, we diagonalize it for each value of B that we want to calculate. For example, for Rb we have:

```
1 import numpy as np
2 import sympy as sp
3
4 muB = 1.399624624 # Bohr magneton, in MHz/G
5
6 # Hyperfine splittings in MHz
```

```

7 Fhfs0 = 0
8 Fhfs1 = 72.22
9 Fhfs2 = Fhfs1 + 156.6
10 Fhfs3 = Fhfs2 + 266.65
11 # Hyperfine splitting Hamiltonian as a diagonal matrix
12 hhfs = np.diag([Fhfs0, Fhfs1, Fhfs2, Fhfs3])
13
14 # field intensity as a symbolic value
15 B = sp.symbols("B")
16
17 # magnetic part of the Hamiltonian
18 # block M = 0
19 hm0 = np.array([
20     [-1.49268, 0, 0],
21     [-1.49268, 0, -1.19414, 0],
22     [0, -1.19414, 0, -0.895608],
23     [0, 0, -0.895608, 0]
24 ]) * muB * B
25 # add the hyperfine splitting
26 hm0 += hhfs
27 # convert the symbolic expression in a computationally
28 # efficient form
29 hm0f = sp.lambdify(B, hm0)
30
31 # magnetic part of the Hamiltonian
32 # block M = 1
33 hm1 = np.array([
34     [0.666551, -1.03416, 0],
35     [-1.03416, 0.666551, -0.844387],
36     [0, -0.844387, 0.666551]
37 ]) * muB * B
38 # for M > 0, we select only the relevant hyperfine
39 # terms
40 hm1 += hhfs[1:]
41 hm1f = sp.lambdify(B, hm1)
42
43 # magnetic part of the Hamiltonian
44 # block M = 2
45 hm2 = np.array([
46     [1.3331, -0.667547],
47     [-0.667547, 1.3331]
48 ]) * muB * B
49 hm2 += hhfs[2:]

```

```

50 hm2f = sp.lambdify(B, hm2)
51
52 # these lists will hold the values for the calculated
53 # energy levels
54 m0f0 = [] # M = 0, F = 0
55 m0f1 = [] # M = 0, F = 1
56 m0f2 = [] # M = 0, F = 2
57 m1f1 = [] # M = 1, F = 1
58 m1f2 = [] # M = 1, F = 2
59 m2f2 = [] # M = 2, F = 2
60
61 # 100 field values, from 0 to 90 (in G)
62 BG = np.linspace(0, 90, 100)
63
64 for b in BG:
65     # get the eigenvalues of the matrix
66     ev, _ = np.linalg.eig(hm0f(b))
67     # exclude the last value from ev
68     for l, v in zip([m0f0, m0f1, m0f2], ev[:-1]):
69         l.append(v)
70
71     ev, _ = np.linalg.eig(hm1f(b))
72     for l, v in zip([m1f1, m1f2], ev[:-1]):
73         l.append(v)
74
75     ev, _ = np.linalg.eig(hmf2(b))
76     m2f2.append(ev[0])

```

We then subtract, for each hyperfine level, the ground state energy obtained before, and obtain the detuning of the imaging transition, such as those of Figure 5.7.

A.2. Transition amplitudes

For the optical transitions we are using, the relevant operator is the electric dipole operator

$$\mathbf{d} = -e\mathbf{r}_e, \quad (\text{A.15})$$

where \mathbf{r}_e is the position of the open-shell electron. The interaction between the atom and the light is governed by the Hamiltonian

$$\mathbf{H}_{\text{opt}} = -\mathbf{d} \cdot \mathbf{E}. \quad (\text{A.16})$$

The transition probability \mathcal{P} is given by [172]

$$\mathcal{P} = |\langle I, J', F', M' | \mathbf{H}_{\text{opt}} | I, J, F, M \rangle|^2 \quad (\text{A.17})$$

where $J = 1/2$, $J' = 3/2$, $F = 1$, and $M = 1$; the nuclear moment $I = 3/2$ only intervenes in the computation of the limits for F' . For each polarization of the incident light, we can write the matrix elements of this equation as

$$E_q \langle I, J', F', M+q | d_q | I, J, F, M \rangle, \quad (\text{A.18})$$

where $q = 0$ for π polarized and $q = \pm 1$ for σ^\pm polarized light, respectively. In the case of a completely polarized incident radiation, the electric field component E_q can be put equal to unity, and dropped altogether.

It can be shown [237] that, for this case, \mathcal{P} is

$$\mathcal{P} = (2F+1)(2F'+1) \begin{pmatrix} F & 1 & F' \\ M & q & -M' \end{pmatrix}^2 \begin{Bmatrix} F & 1 & F' \\ J' & I & J \end{Bmatrix}^2 |\langle J \| d \| J' \rangle|^2, \quad (\text{A.19})$$

where the object in round brackets is a Wigner-3j symbol[238]

$$\begin{pmatrix} j_1 & j_2 & J \\ m_1 & m_2 & M \end{pmatrix} = \frac{(-1)^{j_1-j_2-M}}{\sqrt{2J+1}} \mathcal{C}(j_1, m_1, j_2, m_2, J, -M), \quad (\text{A.20})$$

that in curly brackets a Wigner-6j symbol

$$\begin{Bmatrix} j_1 & j_2 & j_3 \\ J_1 & J_2 & J_3 \end{Bmatrix} = (2j_3+1) \sum_{M_p, m_q} (-1)^{\Sigma(J_i+M_i)} \begin{pmatrix} J_1 & J_2 & j_3 \\ M_1 & -M_2 & m_3 \end{pmatrix} \begin{pmatrix} J_2 & J_3 & j_1 \\ M_2 & -M_3 & m_1 \end{pmatrix} \times \begin{pmatrix} J_3 & J_1 & j_2 \\ M_3 & -M_1 & m_2 \end{pmatrix} \begin{pmatrix} j_1 & j_2 & j_3 \\ m_1 & m_2 & m_3 \end{pmatrix}, \quad (\text{A.21})$$

and $\langle J \| d \| J' \rangle$ is the reduced matrix element of the Wigner-Eckart theorem, which is constant within all the transitions on the D2 line. Therefore, the relative transition probability can be calculated from (A.19) by setting the reduced matrix element equal to 1. We also remark that all the species-dependent information is stored in the reduced matrix and, therefore, the relative strength is valid for both species, as they have the same nuclear spin.

The Sympy package, already used in the previous codes, has routines available for calculation of 3j and 6j symbols, based on [239]. It is then possible to implement the calculation for the transition amplitude, for example, for the Rb σ^- transition:

```

1 import numpy as np
2 import sympy as sp
3 from sympy.physics.wigner import wigner_6j, wigner_3j
4
5 muB = 1.399624624 # Bohr magneton, in MHz/G
6 Fhfs0 = 0
7 Fhfs1 = 72.22
8 Fhfs2 = Fhfs1 + 156.6
9 Fhfs3 = Fhfs2 + 266.65
10 hhfs = np.diag([Fhfs0, Fhfs1, Fhfs2, Fhfs3])

```

A. Calculation of high-field imaging transitions

```

11 B = sp.symbols("B")
12
13 # Hyperfine splitting of ground state
14 DF = 2 * 3.417341305452145e3 # in MHz
15
16 def amptr(Fg, Mg, Fe, Me):
17     """Calculate probability amplitude of transition
18     From state with F=Fg, M=Mg to state with F=Fe, M=Me"""
19     # Sympy numeric constant for exact expressions
20     I = sp.S(3) / 2
21     Jg = sp.S(1) / 2
22     Je = sp.S(3) / 2
23
24     # polarization
25     q = Me - Mg
26
27     # sign factor has to be added to account for square root
28     a = (-1)**(Fg - 1 + Me) * sp.sqrt(2 * Fe + 1)
29     b = wigner_3j(Fg, 1, Fe, Mg, q, -Me)
30     c = (-1)**(Fg + Je + 1 + I) * sp.sqrt((2 * Fg + 1) * (2 * Je + 1))
31     d = wigner_6j(Fg, 1, Fe, Je, I, Jg)
32     # convert to float for efficient computation
33     return float(a * b * c * d)
34
35 # Ground state magnetic Hamiltonian, M=1
36 hgm1 = sp.Matrix([
37     [-0.501827, -0.867466],
38     [-0.867466, 0.499836]]) * muB * B
39 hgm1 += np.array([[0, 0], [0, DF]])
40 hgm1f = sp.lambdify(B, hgm1)
41
42 # excited state Hamiltonian, M=0
43 hm0 = np.array([
44     [0, -1.49268, 0, 0],
45     [-1.49268, 0, -1.19414, 0],
46     [0, -1.19414, 0, -0.895608],
47     [0, 0, -0.895608, 0]
48 ]) * muB * B
49 hm0 += hhfs
50 hm0f = sp.lambdify(B, hm0)
51
52 # Magnetic field intensity
53 BG = np.linspace(0, 90, 100)

```

```

54 # eigenvectors of ground state Hamiltonian
55 gs = []
56 for b in BG:
57     _, evg = np.linalg.eig(hgRb(b))
58     # component with F=1
59     gsRb.append(esg[:, 0])
60
61 # calculate dipole matrix
62 qsm = -1 # sigma- polarization
63 dipmat = [Prf(Fg, Mg, Fe, Mg + qsm)
64           for Fe in [0, 1, 2, 3] for Fg in [1, 2]]
65 # reshape list as 4x2 matrix
66 dipmat = np.array(dipmat).reshape(4, 2)
67
68 # empty vectors to hold transition probabilities
69 smf0 = np.zeros(len(BG)) # F'=0
70 smf1 = np.zeros(len(BG)) # F'=1
71 smf2 = np.zeros(len(BG)) # F'=2
72
73 # enumerate gives, for each iteration,
74 # index and value of vector element
75 for i, b in enumerate(BG):
76     # eigenvectors of excited state Hamiltonian
77     _, es = np.linalg.eig(hm0f(b))
78     # transition probability
79     # (@ is matrix multiplication)
80     row = (es.T @ dipmat @ gsK[i])**2
81
82     smf0Rb[i] = row[0]
83     smf1Rb[i] = row[1]
84     smf2Rb[i] = row[2]

```

The results from this computation (along with the corresponding computations for the other imaging transitions) are shown, for K and Rb, in Figure 5.8.

Denoising an Optical Density image

Due to the high magnification of the high-resolution imaging system, it becomes desirable to have the ability of removing noise from the images, as even small amount of mechanical vibrations can shift the beam, with respect to the CCD camera, in the time between the acquisition of the three images necessary for the construction of the optical density image.

While some sophisticated methods for noise removal in atomic absorption images have been developed, for example [240, 241], their implementation is not necessarily suited for our situation, as they require a training phase which is specific to the kind of image to be processed.

We opted therefore for a simpler method, used in astronomical photometry [242]. The first step is discriminating the portion of the image that constitute the background from those in which a signal (condensate) is present. To do so, we use a technique called σ -clipping: for an optical density image, we assume that the pixels corresponding to a condensate constitute a brightness peak, with a lower background made of normally distributed values. It is possible to separate the brightness peak by calculating the mean μ and the variance σ^2 of the pixel brightness distribution, and then excluding from the image all those pixels whose intensity is more than $\mu + \alpha\sigma$, for some specified α ; the procedure is then repeated until no more pixels are excluded. By appropriately choosing α , we can make sure that the portion of the image with the condensate is correctly marked as such. Then, the portions of the image classified as background are convoluted with a Gaussian kernel, to smooth high-frequency noise, and, afterwards, divided in square tiles. For each image tile, a statistic of the intensity distribution is calculated, and its value is assigned to the tile; in our case, we found that the median of the tile gave a good background reduction. Finally, the background image is upscaled to the original resolution by interpolating the missing pixels with a cubic spline.

The code used for this procedure uses functions provided by the Photutils and Astropy packages [197–199, 242]. For example, for the K sub-image of Figure 5.10, the code used was:

```
1 from photutils.background import Background2D, MedianBackground
2 from astropy.stats import SigmaClip
```

Denoising of K image

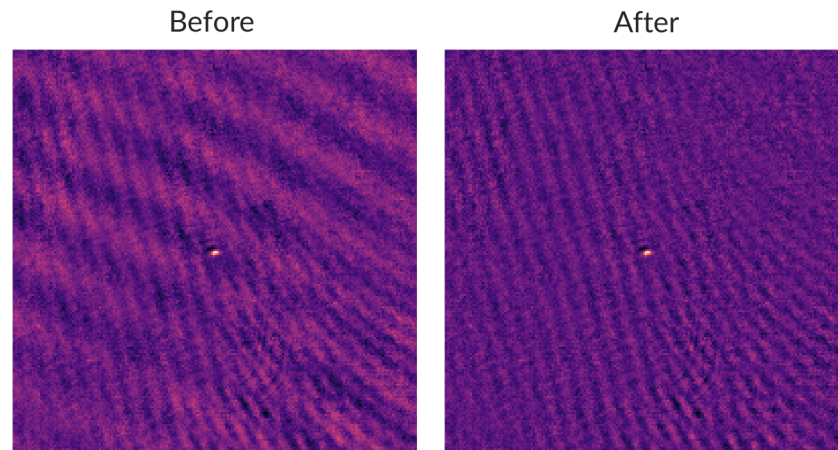


Figure B.1.: Optical density image of K, with the same data as in Figure 5.10, before and after the denoising treatment.

```
3 # parameters are selected by maximizing
4 # the amount of noise removed, while avoiding touching
5 # the actual absorption signal
6 tilesz = 2 # tiling size
7 filtsz = 5 # sigma of the Gaussian blur
8 sgth = 2.0 # alpha for sigma clipping
9
10 # initialize sigma clipping procedure
11 sigma_clip = SigmaClip(sigma=sgth)
12 # select background estimation statistic
13 # we use the median, as it provides good denoising
14 # and does not change the signal
15 bkg_estimator = MedianBackground()
16 # estimate the background image
17 bkg = Background2D(
18     imgK, # raw image for K
19     (tilesz, tilesz), # tile sizing
20     filter_size=(filtsz, filtsz), # filter sizing
21     sigma_clip=sigma_clip, # sigma clipping procedure
22     bkg_estimator=bkg_estimator # estimation statistic
23 )
24 # subtract the background
25 imgKden = imgK - bkg.background
```

Frequency content of K image

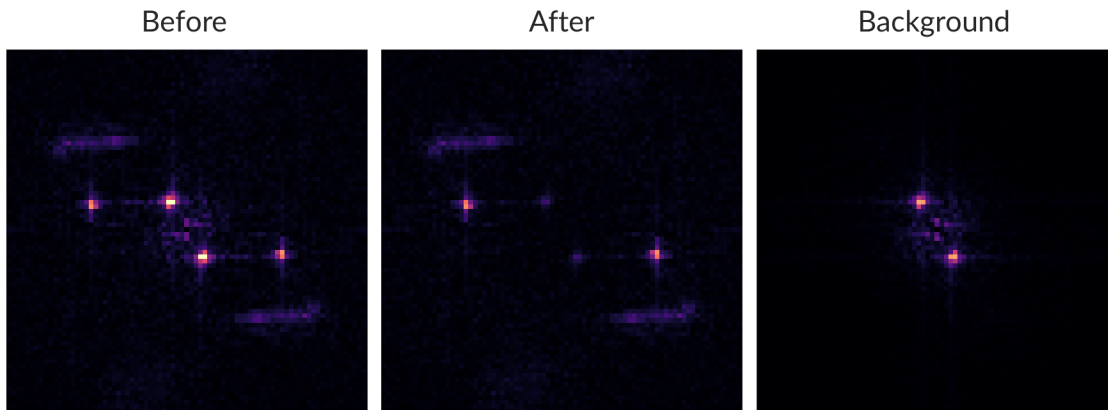


Figure B.2.: Absolute value of the Fourier transform of the corresponding images of Figure B.1, along with the Fourier transform of the estimated background.

A before and after view of the K image, with a wider crop than in Figure 5.10, is shown in Figure B.1. We can see that the long-wavelength fringes in the images are quite reduced with respect to the original image: by fitting a Gaussian to the image, we compare the RMS value of the fit residuals of the two images; the noise reduction, measured with this method, is of approximately 5 dB. Also, we assess which kind of noise is more suppressed by with this method: in Figure B.2, we show the 2-dimensional Fourier transform of the images and of the estimated background: we see that this denoising technique is most effective on the lower spatial frequencies, as we expected by looking at Figure B.1.

Acknowledgements

*«A wiser fellow than myself once said:
Sometimes you eat the bear
And, sometimes, the bear,
Well, he eats you».*
The Stranger, *The Big Lebowski*.

It is always a good idea, ending a deed, to take the time to reflect on all that happened in the intervening time, and to remember and thank all those whose help was fundamental along the way: as much as physicists like vacuums (and experimental atomic physicists even more so), it is a condition that is rarely if at all present on the social side of our lives.

First, it is in order to thank those who have been part, in whatever role, of the K-Rb team in these years. I would like to thank Prof. Francesco Minardi, for giving me the opportunity of embarking on this journey more than three years ago, when I was still a master's student in need of a thesis: I hope that, in these years, I have had the opportunity of, if partially, repaying this trust, and that my work in the future would fill the remaining. I would also like to thank Dr. Alessia Burchianti, with whom I have spent countless hours in the laboratory, and who absolved to the extremely difficult task of trying to teach me about everything that goes on in the experiment, both from a physical and a technical standpoint; whatever knowledge I have accumulated during my PhD was in no small part transmitted by her, at least for the accurate parts: for the errors, everything is—instead—of my own. As, possibly against better judgement, she has decided to enroll me for some other time, I will try to make sure that all these lessons will be remembered and used in full. I would like to thank Dr. Chiara Fort, whose expertise on the matter of quantum gases has oftentimes proven invaluable, and whose discussions and numerical simulations have been, and still are, always a source of new ideas.

During this last year, I have had the pleasure of doing my internship in the Quantum Gases group at ICFO. I would like to thank Prof. Leticia Tarruell for making it possible to have such a wonderful opportunity, which has been a source of professional growth and improvement. I would also like to thank everyone in the group, and especially in the K experiment, to which I was attached, for welcoming me and integrating me in the team with such an efficiency that, after no more than a week, I already felt an integral part of what was going on. I hope that something I did will remain with you, because I have been given a lot by you. Thanks also to Craig, Jelena, and Martina for the Sunday lunches and the time spent together (and, to

Craig, also for the most well-explained notes on linear systems that have ever come out of New Zealand).

Returning back home, I would also like to thank anyone, in the physics department or at LENS, who has helped me during these three years. Whether it was helping to fix esoteric electronics made twenty years ago, or lending a ladder, or answering my questions about various administrative procedures, I appreciated every little bit of help.

I would like to thank Aitor for all the discussions about both physics and the finer aspects of Italian and Basque culture, and for his incursions in the lab during his stay in Florence, in search for some cold relief.

Last, but by no means least, I would also like to thank my friends and family, who have been with me through thick and thin, and without whom I simply would not be who I am today. I am grateful to have you by my side.

I dedicate this thesis to the memory of A. M. and A. B.

Bibliography

1. Planck, M. Ueber das Gesetz der Energieverteilung im Normalspectrum. *Annalen der Physik* **309**, 553 (1901) (cit. on p. 1).
2. Bose, S. N. Plancks Gesetz und Lichtquantenhypothese. *Zeitschrift für Physik* **26**, 178 (1924) (cit. on p. 1).
3. Einstein, A. Quantentheorie Des Einatomigen Idealen Gases. *Sitzungsberichte der Preussischen Akademie der Wissenschaften* (1924) (cit. on p. 1).
4. Fermi, E. Sulla Quantizzazione Del Gas Perfetto Monoatomico. *Rendiconti Lincei* **145** (1926) (cit. on p. 1).
5. Dirac, P. A. M. On the Theory of Quantum Mechanics. *Proceedings of the Royal Society of London. Series A, Containing Papers of a Mathematical and Physical Character* **112**, 661 (1926) (cit. on p. 1).
6. Kapitza, P. Viscosity of Liquid Helium below the λ -Point. *Nature* **141**, 74 (1938) (cit. on p. 1).
7. London, F. The λ -Phenomenon of Liquid Helium and the Bose-Einstein Degeneracy. *Nature* **141**, 643 (1938) (cit. on p. 1).
8. Kamerlingh Onnes, H. Further Experiments with Liquid Helium. C. On the Change of Electric Resistance of Pure Metals at Very Low Temperatures, Etc. IV. The Resistance of Pure Mercury at Helium Temperatures. *KNAW Proceedings* **13**, 1274 (1911) (cit. on p. 1).
9. Bardeen, J., Cooper, L. N. & Schrieffer, J. R. Microscopic Theory of Superconductivity. *Physical Review* **106**, 162 (1957) (cit. on p. 1).
10. Stwalley, W. C. Stability of Spin-Aligned Hydrogen at Low Temperatures and High Magnetic Fields: New Field-Dependent Scattering Resonances and Predissociations. *Physical Review Letters* **37**, 1628 (1976) (cit. on p. 1).
11. Hänsch, T. & Schawlow, A. Cooling of Gases by Laser Radiation. *Optics Communications* **13**, 68 (1975) (cit. on p. 1).
12. Phillips, W. D. & Metcalf, H. Laser Deceleration of an Atomic Beam. *Physical Review Letters* **48**, 596 (1982) (cit. on p. 1).
13. Migdall, A. L., Prodan, J. V., Phillips, W. D., Bergeman, T. H. & Metcalf, H. J. First Observation of Magnetically Trapped Neutral Atoms. *Physical Review Letters* **54**, 2596 (1985) (cit. on p. 1).

14. Anderson, M. H., Ensher, J. R., Matthews, M. R., Weiman, C. E. & Cornell, E. A. Observation of Bose-Einstein Condensation in a Dilute Atomic Vapor. *Science* **269**, 198 (1995) (cit. on p. 1).
15. Bradley, C. C., Sackett, C. A., Tollett, J. J. & Hulet, R. G. Evidence of Bose-Einstein Condensation in an Atomic Gas with Attractive Interactions. *Physical Review Letters* **75**, 1687 (1995) (cit. on p. 1).
16. Davis, K. B. Bose-Einstein Condensation in a Gas of Sodium Atoms. *Physical Review Letters* **75**, 5 (1995) (cit. on p. 1).
17. Ho, T.-L. & Shenoy, V. B. Binary Mixtures of Bose Condensates of Alkali Atoms. *Physical Review Letters* **77**, 3276 (1996) (cit. on p. 1).
18. Pu, H. & Bigelow, N. P. Collective Excitations, Metastability, and Nonlinear Response of a Trapped Two-Species Bose-Einstein Condensate. *Physical Review Letters* **80**, 1134 (1998) (cit. on pp. 1, 19, 20).
19. Guttman, L. & Arnold, J. R. The Nonparticipation of He 6 in the Superfluidity of He 4. *Physical Review* **92**, 547 (1953) (cit. on p. 1).
20. Khalatnikov, I. M. Hydrodynamics of Solutions of Two Superfluid Liquids. *Soviet Journal of Experimental and Theoretical Physics* **5**, 542 (1957) (cit. on p. 1).
21. Edwards, D. O., Brewer, D. F., Seligman, P., Skertic, M. & Yaqub, M. Solubility of He 3 in Liquid He 4 at 0°K. *Physical Review Letters* **15**, 773 (1965) (cit. on p. 1).
22. Andreev, A. F. & Bashkin, E. P. Three-Velocity Hydrodynamics of Superfluid Solutions. *Soviet Journal of Experimental and Theoretical Physics* **42**, 164 (1975) (cit. on pp. 1, 19).
23. Colson, W. B. & Fetter, A. L. Mixtures of Bose Liquids at Finite Temperature. *Journal of Low Temperature Physics* **33**, 231 (1978) (cit. on p. 1).
24. Myatt, C. J., Burt, E. A., Ghrist, R. W., Cornell, E. A. & Wieman, C. E. Production of Two Overlapping Bose-Einstein Condensates by Sympathetic Cooling. *Physical Review Letters* **78** (1997) (cit. on p. 1).
25. Stenger, J., Inouye, S., Stamper-Kurn, D. M., Miesner, H.-J., Chikkatur, A. P. & Ketterle, W. Spin Domains in Ground-State Bose-Einstein Condensates. *Nature* **396**, 345 (1998) (cit. on p. 1).
26. Modugno, G., Modugno, M., Riboli, F., Roati, G. & Inguscio, M. Two Atomic Species Superfluid. *Physical Review Letters* **89**, 190404 (2002) (cit. on pp. 1, 2, 49).
27. Iskin, M. & Sá De Melo, C. A. R. Two-Band Superfluidity from the BCS to the BEC Limit. *Physical Review B* **74**, 144517 (2006) (cit. on p. 1).
28. Tajima, H., Yerin, Y., Perali, A. & Pieri, P. Enhanced Critical Temperature, Pairing Fluctuation Effects, and BCS-BEC Crossover in a Two-Band Fermi Gas. *Physical Review B* **99**, 180503 (2019) (cit. on p. 1).
29. Salasnich, L., Shanenko, A. A., Vagov, A., Aguiar, J. A. & Perali, A. Screening of Pair Fluctuations in Superconductors with Coupled Shallow and Deep Bands: A Route to Higher-Temperature Superconductivity. *Physical Review B* **100**, 064510 (2019) (cit. on p. 1).

30. Yerin, Y., Tajima, H., Pieri, P. & Perali, A. Coexistence of Giant Cooper Pairs with a Bosonic Condensate and Anomalous Behavior of Energy Gaps in the BCS-BEC Crossover of a Two-Band Superfluid Fermi Gas. *Physical Review B* **100**, 104528 (2019) (cit. on p. 1).
31. Alpar, M. A., Langer, S. A. & Sauls, J. A. Rapid Postglitch Spin-up of the Superfluid Core in Pulsars. *The Astrophysical Journal* **282**, 533 (1984) (cit. on p. 1).
32. Andersson, N., Comer, G. L. & Prix, R. Are Pulsar Glitches Triggered by a Superfluid Two-Stream Instability? *Physical Review Letters* **90**, 091101 (2003) (cit. on p. 1).
33. Kobyakov, D. N. & Pethick, C. J. Two-Component Superfluid Hydrodynamics of Neutron Star Cores. *The Astrophysical Journal* **836**, 203 (2017) (cit. on p. 1).
34. Ferrier-Barbut, I., Delehay, M., Laurent, S., Grier, A. T., Pierce, M., Rem, B. S., Chevy, F. & Salomon, C. A Mixture of Bose and Fermi Superfluids. *Science* **345**, 1035 (2014) (cit. on pp. 2, 49).
35. Roy, R., Green, A., Bowler, R. & Gupta, S. Two-Element Mixture of Bose and Fermi Superfluids. *Physical Review Letters* **118**, 055301 (2017) (cit. on pp. 2, 49).
36. Schirotzek, A., Wu, C.-H., Sommer, A. & Zwierlein, M. W. Observation of Fermi Polarons in a Tunable Fermi Liquid of Ultracold Atoms. *Physical Review Letters* **102**, 230402 (2009) (cit. on p. 2).
37. Kohstall, C., Zaccanti, M., Jag, M., Trenkwalder, A., Massignan, P., Bruun, G. M., Schreck, F. & Grimm, R. Metastability and Coherence of Repulsive Polarons in a Strongly Interacting Fermi Mixture. *Nature* **485**, 615 (2012) (cit. on p. 2).
38. Hu, M.-G., Van De Graaff, M. J., Kedar, D., Corson, J. P., Cornell, E. A. & Jin, D. S. Bose Polarons in the Strongly Interacting Regime. *Physical Review Letters* **117**, 055301 (2016) (cit. on p. 2).
39. Jørgensen, N. B., Wacker, L., Skalmstang, K. T., Parish, M. M., Levinsen, J., Christensen, R. S., Bruun, G. M. & Arlt, J. J. Observation of Attractive and Repulsive Polarons in a Bose-Einstein Condensate. *Physical Review Letters* **117**, 055302 (2016) (cit. on p. 2).
40. Takeuchi, H., Ishino, S. & Tsubota, M. Binary Quantum Turbulence Arising from Countersuperflow Instability in Two-Component Bose-Einstein Condensates. *Physical Review Letters* **105**, 205301 (2010) (cit. on p. 2).
41. Hamner, C., Chang, J. J., Engels, P. & Hofer, M. A. Generation of Dark-Bright Soliton Trains in Superfluid-Superfluid Counterflow. *Physical Review Letters* **106**, 065302 (2011) (cit. on pp. 2, 49).
42. DeSalvo, B. J., Patel, K., Cai, G. & Chin, C. Observation of Fermion-Mediated Interactions between Bosonic Atoms. *Nature* **568**, 61 (2019) (cit. on p. 2).
43. Tung, S.-K., Jiménez-García, K., Johansen, J., Parker, C. V. & Chin, C. Geometric Scaling of Efimov States in a Li 6 – Cs 133 Mixture. *Physical Review Letters* **113**, 240402 (2014) (cit. on p. 2).

44. Pires, R., Ulmanis, J., Häfner, S., Repp, M., Arias, A., Kuhnle, E. D. & Weidemüller, M. Observation of Efimov Resonances in a Mixture with Extreme Mass Imbalance. *Physical Review Letters* **112**, 250404 (2014) (cit. on p. 2).
45. Maier, R. A. W., Eisele, M., Tiemann, E. & Zimmermann, C. Efimov Resonance and Three-Body Parameter in a Lithium-Rubidium Mixture. *Physical Review Letters* **115**, 043201 (2015) (cit. on p. 2).
46. Ulmanis, J., Häfner, S., Pires, R., Kuhnle, E. D., Wang, Y., Greene, C. H. & Weidemüller, M. Heteronuclear Efimov Scenario with Positive Intraspecies Scattering Length. *Physical Review Letters* **117**, 153201 (2016) (cit. on p. 2).
47. Schlippert, D., Hartwig, J., Albers, H., Richardson, L. L., Schubert, C., Roura, A., Schleich, W. P., Ertmer, W. & Rasel, E. M. Quantum Test of the Universality of Free Fall. *Physical Review Letters* **112**, 203002 (2014) (cit. on p. 2).
48. Zhou, L. *et al.* Test of Equivalence Principle at 1 0 – 8 Level by a Dual-Species Double-Diffraction Raman Atom Interferometer. *Physical Review Letters* **115**, 013004 (2015) (cit. on p. 2).
49. Asenbaum, P., Overstreet, C., Kim, M., Curti, J. & Kasevich, M. A. Atom-Interferometric Test of the Equivalence Principle at the 10 – 12 Level. *Physical Review Letters* **125**, 191101 (2020) (cit. on p. 2).
50. Ni, K.-K., Ospelkaus, S., De Miranda, M. H. G., Pe'er, A., Neyenhuis, B., Zirbel, J. J., Kotochigova, S., Julienne, P. S., Jin, D. S. & Ye, J. A High Phase-Space-Density Gas of Polar Molecules. *Science* **322**, 231 (2008) (cit. on p. 2).
51. Molony, P. K., Kumar, A., Gregory, P. D., Kliese, R., Puppe, T., Le Sueur, C. R., Aldegunde, J., Hutson, J. M. & Cornish, S. L. Measurement of the Binding Energy of Ultracold Rb 87 Cs 133 Molecules Using an Offset-Free Optical Frequency Comb. *Physical Review A* **94**, 022507 (2016) (cit. on p. 2).
52. Takekoshi, T., Reichsöllner, L., Schindewolf, A., Hutson, J. M., Le Sueur, C. R., Dulieu, O., Ferlaino, F., Grimm, R. & Nägerl, H.-C. Ultracold Dense Samples of Dipolar RbCs Molecules in the Rovibrational and Hyperfine Ground State. *Physical Review Letters* **113**, 205301 (2014) (cit. on p. 2).
53. Park, J. W., Will, S. A. & Zwierlein, M. W. Ultracold Dipolar Gas of Fermionic Na 23 K 40 Molecules in Their Absolute Ground State. *Physical Review Letters* **114**, 205302 (2015) (cit. on p. 2).
54. Guo, M., Zhu, B., Lu, B., Ye, X., Wang, F., Vexiau, R., Bouloufa-Maafa, N., Quéméner, G., Dulieu, O. & Wang, D. Creation of an Ultracold Gas of Ground-State Dipolar Na 23 Rb 87 Molecules. *Physical Review Letters* **116**, 205303 (2016) (cit. on p. 2).
55. Rvachov, T. M., Son, H., Sommer, A. T., Ebadi, S., Park, J. J., Zwierlein, M. W., Ketterle, W. & Jamison, A. O. Long-Lived Ultracold Molecules with Electric and Magnetic Dipole Moments. *Physical Review Letters* **119**, 143001 (2017) (cit. on p. 2).

56. Yang, H., Zhang, D.-C., Liu, L., Liu, Y.-X., Nan, J., Zhao, B. & Pan, J.-W. Observation of Magnetically Tunable Feshbach Resonances in Ultracold $^{23}\text{Na} + ^{40}\text{K}$ Collisions. *Science* **363**, 261 (2019) (cit. on p. 2).
57. Voges, K. K., Gersema, P., Hartmann, T., Schulze, T. A., Zenesini, A. & Ospelkaus, S. Formation of Ultracold Weakly Bound Dimers of Bosonic $^{23}\text{Na} + ^{39}\text{K}$. *Physical Review A* **101**, 042704 (2020) (cit. on pp. 2, 3).
58. Petrov, D. S. Quantum Mechanical Stabilization of a Collapsing Bose-Bose Mixture. *Physical Review Letters* **115**, 155302 (2015) (cit. on pp. 2, 23–25).
59. Ferrier-Barbut, I., Kadau, H., Schmitt, M., Wenzel, M. & Pfau, T. Observation of Quantum Droplets in a Strongly Dipolar Bose Gas. *Physical Review Letters* **116**, 215301 (2016) (cit. on pp. 2, 24).
60. Chomaz, L., Baier, S., Petter, D., Mark, M. J., Wächtler, F., Santos, L. & Ferlaino, F. Quantum-Fluctuation-Driven Crossover from a Dilute Bose-Einstein Condensate to a Macrodroplet in a Dipolar Quantum Fluid. *Physical Review X* **6**, 041039 (2016) (cit. on pp. 2, 24, 25).
61. Cabrera, C. R., Tanzi, L., Sanz, J., Naylor, B., Thomas, P., Cheiney, P. & Tarruell, L. Quantum Liquid Droplets in a Mixture of Bose-Einstein Condensates. *Science* **359**, 301 (2018) (cit. on pp. 2, 24, 25).
62. Semeghini, G., Ferioli, G., Masi, L., Mazzinghi, C., Wolswijk, L., Minardi, F., Modugno, M., Modugno, G., Inguscio, M. & Fattori, M. Self-Bound Quantum Droplets of Atomic Mixtures in Free Space. *Physical Review Letters* **120**, 235301 (2018) (cit. on pp. 2, 24).
63. Ferioli, G., Semeghini, G., Masi, L., Giusti, G., Modugno, G., Inguscio, M., Gallemi, A., Recati, A. & Fattori, M. Collisions of Self-Bound Quantum Droplets. *Physical Review Letters* **122**, 090401 (2019) (cit. on p. 2).
64. Cheiney, P., Cabrera, C. R., Sanz, J., Naylor, B., Tanzi, L. & Tarruell, L. Bright Soliton to Quantum Droplet Transition in a Mixture of Bose-Einstein Condensates. *Physical Review Letters* **120**, 135301 (2018) (cit. on pp. 2, 25).
65. D’Errico, C., Burchianti, A., Prevedelli, M., Salasnich, L., Ancilotto, F., Modugno, M., Minardi, F. & Fort, C. Observation of Quantum Droplets in a Heteronuclear Bosonic Mixture. *Physical Review Research* **1**, 033155 (2019) (cit. on pp. 2, 24, 25, 27, 65).
66. Guo, Z., Jia, F., Li, L., Ma, Y., Hutson, J. M., Cui, X. & Wang, D. Lee-Huang-Yang Effects in the Ultracold Mixture of ^{23}Na and ^{87}Rb with Attractive Interspecies Interactions. *Physical Review Research* **3**, 033247 (2021) (cit. on p. 2).
67. Bloch, I., Dalibard, J. & Zwerger, W. Many-Body Physics with Ultracold Gases. *Reviews of Modern Physics* **80**, 885 (2008) (cit. on p. 2).
68. Sanz, J., Frölian, A., Chisholm, C. S., Cabrera, C. R. & Tarruell, L. Interaction Control and Bright Solitons in Coherently Coupled Bose-Einstein Condensates. *Physical Review Letters* **128**, 013201 (2022) (cit. on p. 2).

69. Williams, R. A., LeBlanc, L. J., Jiménez-García, K., Beeler, M. C., Perry, A. R., Phillips, W. D. & Spielman, I. B. Synthetic Partial Waves in Ultracold Atomic Collisions. *Science* **335**, 314 (2012) (cit. on p. 2).
70. Chin, C., Grimm, R., Julienne, P. & Tiesinga, E. Feshbach Resonances in Ultracold Gases. *Reviews of Modern Physics* **82**, 1225 (2010) (cit. on pp. 2, 8, 9, 11).
71. Thalhammer, G., Barontini, G., De Sarlo, L., Catani, J., Minardi, F. & Inguscio, M. Double Species Bose-Einstein Condensate with Tunable Interspecies Interactions. *Physical Review Letters* **100**, 210402 (2008) (cit. on pp. 2, 11–14).
72. Elsen, M. *et al.* A Dual-Species Atom Interferometer Payload for Operation on Sounding Rockets. *Microgravity Science and Technology* **35**, 48 (2023) (cit. on p. 2).
73. Elliott, E. R. *et al.* Quantum Gas Mixtures and Dual-Species Atom Interferometry in Space. *Nature* **623**, 502 (2023) (cit. on p. 2).
74. Hewitt, T., Bertheas, T., Jain, M., Nishida, Y. & Barontini, G. *Controlling the Interactions in a Cold Atom Quantum Impurity System* arXiv: [2310.02771](https://arxiv.org/abs/2310.02771). preprint (cit. on p. 2).
75. Lercher, A. D., Takekoshi, T., Debatin, M., Schuster, B., Rameshan, R., Ferlaino, F., Grimm, R. & Nägerl, H. -. Production of a Dual-Species Bose-Einstein Condensate of Rb and Cs Atoms. *The European Physical Journal D* **65**, 3 (2011) (cit. on p. 2).
76. McCarron, D. J., Cho, H. W., Jenkin, D. L., Köppinger, M. P. & Cornish, S. L. Dual-Species Bose-Einstein Condensate of Rb 87 and Cs 133. *Physical Review A* **84**, 011603 (2011) (cit. on p. 2).
77. Pilch, K., Lange, A. D., Prantner, A., Kerner, G., Ferlaino, F., Nägerl, H.-C. & Grimm, R. Observation of Interspecies Feshbach Resonances in an Ultracold Rb-Cs Mixture. *Physical Review A* **79**, 042718 (2009) (cit. on p. 2).
78. Vuletić, V., Kerman, A. J., Chin, C. & Chu, S. Observation of Low-Field Feshbach Resonances in Collisions of Cesium Atoms. *Physical Review Letters* **82**, 1406 (1999) (cit. on p. 2).
79. Pasquiou, B., Bayerle, A., Tzanova, S. M., Stellmer, S., Szczepkowski, J., Parigger, M., Grimm, R. & Schreck, F. Quantum Degenerate Mixtures of Strontium and Rubidium Atoms. *Physical Review A* **88**, 023601 (2013) (cit. on p. 2).
80. Barbé, V., Ciamei, A., Pasquiou, B., Reichsöllner, L., Schreck, F., Żuchowski, P. S. & Hutson, J. M. Observation of Feshbach Resonances between Alkali and Closed-Shell Atoms. *Nature Physics* **14**, 881 (2018) (cit. on p. 3).
81. Wacker, L., Jørgensen, N. B., Birkmose, D., Horchani, R., Ertmer, W., Klempt, C., Winter, N., Sherson, J. & Arlt, J. J. Tunable Dual-Species Bose-Einstein Condensates of K 39 and Rb 87. *Physical Review A* **92**, 053602 (2015) (cit. on p. 3).
82. Mi, C.-D., Nawaz, K. S., Wang, P.-J., Chen, L.-C., Meng, Z.-M., Huang, L. & Zhang, J. Production of Dual Species Bose-Einstein Condensates of ³⁹K and ⁸⁷Rb. *Chinese Physics B* **30**, 063401 (2021) (cit. on p. 3).

83. Roati, G., Zaccanti, M., D’Errico, C., Catani, J., Modugno, M., Simoni, A., Inguscio, M. & Modugno, G. K 39 Bose-Einstein Condensate with Tunable Interactions. *Physical Review Letters* **99**, 010403 (2007) (cit. on p. 3).
84. Simoni, A., Zaccanti, M., D’Errico, C., Fattori, M., Roati, G., Inguscio, M. & Modugno, G. Near-Threshold Model for Ultracold KRb Dimers from Interisotope Feshbach Spectroscopy. *Physical Review A* **77**, 052705 (2008) (cit. on pp. 3, 12, 13).
85. Schulze, T. A., Hartmann, T., Voges, K. K., Gempel, M. W., Tiemann, E., Zenesini, A. & Ospelkaus, S. Feshbach Spectroscopy and Dual-Species Bose-Einstein Condensation of Na 23 – K 39 Mixtures. *Physical Review A* **97**, 023623 (2018) (cit. on p. 3).
86. Durastante, G., Politi, C., Sohmen, M., Ilzhöfer, P., Mark, M. J., Norcia, M. A. & Ferlaino, F. Feshbach Resonances in an Erbium-Dysprosium Dipolar Mixture. *Physical Review A* **102**, 033330 (2020) (cit. on p. 3).
87. Politi, C., Trautmann, A., Ilzhöfer, P., Durastante, G., Mark, M. J., Modugno, M. & Ferlaino, F. Interspecies Interactions in an Ultracold Dipolar Mixture. *Physical Review A* **105**, 023304 (2022) (cit. on p. 3).
88. Wilson, K. E., Guttridge, A., Segal, J. & Cornish, S. L. Quantum Degenerate Mixtures of Cs and Yb. *Physical Review A* **103**, 033306 (2021) (cit. on pp. 3, 49).
89. Warner, C., Lam, A. Z., Bigagli, N., Liu, H. C., Stevenson, I. & Will, S. Overlapping Bose-Einstein Condensates of Na 23 and Cs 133. *Physical Review A* **104**, 033302 (2021) (cit. on p. 3).
90. Lam, A. Z., Bigagli, N., Warner, C., Yuan, W., Zhang, S., Tiemann, E., Stevenson, I. & Will, S. High Phase-Space Density Gas of NaCs Feshbach Molecules. *Physical Review Research* **4**, L022019 (2022) (cit. on p. 3).
91. Chen, Y.-D., Li, W.-X., Sun, Y.-T., Chen, Q.-C., Chang, P.-Y. & Tung, S. Dual-Species Bose-Einstein Condensates of Li 7 and Cs 133. *Physical Review A* **108**, 033301 (2023) (cit. on p. 3).
92. Cavicchioli, L., Fort, C., Modugno, M., Minardi, F. & Burchianti, A. Dipole Dynamics of an Interacting Bosonic Mixture. *Physical Review Research* **4**, 043068 (2022) (cit. on pp. 4, 49, 56).
93. Landau, L. D. & Lifshitz, E. M. *Statistical Physics, Part 1* 2nd ed. *Course of Theoretical Physics* **5** (Pergamon Press, Oxford, 1968) (cit. on pp. 5, 15).
94. Pitaevskii, L. P. & Stringari, S. *Bose Einstein Condensation and Superfluidity* (Oxford University Press, 2016) (cit. on pp. 5, 14, 17, 50, 51).
95. *Handbook of Mathematical Functions: With Formulas, Graphs, and Mathematical Tables* 9th ed. (eds Abramowitz, M. & Stegun, I. A.) (Dover Publ, New York, NY, 2013) (cit. on p. 6).
96. Landau, L. D. & Lifshitz, E. M. *Quantum Mechanics, Non-Relativistic Theory* 2nd ed. *Course of Theoretical Physics* **3** (Pergamon Press, Oxford, 1965) (cit. on pp. 6, 8).
97. Dalibard, J. *Les Interactions Entre Atomes Dans Les Gaz Quantiques* (2021) (cit. on pp. 7, 8).

98. Sadeghpour, H. R., Bohn, J. L., Cavagnero, M. J., Esry, B. D., Fabrikant, I. I., Macek, J. H. & Rau, A. R. P. Collisions near Threshold in Atomic and Molecular Physics. *Journal of Physics B: Atomic, Molecular and Optical Physics* **33**, R93 (2000) (cit. on p. 7).
99. Mott, N. F. The Collision between Two Electrons. *Proceedings of the Royal Society of London. Series A, Containing Papers of a Mathematical and Physical Character* **126**, 259 (1930) (cit. on p. 8).
100. Rutherford, E. LXXIX. The Scattering of α and β Particles by Matter and the Structure of the Atom. *The London, Edinburgh, and Dublin Philosophical Magazine and Journal of Science* **21**, 669 (1911) (cit. on p. 8).
101. Feshbach, H. Unified Theory of Nuclear Reactions. *Annals of Physics* **5**, 357 (1958) (cit. on p. 8).
102. Feshbach, H. A Unified Theory of Nuclear Reactions. II. *Annals of Physics* **19**, 287 (1962) (cit. on p. 8).
103. Fano, U. Effects of Configuration Interaction on Intensities and Phase Shifts. *Physical Review* **124**, 1866 (1961) (cit. on pp. 8, 10, 11).
104. *The IUPAC Compendium of Chemical Terminology: The Gold Book* 4th ed. (ed Gold, V.) (International Union of Pure and Applied Chemistry (IUPAC), Research Triangle Park, NC, 2019) (cit. on p. 8).
105. Arndt, M., Ben Dahan, M., Guéry-Odelin, D., Reynolds, M. W. & Dalibard, J. Observation of a Zero-Energy Resonance in Cs-Cs Collisions. *Physical Review Letters* **79**, 625 (1997) (cit. on p. 8).
106. Volz, T., Dürr, S., Syassen, N., Rempe, G., Van Kempen, E. & Kokkelmans, S. Feshbach Spectroscopy of a Shape Resonance. *Physical Review A* **72**, 010704 (2005) (cit. on p. 9).
107. Yao, X.-C. *et al.* Degenerate Bose Gases near a D-Wave Shape Resonance. *Nature Physics* **15**, 570 (2019) (cit. on p. 9).
108. Olshanii, M. Atomic Scattering in the Presence of an External Confinement and a Gas of Impenetrable Bosons. *Physical Review Letters* **81**, 938 (1998) (cit. on p. 9).
109. Bergeman, T., Moore, M. G. & Olshanii, M. Atom-Atom Scattering under Cylindrical Harmonic Confinement: Numerical and Analytic Studies of the Confinement Induced Resonance. *Physical Review Letters* **91**, 163201 (2003) (cit. on p. 9).
110. Haller, E., Gustavsson, M., Mark, M. J., Danzl, J. G., Hart, R., Pupillo, G. & Nägerl, H.-C. Realization of an Excited, Strongly Correlated Quantum Gas Phase. *Science* **325**, 1224 (2009) (cit. on p. 9).
111. Massignan, P. & Castin, Y. Three-Dimensional Strong Localization of Matter Waves by Scattering from Atoms in a Lattice with a Confinement-Induced Resonance. *Physical Review A* **74**, 013616 (2006) (cit. on p. 9).
112. Nishida, Y. & Tan, S. Universal Fermi Gases in Mixed Dimensions. *Physical Review Letters* **101**, 170401 (2008) (cit. on p. 9).

113. Lamporesi, G., Catani, J., Barontini, G., Nishida, Y., Inguscio, M. & Minardi, F. Scattering in Mixed Dimensions with Ultracold Gases. *Physical Review Letters* **104**, 153202 (2010) (cit. on p. 9).
114. Inouye, S., Andrews, M. R., Stenger, J., Miesner, H.-J., Stamper-Kurn, D. M. & Ketterle, W. Observation of Feshbach Resonances in a Bose–Einstein Condensate. *Nature* **392**, 151 (1998) (cit. on p. 9).
115. Stwalley, W. C. & Nosanow, L. H. Possible "New" Quantum Systems. *Physical Review Letters* **36**, 910 (1976) (cit. on p. 9).
116. Fedichev, P. O., Kagan, Yu., Shlyapnikov, G. V. & Walraven, J. T. M. Influence of Nearly Resonant Light on the Scattering Length in Low-Temperature Atomic Gases. *Physical Review Letters* **77**, 2913 (1996) (cit. on p. 9).
117. Theis, M., Thalhammer, G., Winkler, K., Hellwig, M., Ruff, G., Grimm, R. & Denschlag, J. H. Tuning the Scattering Length with an Optically Induced Feshbach Resonance. *Physical Review Letters* **93**, 123001 (2004) (cit. on p. 9).
118. Riley, K. F., Hobson, M. P. & Bence, S. J. *Mathematical Methods for Physics and Engineering* 3rd ed. (Cambridge University Press, Cambridge ; New York, 2006) (cit. on p. 10).
119. Laue, T., Tiesinga, E., Samuelis, C., Knöckel, H. & Tiemann, E. Magnetic-Field Imaging of Weakly Bound Levels of the Ground-State Na₂ Dimer. *Physical Review A* **65**, 023412 (2002) (cit. on p. 11).
120. Moerdijk, A. J., Verhaar, B. J. & Axelsson, A. Resonances in Ultracold Collisions of Li 6, Li 7, and Na 23. *Physical Review A* **51**, 4852 (1995) (cit. on p. 11).
121. Ferrari, G., Inguscio, M., Jastrzebski, W., Modugno, G., Roati, G. & Simoni, A. Collisional Properties of Ultracold K-Rb Mixtures. *Physical Review Letters* **89**, 053202 (2002) (cit. on pp. 11, 12).
122. Marinescu, M. & Sadeghpour, H. R. Long-Range Potentials for Two-Species Alkali-Metal Atoms. *Physical Review A* **59**, 390 (1999) (cit. on p. 12).
123. Simoni, A., Ferlaino, F., Roati, G., Modugno, G. & Inguscio, M. Magnetic Control of the Interaction in Ultracold K-Rb Mixtures. *Physical Review Letters* **90**, 163202 (2003) (cit. on p. 11).
124. Ferlaino, F., D'Errico, C., Roati, G., Zaccanti, M., Inguscio, M., Modugno, G. & Simoni, A. Feshbach Spectroscopy of a K-Rb Atomic Mixture. *Physical Review A* **73**, 040702 (2006) (cit. on pp. 11, 13).
125. Wacker, L. J., Jørgensen, N. B., Birkmose, D., Winter, N., Mikkelsen, M., Sherson, J., Zinner, N. & Arlt, J. J. Supplementary Material to "Universal Three-Body Physics in Ultracold KRb Mixtures" (2016) (cit. on p. 11).
126. Köhler, T., Góral, K. & Julienne, P. S. Production of Cold Molecules via Magnetically Tunable Feshbach Resonances. *Reviews of Modern Physics* **78**, 1311 (2006) (cit. on p. 12).
127. Smirnov, B. M. & Chibisov, M. I. Electron Exchange and Changes in the Hyperfine State of Colliding Alkaline Metal Atoms. *Soviet Journal of Experimental and Theoretical Physics* **21**, 624 (1965) (cit. on p. 13).

128. Tiesinga, E., Williams, C., Julienne, P., Jones, K., Lett, P. & Phillips, W. A Spectroscopic Determination of Scattering Lengths for Sodium Atom Collisions. *Journal of Research of the National Institute of Standards and Technology* **101**, 505 (1996) (cit. on p. 13).
129. Thalhammer, G., Barontini, G., Catani, J., Rabatti, F., Weber, C., Simoni, A., Minardi, F. & Inguscio, M. Collisional and Molecular Spectroscopy in an Ultracold Bose–Bose Mixture. *New Journal of Physics* **11**, 055044 (2009) (cit. on pp. 13, 14, 41).
130. Wacker, L. J., Jørgensen, N. B., Birkmose, D., Winter, N., Mikkelsen, M., Sherson, J., Zinner, N. & Arlt, J. J. Universal Three-Body Physics in Ultracold KRb Mixtures. *Physical Review Letters* **117**, 163201 (2016) (cit. on p. 14).
131. Hellmann, H. A New Approximation Method in the Problem of Many Electrons. *The Journal of Chemical Physics* **3**, 61 (1935) (cit. on p. 15).
132. Bogoliubov, N. On the Theory of Superfluidity. *J. Phys* **11**, 23 (1947) (cit. on pp. 15, 16).
133. Gross, E. P. Structure of a Quantized Vortex in Boson Systems. *Il Nuovo Cimento* **20**, 454 (1961) (cit. on p. 17).
134. Gross, E. P. Hydrodynamics of a Superfluid Condensate. *Journal of Mathematical Physics* **4**, 195 (1963) (cit. on p. 17).
135. Pitaevskii, L. P. Vortex Lines in an Imperfect Bose Gas. *Soviet Journal of Experimental and Theoretical Physics* **13**, 451 (1961) (cit. on p. 17).
136. Chiofalo, M. L., Succi, S. & Tosi, M. P. Ground State of Trapped Interacting Bose-Einstein Condensates by an Explicit Imaginary-Time Algorithm. *Physical Review E* **62**, 7438 (2000) (cit. on p. 18).
137. Adhikari, S. K. & Muruganandam, P. Bose–Einstein Condensation Dynamics from the Numerical Solution of the Gross–Pitaevskii Equation. *Journal of Physics B: Atomic, Molecular and Optical Physics* **35**, 2831 (2002) (cit. on p. 18).
138. Stringari, S. Collective Excitations of a Trapped Bose-Condensed Gas. *Physical Review Letters* **77**, 2360 (1996) (cit. on pp. 18, 50, 52).
139. Feynman, R. P., Metropolis, N. & Teller, E. Equations of State of Elements Based on the Generalized Fermi-Thomas Theory. *Physical Review* **75**, 1561 (1949) (cit. on p. 19).
140. Nespolo, J., Astrakharchik, G. E. & Recati, A. Andreev–Bashkin Effect in Superfluid Cold Gases Mixtures. *New Journal of Physics* **19**, 125005 (2017) (cit. on p. 19).
141. Riboli, F. & Modugno, M. Topology of the Ground State of Two Interacting Bose-Einstein Condensates. *Physical Review A* **65**, 063614 (2002) (cit. on p. 19).
142. Pu, H. & Bigelow, N. P. Properties of Two-Species Bose Condensates. *Physical Review Letters* **80**, 1130 (1998) (cit. on p. 20).
143. Esry, B. D., Greene, C. H., Burke Jr., J. P. & Bohn, J. L. Hartree-Fock Theory for Double Condensates. *Physical Review Letters* **78**, 3594 (1997) (cit. on p. 20).
144. Timmermans, E. Phase Separation of Bose-Einstein Condensates. *Physical Review Letters* **81**, 5718 (1998) (cit. on p. 20).

145. Ao, P. & Chui, S. T. Binary Bose-Einstein Condensate Mixtures in Weakly and Strongly Segregated Phases. *Physical Review A* **58**, 4836 (1998) (cit. on p. 20).
146. Alexandrov, A. S. & Kabanov, V. V. Excitations and Phase Segregation in a Two-Component Bose-Einstein Condensate with an Arbitrary Interaction. *Journal of Physics: Condensed Matter* **14**, L327 (2002) (cit. on pp. 22, 23).
147. Ashcroft, N. W. & Mermin, N. D. *Solid State Physics* (Holt, Rinehart and Winston, New York, 1976) (cit. on p. 23).
148. Lee, T. D., Huang, K. & Yang, C. N. Eigenvalues and Eigenfunctions of a Bose System of Hard Spheres and Its Low-Temperature Properties. *Physical Review* **106**, 1135 (1957) (cit. on p. 23).
149. Lee, T. D. & Yang, C. N. Many-Body Problem in Quantum Mechanics and Quantum Statistical Mechanics. *Physical Review* **105**, 1119 (1957) (cit. on p. 23).
150. Larsen, D. M. Binary Mixtures of Dilute Bose Gases with Repulsive Interactions at Low Temperature. *Annals of Physics* **24**, 89 (1963) (cit. on p. 23).
151. Ancilotto, F., Barranco, M., Guilleumas, M. & Pi, M. Self-Bound Ultradilute Bose Mixtures within Local Density Approximation. *Physical Review A* **98**, 053623 (2018) (cit. on p. 23).
152. Ferioli, G. *Self-Bound Quantum Droplets in Bose-Bose Mixture* PhD thesis (University of Florence, Florence, 2018) (cit. on pp. 24, 25).
153. Schmitt, M., Wenzel, M., Böttcher, F., Ferrier-Barbut, I. & Pfau, T. Self-Bound Droplets of a Dilute Magnetic Quantum Liquid. *Nature* **539**, 259 (2016) (cit. on p. 24).
154. Barranco, M., Guardiola, R., Hernández, S., Mayol, R., Navarro, J. & Pi, M. Helium Nanodroplets: An Overview. *Journal of Low Temperature Physics* **142**, 1 (2006) (cit. on p. 24).
155. Cikojević, V., Dželalija, K., Stipanović, P., Vranješ Markić, L. & Boronat, J. Ultradilute Quantum Liquid Drops. *Physical Review B* **97**, 140502 (2018) (cit. on p. 25).
156. Burchianti, A., D’Errico, C., Rosi, S., Simoni, A., Modugno, M., Fort, C. & Minardi, F. Dual-Species Bose-Einstein Condensate of K 41 and Rb 87 in a Hybrid Trap. *Physical Review A* **98**, 063616 (2018) (cit. on pp. 27, 40).
157. Alcock, C. B. *Vapor Pressure of the Metallic Elements - Equations in CRC Handbook of Chemistry and Physics* 97th ed., 4-120 (CRC Press, 2017) (cit. on p. 28).
158. Williamson, R. S. & Walker, T. Magneto-Optical Trapping and Ultracold Collisions of Potassium Atoms. *Journal of the Optical Society of America B* **12**, 1393 (1995) (cit. on pp. 29, 31).
159. Tiecke, T. G. *Feshbach Resonances in Ultracold Mixtures of the Fermionic Quantum Gases ^6Li and ^40K* PhD thesis (University of Amsterdam, The Netherlands, 2009) (cit. on p. 31).
160. Steck, D. A. *Rubidium 87 D Line Data* (2019) (cit. on pp. 31, 100, 101).

161. Foot, C. J. *Atomic Physics* (Oxford University Press, Oxford ; New York, 2005) (cit. on p. 33).
162. Raj, R. K., Bloch, D., Snyder, J. J., Camy, G. & Ducloy, M. High-Frequency Optically Heterodyned Saturation Spectroscopy Via Resonant Degenerate Four-Wave Mixing. *Physical Review Letters* **44**, 1251 (1980) (cit. on p. 33).
163. Jaatinen, E. Theoretical Determination of Maximum Signal Levels Obtainable with Modulation Transfer Spectroscopy. *Optics Communications* **120**, 91 (1995) (cit. on p. 33).
164. McCarron, D. J., King, S. A. & Cornish, S. L. Modulation Transfer Spectroscopy in Atomic Rubidium. *Measurement Science and Technology* **19**, 105601 (2008) (cit. on p. 33).
165. Grimm, R., Weidemüller, M. & Ovchinnikov, Y. B. *Optical Dipole Traps for Neutral Atoms in Advances In Atomic, Molecular, and Optical Physics* 95 (Elsevier, 2000) (cit. on p. 34).
166. Svelto, O. *Principles of Lasers* (Springer US, Boston, 2010) (cit. on p. 36).
167. Bergeman, T., Erez, G. & Metcalf, H. J. Magnetostatic Trapping Fields for Neutral Atoms. *Physical Review A* **35**, 1535 (1987) (cit. on p. 37).
168. Petrich, W., Anderson, M. H., Ensher, J. R. & Cornell, E. A. Behavior of Atoms in a Compressed Magneto-Optical Trap. *Journal of the Optical Society of America B* **11**, 1332 (1994) (cit. on p. 39).
169. Landini, M., Roy, S., Carcagnì, L., Trypogeorgos, D., Fattori, M., Inguscio, M. & Modugno, G. Sub-Doppler Laser Cooling of Potassium Atoms. *Physical Review A* **84**, 043432 (2011) (cit. on p. 39).
170. Chen, H.-Z., Yao, X.-C., Wu, Y.-P., Liu, X.-P., Wang, X.-Q., Wang, Y.-X., Chen, Y.-A. & Pan, J.-W. Production of Large K 41 Bose-Einstein Condensates Using D 1 Gray Molasses. *Physical Review A* **94**, 033408 (2016) (cit. on p. 40).
171. Rosi, S., Burchianti, A., Conclave, S., Naik, D. S., Roati, G., Fort, C. & Minardi, F. Λ -Enhanced Grey Molasses on the D2 Transition of Rubidium-87 Atoms. *Scientific Reports* **8**, 1301 (2018) (cit. on p. 40).
172. Steck, D. A. *Quantum and Atom Optics* (2023) (cit. on pp. 41, 104).
173. Woodgate, G. K. *Elementary Atomic Structure* 2nd ed. (Clarendon Press, Oxford, 1992) (cit. on pp. 41, 99).
174. Arimondo, E., Inguscio, M. & Violino, P. Experimental Determinations of the Hyperfine Structure in the Alkali Atoms. *Reviews of Modern Physics* **49**, 31 (1977) (cit. on p. 42).
175. Bize, S., Sortais, Y., Santos, M. S., Mandache, C., Clairon, A. & Salomon, C. High-Accuracy Measurement of the ^{87}Rb Ground-state Hyperfine Splitting in an Atomic Fountain. *Europhysics Letters (EPL)* **45**, 558 (1999) (cit. on p. 42).
176. Kohn, W. Cyclotron Resonance and de Haas-van Alphen Oscillations of an Interacting Electron Gas. *Physical Review* **123**, 1242 (1961) (cit. on pp. 49, 51).
177. Hall, D. S., Matthews, M. R., Ensher, J. R., Wieman, C. E. & Cornell, E. A. Dynamics of Component Separation in a Binary Mixture of Bose-Einstein Condensates. *Physical Review Letters* **81** (1998) (cit. on p. 49).

178. Maddaloni, P., Modugno, M., Fort, C., Minardi, F. & Inguscio, M. Collective Oscillations of Two Colliding Bose-Einstein Condensates. *Physical Review Letters* **85**, 2413 (2000) (cit. on p. 49).
179. Bienaimé, T., Fava, E., Colzi, G., Mordini, C., Serafini, S., Qu, C., Stringari, S., Lamporesi, G. & Ferrari, G. Spin-Dipole Oscillation and Polarizability of a Binary Bose-Einstein Condensate near the Miscible-Immiscible Phase Transition. *Physical Review A* **94**, 063652 (2016) (cit. on p. 49).
180. Zhang, J.-Y. *et al.* Collective Dipole Oscillations of a Spin-Orbit Coupled Bose-Einstein Condensate. *Physical Review Letters* **109**, 115301 (2012) (cit. on p. 49).
181. Egorov, M., Opanchuk, B., Drummond, P., Hall, B. V., Hannaford, P. & Sidorov, A. I. Measurement of s-Wave Scattering Lengths in a Two-Component Bose-Einstein Condensate. *Physical Review A: Atomic, Molecular, and Optical Physics* **87**, 053614 (2013) (cit. on p. 49).
182. Fava, E., Bienaimé, T., Mordini, C., Colzi, G., Qu, C., Stringari, S., Lamporesi, G. & Ferrari, G. Observation of Spin Superfluidity in a Bose Gas Mixture. *Physical Review Letters* **120**, 170401 (2018) (cit. on p. 49).
183. Fort, C. & Modugno, M. Dipole Modes of a Trapped Bosonic Mixture: Fate of the Sum-Rule Approach. *Physical Review A* **106**, 043311 (2022) (cit. on pp. 52–55).
184. Pines, D. & Nozières, P. *The Theory of Quantum Liquids* (Benjamin, New York, 1966) (cit. on p. 52).
185. Bohigas, O., Lane, A. M. & Martorell, J. Sum Rules for Nuclear Collective Excitation. *Physics Reports* **51**, 267 (1979) (cit. on p. 52).
186. Lipparini, E. & Stringari, S. Sum Rules and Giant Resonances in Nuclei. *Physics Reports* **175**, 103 (1989) (cit. on p. 53).
187. Miyakawa, T., Suzuki, T. & Yabu, H. Sum-Rule Approach to Collective Oscillations of a Boson-Fermion Mixed Condensate of Alkali-Metal Atoms. *Physical Review A* **62**, 063613 (2000) (cit. on p. 53).
188. Ehrenfest, P. Bemerkung über die angenäherte Gültigkeit der klassischen Mechanik innerhalb der Quantenmechanik. *Zeitschrift für Physik* **45**, 455 (1927) (cit. on p. 54).
189. Horowitz, P. & Hill, W. *The Art of Electronics* 3rd ed. (Cambridge University Press, New York, 2015) (cit. on p. 56).
190. Allan, D. Statistics of Atomic Frequency Standards. *Proceedings of the IEEE* **54**, 221 (1966) (cit. on p. 58).
191. Lomb, N. R. Least-Squares Frequency Analysis of Unequally Spaced Data. *Astrophysics and Space Science* **39**, 447 (1976) (cit. on p. 58).
192. Scargle, J. D. Studies in Astronomical Time Series Analysis. II - Statistical Aspects of Spectral Analysis of Unevenly Spaced Data. *The Astrophysical Journal* **263**, 835 (1982) (cit. on pp. 58, 59).

193. Schuster, A. On the Investigation of Hidden Periodicities with Application to a Supposed 26 Day Period of Meteorological Phenomena. *Terrestrial Magnetism* **3**, 13 (1898) (cit. on p. 58).
194. Welch, P. The Use of Fast Fourier Transform for the Estimation of Power Spectra: A Method Based on Time Averaging over Short, Modified Periodograms. *IEEE Transactions on Audio and Electroacoustics* **15**, 70 (1967) (cit. on p. 58).
195. Irwin, A. W. & Campbell, B. Long-Period Radial-Velocity Variations of Arcturus. *Publications of the Astronomical Society of the Pacific* **101**, 147 (1989) (cit. on p. 59).
196. Eyer, L. & Bartholdi, P. Variable Stars: Which Nyquist Frequency? *Astronomy and Astrophysics Supplement Series* **135**, 1 (1999) (cit. on p. 59).
197. The Astropy Collaboration *et al.* The Astropy Project: Sustaining and Growing a Community-Oriented Open-Source Project and the Latest Major Release (v5.0) of the Core Package*. *The Astrophysical Journal* **935**, 167 (2022) (cit. on pp. 59, 109).
198. The Astropy Collaboration *et al.* The Astropy Project: Building an Open-science Project and Status of the v2.0 Core Package. *The Astronomical Journal* **156**, 123 (2018) (cit. on pp. 59, 109).
199. The Astropy Collaboration *et al.* Astropy: A Community Python Package for Astronomy. *Astronomy & Astrophysics* **558**, A33 (2013) (cit. on pp. 59, 109).
200. Baluev, R. V. Assessing the Statistical Significance of Periodogram Peaks. *Monthly Notices of the Royal Astronomical Society* **385**, 1279 (2008) (cit. on p. 59).
201. Levenberg, K. A Method for the Solution of Certain Non-Linear Problems in Least Squares. *Quarterly of Applied Mathematics* **2**, 164 (1944) (cit. on p. 59).
202. Marquardt, D. W. An Algorithm for Least-Squares Estimation of Nonlinear Parameters. *Journal of the Society for Industrial and Applied Mathematics* **11**, 431 (1963) (cit. on pp. 59, 60).
203. Virtanen, P. *et al.* SciPy 1.0: Fundamental Algorithms for Scientific Computing in Python. *Nature Methods* **17**, 261 (2020) (cit. on pp. 60, 76).
204. Press, W. H., Teukolsky, S. A., Vetterling, W. T. & Flannery, B. P. *Numerical Recipes in C* 2nd ed. (Cambridge University Press, Cambridge, 1992) (cit. on p. 60).
205. Cowan, G. *Statistical Data Analysis* (Oxford University Press, Oxford, 1998) (cit. on p. 60).
206. James, F. *Statistical Methods in Experimental Physics* (World Scientific Publishing Company, 2006) (cit. on p. 65).
207. Law, C. K., Chan, C. M., Leung, P. T. & Chu, M.-C. Critical Velocity in a Binary Mixture of Moving Bose Condensates. *Physical Review A* **63**, 063612 (2001) (cit. on p. 67).
208. Bjørnstrøm, J. E. *Advanced Optics for the Superfluid Flow of Atomic Quantum Mixtures* MA thesis (University of Southern Denmark, Odense, 2018) (cit. on pp. 69, 71, 72, 74, 80).

209. Ketterle, W., Durfee, D. S. & Stamper-Kurn, D. M. *Making, Probing and Understanding Bose-Einstein Condensates* in *Bose-Einstein Condensation in Atomic Gases* Course CXL - Enrico Fermi Summer School (eds Inguscio, M., Stringari, S. & Weiman, C. E.) (Società Italiana di Fisica, Varenna, 1999) (cit. on pp. 69, 70).
210. Fox, M. *Optical Properties of Solids* 2 ed., (with corr.) *Oxford Master Series in Physics Condensed Matter Physics* 3 (Oxford Univ. Press, Oxford, 2012) (cit. on p. 69).
211. Optics, E. *40mm Dia., 0.50 Numerical Aperture, 600-1050nm Coated, Precision Aspheric Lens* (cit. on p. 71).
212. Fuzhou Solid Photon Inc. *Lens Inspection Report* (Fujian, 2019) (cit. on p. 71).
213. Goodman, J. W. *Introduction to Fourier Optics* (Roberts and Company publishers, 2005) (cit. on pp. 72, 74, 94).
214. Mahajan, V. N. Strehl Ratio for Primary Aberrations in Terms of Their Aberration Variance. *Journal of the Optical Society of America* 73, 860 (1983) (cit. on p. 72).
215. Andor. *iXon Ultra 897 EMCCD Datasheet* (Oxford Instruments, 2020) (cit. on pp. 75, 81).
216. Gerrard, A. & Burch, J. M. *Introduction to Matrix Methods in Optics* (Dover, New York, 1994) (cit. on p. 75).
217. Byrd, R. H., Hribar, M. E. & Nocedal, J. An Interior Point Algorithm for Large-Scale Nonlinear Programming. *SIAM Journal on Optimization* 9, 877 (1999) (cit. on p. 76).
218. Standardization Division. *Military Standard Photographic Lenses*. MIL-STD 150A (US Armed Forces Supply Center, 1959) (cit. on p. 77).
219. Stangner, T., Zhang, H., Dahlberg, T., Wiklund, K. & Andersson, M. Step-by-Step Guide to Reduce Spatial Coherence of Laser Light Using a Rotating Ground Glass Diffuser. *Applied Optics* 56, 5427 (2017) (cit. on p. 79).
220. Bureau International des Poids et Mesures. *Le Système International d'unités / The International System of Units* 9 (BIPM, Sèvres, 2019) (cit. on p. 80).
221. Burchianti, A., D'Errico, C., Prevedelli, M., Salasnich, L., Ancilotto, F., Modugno, M., Minardi, F. & Fort, C. A Dual-Species Bose-Einstein Condensate with Attractive Interspecies Interactions. *Condensed Matter* 5, 21 (2020) (cit. on p. 80).
222. Fort, C. *Simulation of Trapped Mixture Ground State (Private Communication)* (cit. on p. 84).
223. Texas Instruments. *DLP9500 DLP® 0.95 1080p 2x LVDS Type A DMD Datasheet* (2023) (cit. on p. 88).
224. Hecht, E. *Optics* 5th ed. (Pearson, Boston Columbus Indianapolis New York San Francisco Amsterdam Cape Town Dubai London Madrid Milan Munich, 2017) (cit. on p. 89).
225. Zupancic, P. *Dynamic Holography and Beamshaping Using Digital Micromirror Devices* MA thesis (Ludwig-Maximilians-Universität, München, 2013) (cit. on p. 90).
226. Perego, E. *Generation of Arbitrary Optical Potentials for Atomic Physics Experiments Using a Digital Micromirror Device* MA thesis (University of Florence, Florence, 2015) (cit. on p. 90).

227. Del Pace, G. *Tailored Optical Potentials for Experiments with Atomic Superfluids* MA thesis (University of Florence, Florence, 2017) (cit. on p. 90).
228. Stetson, P. B. DAOPHOT - A Computer Program for Crowded-Field Stellar Photometry. *Publications of the Astronomical Society of the Pacific* **99**, 191 (1987) (cit. on p. 91).
229. The OpenCV collaboration. *OpenCV: Open Source Computer Vision Library* version 4.8.1. 2023 (cit. on p. 91).
230. Storn, R. & Price, K. Differential Evolution – A Simple and Efficient Heuristic for Global Optimization over Continuous Spaces. *Journal of global optimization* **11**, 341 (1997) (cit. on p. 92).
231. Popoff, S. M., Shih, G., Dirk, B. & Pariente, G. *Wavefrontshaping/ALP4lib: 1.0.1* version 1.0.1. Zenodo, 2022 (cit. on pp. 92, 93).
232. Rosenblatt, M. Remarks on Some Nonparametric Estimates of a Density Function. *The Annals of Mathematical Statistics* **27**, 832 (1956) (cit. on p. 95).
233. Parzen, E. On Estimation of a Probability Density Function and Mode. *The Annals of Mathematical Statistics* **33**, 1065 (1962) (cit. on p. 95).
234. Rossum, G. van & Drake, F. L. *The Python Language Reference* Release 3.0.1 [Repr.] *Python Documentation Manual / Guido van Rossum; Fred L. Drake [Ed.] Pt. 2* (Python Software Foundation, Hampton, NH, 2010) (cit. on p. 101).
235. Harris, C. R. *et al.* Array Programming with NumPy. *Nature* **585**, 357 (2020) (cit. on p. 101).
236. Meurer, A. *et al.* SymPy: Symbolic Computing in Python. *PeerJ Computer Science* **3**, e103 (2017) (cit. on p. 101).
237. Axner, O., Gustafsson, J., Omenetto, N. & Winefordner, J. D. Line Strengths, A-factors and Absorption Cross-Sections for Fine Structure Lines in Multiplets and Hyperfine Structure Components in Lines in Atomic Spectrometry—a User’s Guide. *Spectrochimica Acta Part B: Atomic Spectroscopy* **59**, 1 (2004) (cit. on p. 105).
238. Messiah, A. *Quantum Mechanics*. 2 12th ed. (North-Holland, Amsterdam, 2006) (cit. on p. 105).
239. Rasch, J. & Yu, A. C. H. Efficient Storage Scheme for Precalculated Wigner $3j$, $6j$ and Gaunt Coefficients. *SIAM Journal on Scientific Computing* **25**, 1416 (2004) (cit. on p. 105).
240. Li, X. Reduction of Interference Fringes in Absorption Imaging of Cold Atom Cloud Using Eigenface Method. *Chinese Optics Letters* **5**, 3 (2007) (cit. on p. 109).
241. Ness, G., Vainbaum, A., Shkedrov, C., Florshaim, Y. & Sagi, Y. Single-Exposure Absorption Imaging of Ultracold Atoms Using Deep Learning. *Physical Review Applied* **14**, 014011 (2020) (cit. on p. 109).
242. Bradley, L. *Astropy/Photutils: 1.8.0* version 1.8.0. Zenodo, 2023 (cit. on p. 109).